A numerical and theoretical study of drag reduction using superhydrophobic surfaces

A DISSERTATION
SUBMITTED TO THE FACULTY OF THE GRADUATE SCHOOL
OF THE UNIVERSITY OF MINNESOTA
BY

Yixuan Li

IN PARTIAL FULFILLMENT OF THE REQUIREMENTS
FOR THE DEGREE OF
DOCTOR OF PHILOSOPHY

Krishnan Mahesh, Adviser

September, 2018

Acknowledgements

My first and foremost thanks should go to my academic adviser Prof. Krishnan Mahesh. Thank you for your constant support, guidance, and patience. I hope that I can be as humorous, enthusiastic, and professional as you. Thank you for always being there to answer my questions, to cheer me up, and to give me a pat on my back.

I thank Prof. Ellen Longmire, Prof. Bernardo Cockburn, and Prof. Filippo Coletti for being on my examination committee and reviewing my thesis. I am also thankful to Prof. Satish Kumar for being part of my preliminary examination committee.

I would like to express my very great appreciation to Dr. Aswin Gnanaskandan, Dr. Zane Nitzkorski, Dr. Aman Verma, Dr. Prahladh Iyer, Dr. Rajapandyan Asaithambi, and Dr. Xiaochuan Chai who mentored me during the initial stages of my PhD. I would also like to thank Dr. Chonglin Zhang, Dr. Xian Chen, Dr. Yintao Song, and Dr. Bin Hu for their help when I first joined the department. I would like to thank Mr. Karim Alame for the collaboration with me in the MURI project. I am also grateful to my fellow doctoral students Dr. Praveen Kumar and Mr. Wyatt Horne for their help. I would also like to thank Dr. Yan Ming Tan and Dr. Anand Kartha for all the group study and group TA work during my first year of graduate school.

I am lucky to have colleagues in Prof. Mahesh's group who like to exchange ideas and who inspire each other. Big thanks go out to Sreevatsa Anatharamu, Mrugank Bhatt, Jacob Keller, Dr. Marc Regan, Thomas Kroll, Aditya Madabbushi, Filipe Brandao, and Rong Ma.

I would like to thank my friends at UMN for making my PhD years lively – Mengying Wang, Dr. Fan Feng, Hanlin Gu, Dr. Cheng Qiu, Dr. Yingchen He, Sha Li, Danqing

Deng, and Lu Yu. Finally, I am deeply indebted to my parents for their support and encouragement throughout my study.

This work was supported by the United States Office of Naval Research (ONR) under ONR Grant N00014-12-1-0874 with Dr. Ki-Han Kim as technical monitor. Computing resources from the Argonne Leadership Computing Facility, Minnesota Supercomputing Institute (MSI), and Texas Advanced Computing Center (TACC) are duly acknowledged.

To my family

Abstract

Motivated by the potential drag reduction benefits of superhydrophobic surfaces (SHS), direct numerical simulation (DNS) and theoretical analyses are used to explore the interaction between SHS and turbulent channel flow.

First, DNS is used to study the drag reduction by SHS in laminar channel flow. Resolved multi-phase simulations using the volume of fluid (VOF) methodology are performed to study the effects of groove geometry, interface shear rate and meniscus penetration independently. An analytical solution for the flow in a laminar channel with grooved surface with gas-pocket within is obtained. The solution accounts for both the groove geometry and the trapped fluid properties, and shows good agreement with simulation results. The solution is used to propose a scaling law that collapses data across fully wetted to fully gas-filled regimes. The trapped gas is simulated as both flat and meniscal interfaces. The drag reduction initially increases with interface deflection into the groove and then decreases for large deflections as the interface velocity approaches zero due to the proximity to the bottom of the groove.

Next, the geometric effect of SHS in turbulent flow is studied by performing DNS at friction Reynolds number $Re_\tau = 400$ over longitudinal grooves whose size is comparable to the viscous sublayer thickness. It is found that despite the bulk flow being close to that of a flat-wall channel, the slip effect of the grooves causes some differences within the viscous sublayer. Spectral analysis of the velocity transfer function between the interior and the exterior regions of the grooves shows that the grooves suppress the energy at low frequencies. The DNS reveals negligible Reynolds shear stress near the grooves, which motivates an unsteady Stokes flow model. It is assumed that the flow

in the vicinity of the grooves is governed by the unsteady Stokes equations, forced by an oscillating external flow. The effects of streamwise, spanwise and vertical velocity, freestream wavenumber and the height of freestream perturbation above the groove are studied. The non-dimensional parameter $\omega L^2/\nu$ obtained from this model problem (L is half of the groove span, ω is the frequency of the external turbulent signal and ν is the kinematic viscosity) is used to relate the model to the current DNS. Good agreement is seen with DNS at low frequencies. It is suggested that higher frequency disturbances are produced by smaller spanwise structures near the wall, and when this effect is accounted for, good agreement is also observed at higher frequencies.

Finally, we study multiphase flow within grooved textures exposed to external unsteadiness. We derive analytical expressions for multiphase unsteady Stokes flow within periodic grooves driven by oscillating streamwise/spanwise freestream velocity. Good agreement is obtained between the analytical solution and DNS performed with the VOF method. The effect of oscillation frequency, Reynolds number, and the multiphase interface location on the transfer function between the input signal external to the groove and output near the interface, is examined. Also, the effective slip length and the shear stress over the grooved plane are studied.

Contents

List of Tables

List of Figures

Chapter 1

Introduction

1.1 Motivation

Figure 1.1: A lotus leaf with droplets on the surface. Photo credit: GJ Bulte / wiki commons

Superhydrophobicity is the property where surfaces can maintain large contact angles for sessile drops, thereby exhibiting low wettability - the 'Cassie-Baxter state' [1]. The lotus leaf (figure 1.1) is possibly the best-known natural example of a superhydrophobic surface (SHS). The superhydrophobic effect has been attributed to both surface chemistry and roughness. Trapped gas within the microstructure has been hypothesized to lower the shear at the interface, thus reducing the drag on external flow

over the surface. This observation has inspired several research groups to study such surfaces for their application to drag reduction in both laminar and turbulent flows (see recent reviews in [2–5] and references therein). SHS could consist of regular arrays of grooves or posts (e.g. [6–10]), nanotubes [11, 12], micro-nano dual-scale structures [13], randomly rough structures [14–18], and randomly rough but preferentially streamwise grooves [18].

The magnitude of the slip length over SHS is typically in micrometers, making it challenging for direct experimental measurement [4]. Also, the length scale of fabricated SHS tested in turbulent flows is close to a wall unit, making it challenging for numerical simulations. Table 1.1 lists some of the recent studies of SHS in the turbulent regime, where Re_τ is the friction Reynolds number, w^+, h^+, and ϕ denote the distance between the microridges/posts, the height of the microstructures, and the cavity fraction respectively. The term '$\times 2$' means that alternating no-shear/no-slip boundary conditions are applied on both walls of the turbulent channel to model the SHS effect. The definition of drag reduction varies and is listed on the last column, where CFR implies that the flow is driven by a constant flow rate and CPG represents constant pressure gradient. TBL stands for turbulent boundary layer. By comparing the parameters between simulations and experiments, it is observed that feature sizes of the SHS in most numerical simulations are larger than the experimental values, and the geometry of the microstructure is often ignored since the air-water interface is assumed to be flat and at the same level as the microstructure. Also, in numerical simulations, the air-water interface condition is commonly assumed to be shear free.

The objective of this dissertation is therefore, to use direct numerical simulation (DNS) and theory that resolve the microphysics of the multiphase flow inside the SHS features. §1.2 provides a brief review of relevant past work, and §1.3 summarizes the primary contributions of this dissertation.

	References	Re_τ	w^+	h^+	ϕ	Surface condition	Drag reduction	Definition of drag reduction
Experiments	W2009[7]	156-285	$1-2$	$0.6-1.1$	0.8	Micrograte	$<11\%$	friction factor on SH wall
	DWR2009[8]	72-285	<7	<1.7	0.5	Micrograte on one or both walls	$30-50\%$	SHS skin friction
	PSK2014[9]	250	$1-2$	–	$0.3-0.95$	Micrograte	60%	TBL wall-shear stress
	B2014[15]	$5000-40000$	–	$k^+=0.06-6$	–	Random rough SHS	$0.9-30\%$	SHS skin friction
	L2016[18]	$693-4496$	–	$k^+_{\mathrm{rms}}=0.43-3.28$	–	Random rough SHS	$-11-36\%$	TBL wall-shear stress
Simulations	MK2004[19]	180	–	0	–	$l_x^+, l_z^+ \approx 0.036-3.6$	$<29\%$	Pressure drop(CFR)
	FKK2006[20]	180, 400	–	0	–	$l_x^+, l_z^+ \approx 0.01-1000$	$f(l_x^+, l_z^+, Re_\tau)$	SHS skin friction(CFR)
	MPR2009[21]	180	$17-220$	0	$0.5-0.75$	No-shear/no-slip	$<40\%$	SHS skin frictions(CPG)
	MRP2010[22]	180, 395, 590	$17-220$	0	$0.5-0.75$	No-shear/no-slip	$<50\%$	SHS skin frictions(CPG)
	BS2012[23]	180, 360	–	0	–	$l_x^+=0-100, l_z^+=0-\infty$	$<80\%$	SHS skin frictions(CFR)
	PPK2013[24]	180, 395, 590	$17-885$	0	$0.5-0.94$	No-shear/no-slip×2	$<75\%$	Pressure drop(CFR)
	JJZ2014[25]	180	33.75	0	0.5	No-shear/no-slip×2	$<20\%$	SHS skin frictions(CFR)
	T2014[26]	180	$4.3-280$	0	$0.25-0.75$	No-shear/no-slip×2	$<20\%$	Bulk velocity(CPG)
	SM2015[27] SGM2016[28]	180, 400	5-300	0	$0.01-0.11$	No-shear/no-slip×2	$>15\%$	Slip velocity(CPG)
	J2016[29]	$80-160$	$4.3-280$	$0.03-0.82$	1.0	Air-water interface×2	$5-90\%$	Pressure drop(CFR)
Current study		400	<7.2	<7.2	0.875	Micrograte (fully-wetted)	0	Bulk velocity

Table 1.1: Summary of the parameters and results from SHS research in published literature.

1.2 Review of past work

1.2.1 Drag reduction by superhydrophobic surfaces

Most past work has been performed for laminar flow. The most common assumption in theoretical analyses and simulations (e.g. [21, 24–27, 30, 31]) of SHS is that the gas-liquid interface is flat and shear free. Early theoretical work by Philip [32, 33] obtained the solution to laminar channel flow with alternating no-slip and no-shear boundary conditions on one wall, using conformal mapping. These results have been widely applied to superhydrophobic surfaces. Lauga and Stone [34] further extended this solution to pipe flow. The effect of orientation of the strips on the overall drag reduction was investigated, and the effective slip length for longitudinal strips was shown to be twice that for transverse strips with the same coverage ratio. More importantly, it was proposed that the effective slip length is shear dependent. Another extension of [32] is the analytical solution by Schönecker et al. [35], which contains the viscosity ratio of two fluids by assuming an approximate local slip length as a function of the groove aspect ratio at the interface. Belyaev and Vinogradova [36] described the interface with a prescribed constant local slip length in order to apply the "gas cushion" model [37]. Nizkaya et al. [38] generalized this model to include the viscosity ratio and the geometry of the surface using the operator method. Busse et al. [39] took the dissipation of the air-water layer into consideration, but neglected the geometric features of the surface. The dissipation at the interface is included in [40] by coupling the liquid channel flow to the trapped gas pocket. The interface is assumed to be flat and the gas flow is modeled as a convection cell. This coupled liquid-gas prediction lies between the zero shear model and the experiments. They conjecture that the discrepancy between the experimental data and coupled liquid-gas model is due to the shape of the meniscus not being flat. In their comparison of the slip length between molecular-dynamics simulation and a semi-analytical solution of SHS in strips, Cottin-Bizonne et al. [41] also have suggested that the shape of the interface is important when normal pressure is increased.

The meniscus shape has been the subject of many recent studies. Sbragaglia and Prosperetti [42] used perturbation methods to calculate the correction to the effective

slip length due to small interface curvature. Extensions of this work to the large interface curvature regime include [43], which used a finite element solver to solve for the effective slip length; and Crowdy [44] who used conformal mapping. Davis and Lauga [45] used conformal mapping to study transverse flow over an array of bubbles. However, these three studies assumed the interface to be shear free, therefore resulting in a monotonic increase of the slip length with increasing contact angle (from protruding out of the gas to into the gas). The same trend is found in the numerical results in [30]. This trend is inconsistent with the molecular-dynamics simulations conducted by Cottin-Bizonne et al. [41, 46], which show a preferential normal pressure or contact angle (protruding into the gas) that yields an optimal slip length between the normal and the superhydrophobic state. Similarly, in the study of the dynamical property of the interface in [47], it is found that the effective slip length is very sensitive to the penetration of the meniscus into the groove.

The sustainability of the air pocket is another important issue. In an experiment of turbulent Taylor-Couette flow with SHS by Rosenberg et al. [48], patches of the air-impregnated surface failed, yielding a Wenzel state. A liquid-infused surface with a viscosity ratio of $\mu_{\text{ext}}/\mu_{\text{int}} \sim O(1)$ performed better than air-infused surfaces. The drainage problem of liquid-infused surfaces has been studied in [49]. One reason for the failure of air pockets is that they come in contact with the bottom of the groove [50]. Such a state is described in terms of a criterion for the meniscus radius $R_{\text{cr}} \sim w^2/b$ (w and b are the cavity width and depth respectively) in [51, 52]. In addition to this geometrical threshold, the balance of force between surface tension and the pressure across the interface is studied in [53–55]. The maximum pressure to sustain the interface for a grooved surface is given by

$$\Delta p \leq -2\sigma \cos\theta/[(w+d)\phi], \tag{1.1}$$

where σ is the surface tension of a liquid, θ is the contact angle of the liquid on the solid surface, ϕ_g is the gas fraction, and $(w+d)$ is the groove spacing.

When the interface fails, water penetrates into the surface, and the grooves become

fully-wetted. Kamrin et al. [56] have derived a second-order accurate matrix to describe the effective slip boundary condition of a laminar shear flow at the mean surface height of an arbitrary periodic surface. Wang [57] solved the shear flow over longitudinal or transverse grooves using eigenfunction expansions and matching. Ng and Wang [58] studied the partially wetted grooves problem but assumed a shear-free boundary condition at the interface.

Although the shear-free interface boundary condition has been widely applied [32, 33, 42, 58–60], there has been an emergence of liquid-infused surface in recent years: [48, 61–63], which require a more accurate estimation of the interfacial shear. [36, 38, 64] have considered finite shear by determining a finite slip length, and placing the interface at the crest of the corrugated surface. The interface can deform due to capillary effects; this phenomenon is considered in [42, 44, 65] with a zero-shear approximation. Li et al. [66] applied an approximate boundary condition as the finite shear condition and considered penetration of the interface, which is accurate when the gas layer is thin.

The flow condition is often assumed to be either shear-driven [35, 56–58, 66], or pressure-driven [36, 42, 67]. The shear rate is imposed at an infinite wall-normal location, so that solution is strictly applicable to channel flow when the channel height is much greater than the geometric feature of the surface. Pressure-driven flow can be decomposed into a Poiseuille flow solution and a perturbation due to the SHS for linear governing equations [68]. This approach works well when the shear rate on the multiphase interface is neglected or determined heuristically [64, 68]. If the second fluid inside the microstructures is included in the derivation, it could be under the same pressure gradient [65] or driven by the interfacial stress [67] considering the net cross-sectional flux in the second fluid to be zero [40]. The influence of different geometric parameters of grooves and interface conditions is discussed in [66]. The problem of flow over multiphase grooved surfaces with a freestream condition that considers oscillation and spatial wavenumber has never been reported to the best of the author's knowledge, and is considered in this dissertation.

1.2.2 Wetted turbulent flow over micro-structured surfaces

A canonical SHS consists of regular grooves or posts (e.g. [6]). Geometrically, they are similar to the extensively-studied passive drag-reducing riblets [69–73]. The typical spacing of riblets is within the range $s^+ = u_\tau s/\nu = 3-40$, where s is the spacing between riblet tips, with an optimum $s^+ \approx 15$ [73] and associated riblet height $h^+ \approx s^+$, where u_τ is the friction velocity. The roughness height of drag-reducing riblets lies within the transitional roughness regime. In this regime, the geometric effect of riblets restrains the viscous regeneration cycle, and therefore overall drag is reduced [74]. The roughness amplitude of SHS is generally smaller than the riblets studied in the literature.

When the surface roughness height k^+ is smaller than 5, the surface itself is expected to be hydrodynamically smooth or at most transitionally rough [75]. For example, in the experiment of [15], it was found that k^+ has to be less than 0.5 to produce drag reduction. The SHS in [76] had a $k^+_{\text{rms}} = 0.11$ and the wetted surface was tested to be hydrodynamically smooth. Ling et al. [18] reported that k^+_{rms} has to be less than 1, otherwise over the $1 \leqslant k^+_{\text{rms}} \leqslant 2$ range, the two competing factors of SHS: drag reduction by the SHS and drag increase due to roughness effects, appeared to be balanced. For patterned rough surfaces, Woolford et al. [7] tested micro-grooved surfaces of height $h^+ \approx 1$ in wetted state, and showed that the velocity profile coincided with the flat-wall result. The surface element height in [8] was $k^+ < 1.7$.

Theoretically, Luchini et al. [77] solved the steady Stokes equation for a surface with riblets subject to either parallel or cross flow shear at infinite height using the conformal mapping method. They quantitatively characterized the effect of the grooved-surface in terms of two 'protrusion heights' or the virtual origin [70]. A steady solution to constant shear flow at infinite height over grooved surfaces was derived by Wang [57] using eigenfunction expansions. Ng [78] studied the effect of phase shift between two grooved walls using a similar technique. The slip and shear stress relation of laminar shear-driven flow over surfaces with periodic arbitrary height was studied by Kamrin et al. [56] using a tensorial mobility matrix and perturbation method. Li et al. [66] derived a steady Stokes flow solution over grooved surfaces with a multiphase interface.

The unsteady part of the problem was studied by Larrieu et al. [79] by solving the oscillatory Couette flow over a wavy surface. The oscillating flow condition is similar to the Stokes second problem [80] or active flow control by boundary forcing [81, 82].

1.3 Overview

The objective of this dissertation is to explore the interaction of SHS with turbulent channel flow. An outline of this dissertation is shown in figure 1.2. The SHS is characterized by regular grooves with gas pockets. First, the effect of SHS in laminar channel flow is studied using an approximate boundary condition that models a multiphase interface with constant height. The results are compared to volume of fluid (VOF) simulations. Then, single-phase DNS of turbulent channel flow over a representative geometry of SHS is performed to study the geometric effect of the microstructures in isolation. A model based on the unsteady Stokes behavior of the near field of the surface is developed, and solved analytically. The model is then extended to multiphase flow and compared to VOF simulations to study the effects of surface geometry, properties of the multiphase interface, and most importantly, the unsteady nature of the flow above the surface.

The principal contributions of this work are as follows:

- The drag-reducing ingredients of SHS in laminar flow are studied systematically, which include the effects of groove geometry, gas flow and meniscus penetration. The coverage ratio, depth, and the viscosity ratio of the interface all have a positive, monotonic effect on drag reduction. The curvature of the interface has a non-monotonic influence. Drag reduction initially increases with interface deflection into the groove, and then decreases for large deflections as the interface velocity approaches zero due to the proximity to the bottom of the groove. Such a trend is consistent with the molecular-dynamics simulations conducted by Cottin-Bizonne et al. [41, 46].

- An analytical solution is obtained for the flow in a laminar channel with grooved surfaces containing gas-pockets. The solution accounts for both, groove geometry

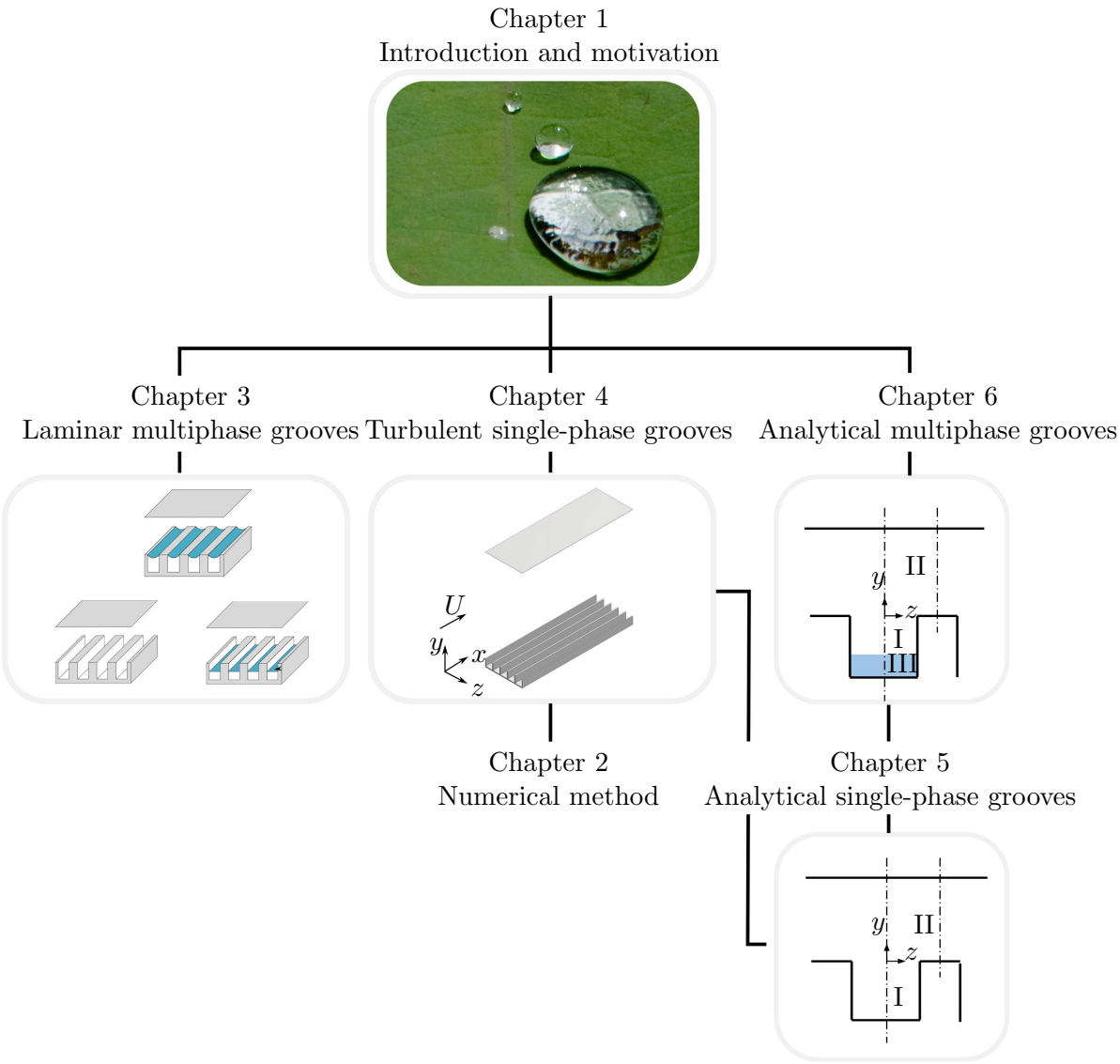

Figure 1.2: Overview of the dissertation.

and properties of the trapped fluid, and shows good agreement with simulation results. The solution of the effective slip length can be used *a priori* as a scaling factor to predict the drag reduction. The scaling law collapses data across fully wetted to fully gas-filled regimes.

- A clone code is developed to overcome the the memory constraint of commercial mesh generating software when a very fine mesh that resolves the micro-structured feature of the SHS is required. The code reads in the mesh file of one part of the domain of interest and duplicate it in periodic directions by geometric progression, merges the boundaries between the new domains as interior faces, then writes out the mesh file of the domain needed.

- Using the mesh generated by the clone code, DNS is performed to study the geometric effect of grooved surfaces with feature size comparable to realistic SHS, and smaller than the past riblet studies, at a moderate Reynolds number $Re_\tau = 400$. One wall of a channel is modeled as longitudinal grooves. It is found that despite the bulk flow being close to that of a flat-wall channel, the slip effect of the grooves causes some differences within the viscous sublayer. Spectral analysis of the velocity transfer function between the interior and the exterior regions of the grooves shows that the grooves suppress the energy at low frequencies.

- The DNS reveals negligible Reynolds shear stress near the grooves, which motivates an unsteady Stokes flow model. It is assumed that the flow in the vicinity of the grooves is governed by the unsteady Stokes equations, forced by an oscillating external flow. The effects of streamwise, spanwise and vertical velocity, freestream wavenumber and the height of freestream perturbation above the groove are studied by numerical experiments and analytical formulation. The non-dimensional parameter $\omega L^2/\nu$ obtained from this model problem (L is half of the groove span, ω is the frequency of the external turbulent signal and ν is the kinematic viscosity) is used to relate the model to the current DNS. Good agreement is seen with DNS at low frequencies. It is suggested that higher frequency disturbances are produced by smaller spanwise structures near the wall, and when this effect is

accounted for, good agreement is also observed at higher frequencies.

- An analytical formula is derived for multiphase unsteady Stokes flow driven by an oscillating streamwise/spanwise velocity in the presence of periodic grooves using separation of variables and eigenfunction expansions. The penetration effect is included by assuming that the interface is flat, and both phases are solved simultaneously. Good agreement is obtained between the analytical solution and the DNS using the VOF methodology.

- A parametric study is conducted that involves the freestream frequency, Reynolds number, and the multiphase interface location. The penetration of the external disturbance, the effective slip length and the shear stress over the grooved plane are examined. It is found that the penetration of the external fluid has a stronger impact for transverse flow than longitudinal flow.

This dissertation is organized as follows. Chapter 2 describes the governing equations, and the algorithm to generate the large periodic mesh used in the DNS. The drag-reducing ingredients of SHS in laminar channel flow are studied in Chapter 3. It is found that the geometry of the microstructure, multiphase interface location, trapped gas properties, and gas flow condition all contribute to the drag-reducing effect of SHS. Grooved surfaces in the hydrodynamically smooth regime in turbulent channel flow are studied in Chapter 4 where the geometric features are resolved. DNS and a set of numerical experiments involving the near-field of the grooved surface are performed. The dynamic flow response inside the groove is further studied in Chapter 5 by an analytical solution to single-phase Stokes flow subject to an unsteady forcing. This solution is extended to include arbitrary multiphase (i.e. air or liquid-infused flow) inside the groove in Chapter 6.

Chapter 2

Numerical method

A focus of this dissertation is numerical simulation that resolves the microstructures of SHS in turbulent flow. This chapter introduces the numerical method used in the simulations and a special procedure to generate the large mesh that resolves the very fine geometry of SHS. The governing equations are discussed in §2.1, and the code used for grid generation is presented in §2.2.

2.1 Governing equations and numerical discretization

The incompressible Navier-Stokes equations are solved numerically using the algorithm described in [83], on unstructured grids.

$$\frac{\partial u_i}{\partial t} + \frac{\partial u_i u_j}{\partial x_j} = -\frac{\partial p}{\partial x_i} + \nu \frac{\partial^2 u_i}{\partial x_j x_j} + K\delta_{i1}, \tag{2.1}$$

$$\frac{\partial u_i}{\partial x_i} = 0, \tag{2.2}$$

where u_i and p denote the velocities and pressure respectively and K is the constant pressure gradient (CPG) applied in the x-direction. The algorithm is a predictor-corrector formulation that emphasizes discrete energy conservation for the convection and pressure terms on unstructured grids. This property guarantees robustness at high Reynolds numbers without adding numerical dissipation. The solutions are integrated

in time implicitly using the Crank-Nicolson scheme, or explicitly using the second order Adams-Bashforth method. The algorithm has been validated for a variety of problems over a range of Reynolds numbers [83]. The algorithm has been used in the past to simulate a variety of complex flow problems, including jets [84–93], flow over hulls [94–96], propellers in the crashback mode [97–104], and flow over rough surfaces [105].

The Harlow-Welch algorithm [106] is discretely kinetic energy conserving on staggered, structured grids. The numerical method developed by Mahesh et al. [83] extends this property to unstructured grids, and is a finite volume method where the Cartesian velocities u_i and pressure p are stored at the centroids of the cells and the face-normal velocities v_n are stored independently at the centroids of the faces. Henceforth, all resolved flow variables will be denoted simply, without the overbar $\overline{()}$.

A predictor-corrector type, fractional-step method is used to solve equation (2.2). The non-linear convective term is denoted by NL and the viscous term incorporating the SGS stress term is denoted by $VISC$. Explicit time advancement is performed using the Adams-Bashforth scheme which is $O(\Delta t^2)$. The predicted velocities u_i^* at the control volume centroids are first obtained from the previous time steps k and $k-1$:

$$\frac{u_i^* - u_i^k}{\Delta t} = \frac{1}{2}\left[3(NL + VISC)^k - (NL + VISC)^{k-1}\right], \tag{2.3}$$

and then interpolated using symmetric averaging ($O(\Delta x^2)$) to obtain the predicted face-normal velocities:

$$v_n^* = \left(\frac{u_{i,icv1}^* + u_{i,icv2}^*}{2}\right) n_i, \tag{2.4}$$

where the face-normal $\vec{n}$ and hence v_n points from control volume $icv1$ to $icv2$.
The corrector step

$$\frac{u_i^{k+1} - u_i^*}{\Delta t} = -\frac{\partial p^{k+1}}{\partial x_i} \tag{2.5}$$

is projected onto the face-normal as:

$$\frac{v_n^{k+1} - v_n^*}{\Delta t} = -\frac{\partial p^{k+1}}{\partial n}. \tag{2.6}$$

The continuity equation imposes the constraint

$$\sum_{\text{faces of cv}} v_n^{k+1} A_f = 0, \tag{2.7}$$

where A_f is the face area. Substituting in equation (2.6) yields a Poisson equation for p^{k+1}:

$$\begin{aligned} \sum_{\text{faces of cv}} v_n^{k+1} A_f - \sum_{\text{faces of cv}} v_n^* A_f &= -\Delta t \sum_{\text{faces of cv}} \frac{\partial p^{k+1}}{\partial n} A_f \\ \Rightarrow \Delta t \sum_{\text{faces of cv}} \frac{\partial p^{k+1}}{\partial n} A_f &= \sum_{\text{faces of cv}} v_n^* A_f, \end{aligned} \tag{2.8}$$

which is solved using the Algebraic Multi-Grid (AMG) method of *hypre* [107].
Once p^{k+1} is known, the pressure gradient $\frac{\partial p}{\partial x_i}$ is computed using a novel least squares formulation which minimizes the conservation error:

$$\sum_{\text{faces of cv}} \left(\frac{\partial p}{\partial x_i} n_i A_f - \frac{\partial p}{\partial n} A_f \right)^2. \tag{2.9}$$

Finally, corrected u_i and v_n are computed from equations (2.5) and (2.6) using p^{k+1}.

Most of the simulations in this dissertation are performed with implicit time advancement using the Crank-Nicolson scheme which is $O(\Delta t^2)$:

$$\frac{u_i^* - u_i^k}{\Delta t} = \frac{1}{2} \left[(NL + VISC)^k + (NL + VISC)^{k+1} \right]. \tag{2.10}$$

$(NL + VISC)^{k+1}$ contains u_i^{k+1} which is expressed in terms of u_i^k as

$$u_i^{k+1} = u_i^* - \Delta t \frac{\partial p^{k+1}}{\partial x_i}, \tag{2.11}$$

where p^{k+1} is linearized as $p^{k+1} = p^k + O(\Delta t)$. Equation (2.10) reduces to a system of linear equations which is solved for u_i^* using SOR.

Note that typically, the face-normal derivatives at a face are computed using

$$\frac{\partial (\cdot)}{\partial n} \Big|_f = \frac{(\cdot)_{nbr} - (\cdot)_{icv}}{d_f}, \tag{2.12}$$

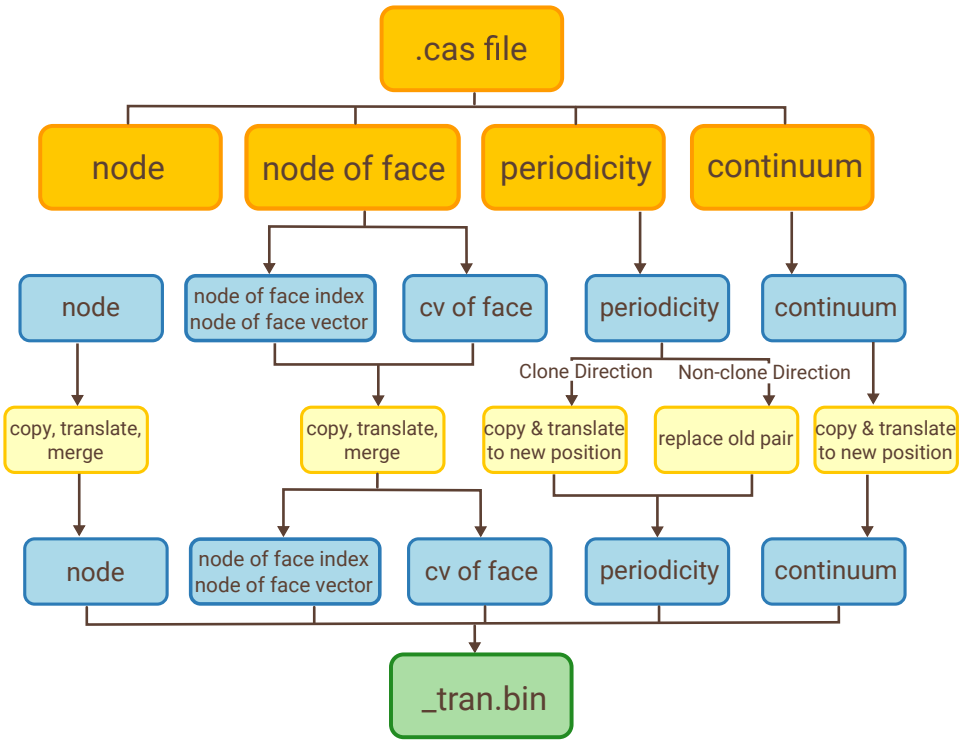

Figure 2.1: Flowchart of the clone code.

where nbr denotes the neighboring control volume of icv and $d_f = (x_{i,nbr} - x_{i,icv})n_{i,f}$ is the face-normal distance.

2.2 Grid generation

The large number of computational geometry facets posed severe challenges to the memory constraints of commercial grid generation software. To overcome this challenge, a 'clone' code that reads in a mesh file and expand it into a large domain was developed.

Figure 2.1 shows the flowchart of the whole cloning process. A mesh file (.cas) generated in Pointwise® contains the information of the coordinates of the nodes, nodes that assemble faces, boundary conditions, periodicity, and the property of the continuum. The Fortran code 'bintran.f90' translates the .cas file into separate binary files that have each of the above information, reconstructs the properties of the faces in terms of the

nodes of faces and the common face between two control volumes into two different binary files, and finally combine all the binary files together into a '_tran.bin' file. The clone code reads in each of these binary files before the combining, and reconstructs them into binary files that make up the large domain of interest. The procedures are as follows.

After the user chooses to clone the mesh from the screen, the clone subroutine is called within 'bintran.f90'.

1. The code reads in the 'clone.in' file prepared by the user:

```
multiple_clone_direction
1
dir_x                    dist_cp
1                        5.0
no_edge                  fa_edge_tag
5.0                      xperio
dir_y                    dist_cp
0                        0.0
no_edge                  fa_edge_tag
3500.0                   none
dir_z                    dist_cp
1                        4
no_edge                  fa_edge_tag
2                        zperio
```

multiple_clone_direction: 1, 2 or 3. The number of directions (≤ 3) the clone process will be performed in.

dir_x, dir_y, or dir_z: 1 or -1. The direction the clone process will be performed in. 1 indicates positive direction; -1 indicates negative direction.

no_edge: The coordinate of the node on the face that is going to be merged in the related direction.

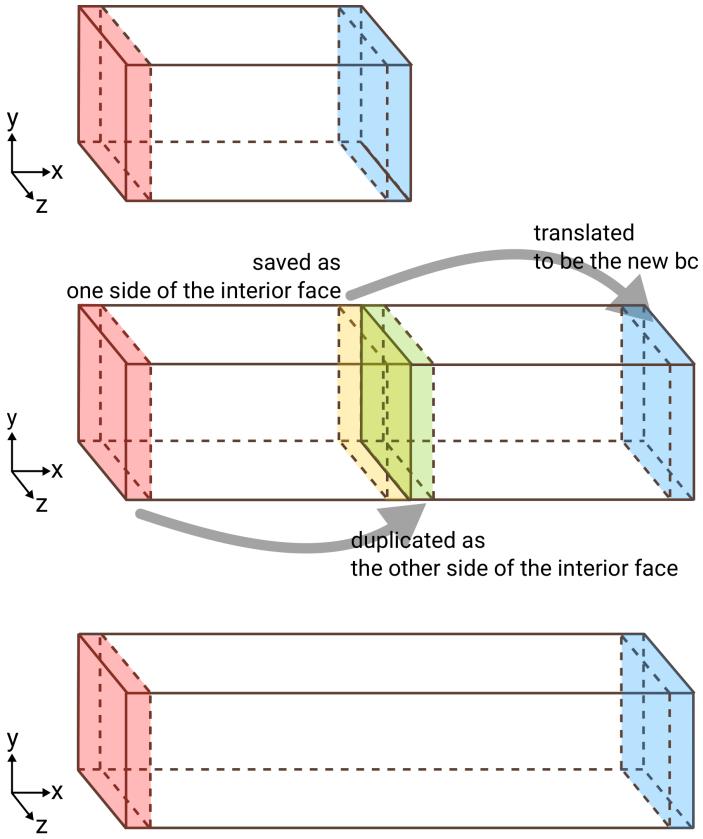

Figure 2.2: Procedure to clone a mesh in the x-direction.

dist_cp: The distance the mesh will be displaced with respect to the original.

fa_edge_tag: The boundary condition of the face that is going to be merged.

2. The node coordinates are read in, copied, and placed in the new location. The overlapping nodes are removed, based on the difference between the sequence of the cloned nodes and original nodes, and stored in the *node_diff_l* array for use in defining the node-of-face list in the next step.

3. The procedure to clone the node-of-face list and the common face between two control volumes is illustrated in figure 2.2. In this example, the mesh is being cloned in the x-direction. The faces are grouped into different zones as 'wall', 'xperiodic', 'xperiodic-shadow', 'zperiodic', 'zperiodic-shadow', and 'interior' based on their

boundary conditions. Each zone is treated separately. The faces in zones 'wall', 'zperiodic', and 'zperiodic-shadow' are parallel to the clone direction and therefore copied and translated to the new location directly. By looking up the *node_diff_l* array created in the previous step, the node-of-face list in the new zones is created. The volumes in green (shifted from the volume in red) are stored in an array. The volumes in yellow (originally blue) are stored in another array. These two arrays are used as the neighboring control volumes defining the new interior faces between them. The faces in zone 'xperiodic' (red) remain. The faces in zone 'xperiodic-shadow' (blue) are translated to the designated position and assigned as the new boundary faces. The difference between the sequence of the cloned faces and the original faces are stored in the *face_diff_l* array, for use in defining the list of periodic pairs in the next step.

4. The original periodic pairs in zones 'zperiodic' and 'zperiodic-shadow' are copied directly. The new pairs are found from the *face_diff_l* array created in the previous step. The periodic faces in zones 'xperiodic' are retained and their 'xperiodic-shadow' partners are found from the *face_diff_l* array as well.

5. The number of control volumes is doubled and therefore the 'continuum' property is also doubled.

6. Finally, the new binary files generated by the clone process replace the original files. The files are sent back to bintran.f90 for final combination.

The clone code presented in this section will be used to study the turbulent flow over micro-grooved surfaces in Chapter 4.

Chapter 3

Laminar drag reduction by superhydrophobic surfaces

We explore the drag-reducing ingredients of SHS using DNS and VOF simulations performed by Alame and Mahesh [108]. An analytically obtained scaling law for drag reduction is proposed. The VOF simulation is used to conduct controlled studies of two commonly omitted components: gas flow and penetration. In §3.2 the VOF method is validated against the experiment by Maynes et al. [40] and used to evaluate the effects of gas flow and penetration of the interface. In §3.3, an analytical solution is obtained that accounts for groove geometry as well as properties of both fluids. The analytical solution is compared to the VOF simulation and DNS results and used to develop a scaling law for the drag reduction which collapses data across fully wetted to fully gas-filled regimes (§3.3.3). The effect of interface curvature is studied in §3.4 by describing the interface with the Young-Laplace equation. An asymptotic analysis of the analytical solution is performed in §3.5. §3.6 summarizes this chapter.

3.1 Problem formulation and simulation parameters

We consider the laminar flow in a channel with grooved SHS as shown in figure 3.1. The independent variables that defines the problem are H, w, d, b, h, $\mu_{\text{gas}}/\mu_{\text{liquid}}$,

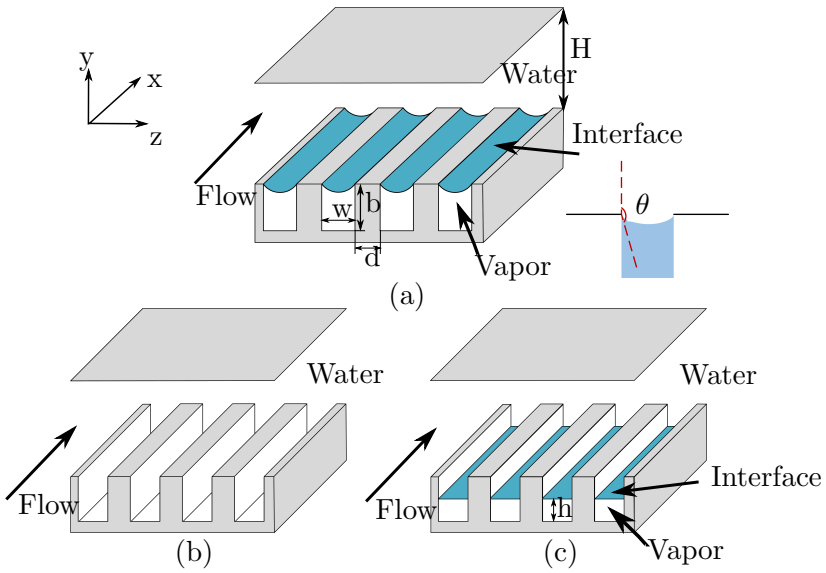

Figure 3.1: The channel geometry and groove configuration. (a) Grooved channel with meniscus interfaces (cases M7, M12, and M25). Definition of the contact angle θ in this chapter is shown on the right. (b) Fully wetted grooved channel (cases F7, F12, and F25). (c) Grooved channel with flat interfaces (cases I7, I12, and I25).

$\rho_{\text{gas}}/\rho_{\text{liquid}}$, $\dot{Q}_{\text{liquid}}$, σ, g, where H is the height of the channel, w is groove width, d is the distance between the grooves, b is the groove depth, $\mu_r = \mu_{\text{gas}}/\mu_{\text{liquid}}$ is the liquid to gas viscosity ratio, $\rho_{\text{liquid}}/\rho_{\text{gas}}$ is the liquid to gas density ratio, $\dot{Q}_{\text{liquid}}$ is the volume flow rate of the liquid, σ is the surface tension of the gas-liquid interface, and g is the gravitational acceleration. In a channel with smooth walls, the friction factor is $f = f(Re)$ for laminar flow. Nondimensionalization yields the friction factor $f = f(\text{Re}, \mu_r, \rho_{\text{liquid}}/\rho_{\text{gas}}, w/(w+d), H/(w+d), h/b, b/H, \text{We}, \text{Bo})$, where $Re = \rho_{\text{liquid}} U(w+d)/\mu_{\text{liquid}}$, $\text{We} = \rho_{\text{liquid}} U^2(w+d)/\sigma$, $\text{Bo} = (\rho_{\text{liquid}} - \rho_{\text{gas}})g(w+d)^2/\sigma$, $U = Q/A$. The density and viscosity ratio are constants. The governing parameters for a channel with SHS are the coverage ratio $\phi = w/(w+d)$, and the channel aspect ratio $H/(w+d)$. Accounting for groove geometry and interface surface tension introduces the additional parameters above. Different models are simulated numerically to conduct a thorough study of the factors that contribute to drag reduction. The simulation parameters are listed in table 3.1. Case number prefixes "F", "I" and "M" represent fully wetted,

	Case	$H/(w+d)$	ϕ	$h/b(\%)$	Bo($\times 10^{-4}$)	We($\times 10^{-3}$)
Fully wetted	F7	1.88	1/4, 1/2, 3/4	n/a	n/a	n/a
	F12	3.1875	1/4, 1/2, 3/4	n/a	n/a	n/a
	F25	6.25	1/4, 1/2, 3/4	n/a	n/a	n/a
Flat interface	I7	1.88	1/4, 1/2, 3/4	28, 60, 90, 100	n/a	n/a
	I12	3.1875	1/4, 1/2, 3/4	28, 60, 90, 100	n/a	n/a
	I25	6.25	1/4, 1/2, 3/4	28, 60, 90, 100	n/a	n/a
Meniscus	M7	1.88	1/2	n/a	2.22	5.56
	M12	3.1875	1/2	n/a	2.22	5.56
	M25	6.25	1/2	n/a	2.22	5.56

Table 3.1: Simulation parameters. Case number prefixes F, I and M represent fully wetted, interface, and meniscus studies. The depth of the groove is fixed at $b/(w+d) = 0.625$. $\mathrm{Re} = 4 \times 10^{-4}$.

interface, and meniscus studies. The cross section configuration is shown in figure 3.1.

The simulations were performed at a constant liquid flow rate, and the drag reduction is defined as:

$$\mathrm{DR} = \frac{K_{\mathrm{no-slip}} - K_{\mathrm{SHS}}}{K_{\mathrm{no-slip}}}, \tag{3.1}$$

where $K_{\mathrm{no-slip}}$ and K_{SHS} are the body forces applied to the no-slip and SHS channel respectively. Periodic boundary conditions are imposed in the streamwise and spanwise directions. The grid size is e.g. for F7 $N_x \times N_y \times N_z = 3 \times 151 \times 161$ for the channel part, and $N_x \times N_y \times N_z = 3 \times 61 \times 81$ to resolve the groove. Grid convergence studies were performed. Doubling the number of nodes in z and y for the case F7 ($\phi = 1/2$) changed the body force by only 0.02%. Similarly, for the VOF case involving a flat or a meniscus interface, the grid size was refined until the drag reduction difference was less than 1%.

3.2 Gas flow and liquid penetration effects

The VOF method from [108] is validated in [66] using the analytical solutions in [39] and the effect of gas flow assumption is evaluated by simulating the experiment in [40]. In the experiment of Maynes et al. [40], the channel has varying groove widths on the top and bottom walls. The drag reduction is quantified in terms of the Darcy friction factor–Reynolds number product fRe as a function of groove widths nondimensionalized by the total pitch length $(w + d)$.

In [66], a channel ($H = 7.69,\ w + d = 4$) flow with grooves ($b = 2.5$) on both walls was simulated using VOF by assuming three different gas flow conditions: equal pressure gradient in both phases, zero volume flow rate inside the groove, and zero pressure gradient inside the groove. The gas was assumed to fill the entire groove and the interface was flat. According to the VOF simulation the equal pressure gradient in both phases yields the least amount of drag, similar to what was observed for the canonical multiphase channel. Both the zero pressure gradient and the zero volume flow rate cases are very close but the latter still has higher drag. All three cases predict the same trend as experiments. The recirculating gas flow is the closest; the levels however

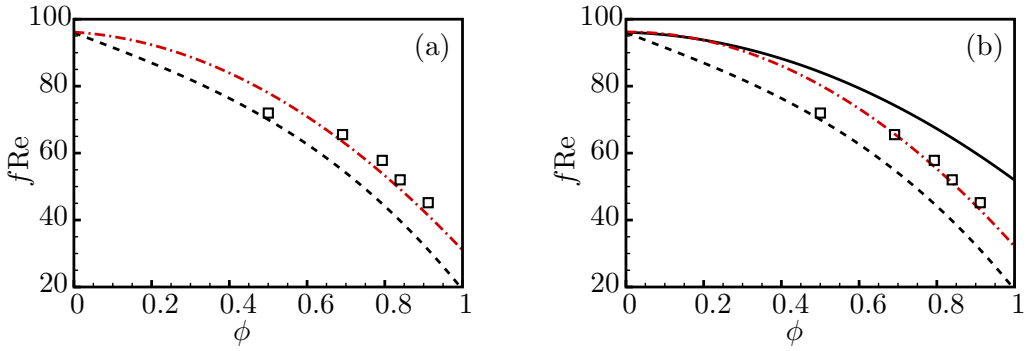

Figure 3.2: Comparison of fRe with varying groove fractions ϕ. (a) ·— meniscus shape of contact angle 150°; (b) ·— flat interface with 16% water penetration, —— for a fully wetted groove (□ experimental results by Maynes et al. [40], · · · for full gas pocket filling the groove).

are lower than the experiments. This behavior is similar to the trend observed by the cavity model of [40]. They speculate that the difference is because change in streamwise pressure induces a continuous change in the meniscus shape that eventually causes the liquid to penetrate slightly into the groove, thus reducing the effective gas layer height.

Two methods are used to represent the liquid penetration effect: prescribing a meniscus with a contact angle of $\theta = 150°$ (defined in figure 3.1) or a flat interface at $y = -16\%b$. The contact angle is identical to the surface property reported in the experiment of [40]. The 16% liquid penetration is selected so that the area of the external fluid penetrating into the groove is the same as applying a meniscus with a contact angle $\theta = 150°$. The grooves are supposed to be capped at the end, i.e., zero flow rate is imposed inside the grooves.

Figure 3.2(a) and figure 3.2(b) show that liquid penetrating into the groove also affects the overall drag. Both methods capture the penetration effect.

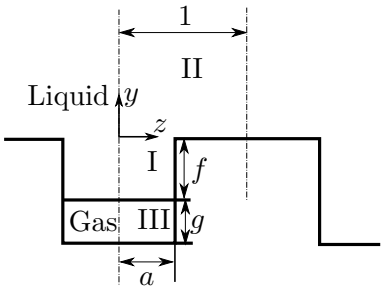

Figure 3.3: The model problem and definitions of the geometric variables. Regions I and III are inside the groove filled with liquid and gas respectively. Region II is outside the groove, filled with liquid.

3.3 Analytical solution

3.3.1 Model problem

The influence of liquid penetration observed in §3.2 motivates us to derive an analytical solution that accounts for its effect. Typically, the texture size of SHS in turbulent experiments in viscous units $(w+d)^+ = u_\tau L/\nu < 5$ [8, 9]. When the groove is small relative to the channel, the flow in the vicinity of the grooves can be treated as shear flow. The shear-driven flow over longitudinal grooves with coupled gas-liquid interface within the grooves can be solved analytically as follows. A corresponding solution for fully wetted grooves solutions is obtained by Wang [57], which can be recovered from the current solution using asymptotic analysis (§3.5).

The model problem is illustrated in figure 3.3. The flow is normal to the (y, z) plane, and the streamwise velocity u is normalized by $(L\tau/\mu)$. All lengths are normalized by L, where L is half of the period of the grooves. $a = \phi = w/(2L)$ is half width of the groove, and g is the depth of the gas pocket inside the groove. $f + g$ is the depth of the groove. The governing equation is the Laplace equation:

$$\frac{\partial^2 u}{\partial y^2} + \frac{\partial^2 u}{\partial z^2} = 0. \tag{3.2}$$

The domain is divided into three rectangular regions. The velocity is zero at all solid walls, and at infinite height $\frac{\partial u(\infty,z)}{\partial y} = 1$. At the gas-liquid interface (between regions I

and III), the shear stress and velocity are matched:

$$u_{\mathrm{I}}(-f,z) = u_{\mathrm{III}}(-f,z), \tag{3.3}$$

$$\mu_{\mathrm{liquid}}\frac{\partial u_{\mathrm{I}}(-f,z)}{\partial y} = \mu_{\mathrm{gas}}\frac{\partial u_{\mathrm{III}}(-f,z)}{\partial y}. \tag{3.4}$$

When the layer is thin enough, the Couette flow assumption approaches the pressure-driven assumption, which suggests an approximate boundary condition to represent the gas-liquid interface:

$$\frac{du_{\mathrm{gas}}}{dy} \sim \frac{u_{\mathrm{gas}}}{h}, \quad \text{yielding} \quad \frac{du_{\mathrm{liquid}}}{dy} \approx \mu_r \frac{u_{\mathrm{liquid}}}{h_r}. \tag{3.5}$$

This is accurate in a Couette type gas flow and also representative of a pressure driven gas flow when the gas layer is thin. Note that one can rework equations (2) and (3) in [38] and get the same expression.

At the gas-liquid interface, we apply the approximate gas-liquid boundary condition:

$$\frac{\partial u_{\mathrm{I}}(-f,z)}{\partial y} = \mu_r \frac{\partial u_{\mathrm{III}}(-f,z)}{\partial y} = \mu_r \frac{u_s(z)}{g}, \tag{3.6}$$

from equation (3.5). This is valid when the gas flow inside the grooves is a Couette type flow or a pressure driven gas flow when the depth of the groove is small compared with the outside channel height, so that the velocity gradient can be obtained from linear approximation.

In region I, using separation of variables, $u_{\mathrm{I}}(y,z) = v(y)w(z)$, and the approximate gas-liquid boundary condition above, the main assumption is that $w(z)$ is a linear function of the interface velocity at the interface between regions I and III:

$$u_s(z) = \alpha w(z). \tag{3.7}$$

Therefore, $\partial v(-b)/\partial y = \mu_r \alpha / g$. Then we obtain

$$u_{\mathrm{I}} = \sum_{n=1}^{\infty} \frac{\alpha}{2} A_n \cos(\alpha_n z) \left[\left(\frac{\mu_r}{g\alpha_n} + 1 \right) e^{\alpha_n (f+y)} - \left(\frac{\mu_r}{g\alpha_n} - 1 \right) e^{-\alpha_n (f+y)} \right], \tag{3.8}$$

where $\alpha_n = (n - \frac{1}{2})\frac{\pi}{a}$. In region II, the general solution is

$$u_{\mathrm{II}} = B_0 + y + \sum_{n=1}^{\infty} B_n \cos(\gamma_n z) e^{-\gamma_n y}, \tag{3.9}$$

where $\gamma_n = n\pi$. The general solution for region III that satisfies the no-slip condition on the walls and symmetry is:

$$u_{\mathrm{III}} = \sum_{n=1}^{\infty} C_n \cos(\alpha_n z) \left[-e^{\alpha_n (y+2f+2g)} + e^{-\alpha_n y} \right]. \tag{3.10}$$

By satisfying equation (3.7) at the interface we get

$$\alpha A_n = C_n \left[-e^{\alpha_n (f+2g)} + e^{\alpha_n f} \right]. \tag{3.11}$$

At the boundary between regions I and II, u_{I} and u_{II} are matched by

$$u_{\mathrm{II}} = \begin{cases} u_{\mathrm{I}}, & 0 \leqslant z < a, \\ 0, & a < z \leqslant 1; \end{cases} \tag{3.12}$$

$$\frac{\partial u_{\mathrm{I}}(-f, z)}{\partial y} = \frac{\partial u_{\mathrm{II}}(-f, z)}{\partial y}. \tag{3.13}$$

Integrating equation (3.12) from 0 to 1 yields

$$\begin{aligned} B_0 = &- \sum_{n=1}^{\infty} \frac{1}{2} C_n \frac{(-1)^n}{\alpha_n} \left[-e^{\alpha_n (f+2g)} + e^{\alpha_n f} \right] \\ &\times \left[\left(\frac{\mu_r}{g\alpha_n} + 1 \right) e^{\alpha_n f} - \left(\frac{\mu_r}{g\alpha_n} - 1 \right) e^{-\alpha_n f} \right]. \end{aligned} \tag{3.14}$$

Multiplying equation (3.12) by $\cos(\gamma_m x)$ and then integrating yields

$$B_m = \sum_{n=1}^{\infty} C_n L_{mn} \left[-e^{\alpha_n (f+2g)} + e^{\alpha_n f} \right] \left[\left(\frac{\mu_r}{g\alpha_n} + 1 \right) e^{\alpha_n f} - \left(\frac{\mu_r}{g\alpha_n} - 1 \right) e^{-\alpha_n f} \right], \tag{3.15}$$

f, g\M	5	10	15	20	25	30	35	40	45
1.25, 1.125	0.1319	0.1301	0.1307	0.1305	0.1306	0.1305	0.1306	0.1306	0.1306
0.25, 0.125	0.1289	0.1272	0.1278	0.1275	0.1277	0.1276	0.1277	0.1276	0.1277

Table 3.2: Convergence of B_0, $a = 0.6$.

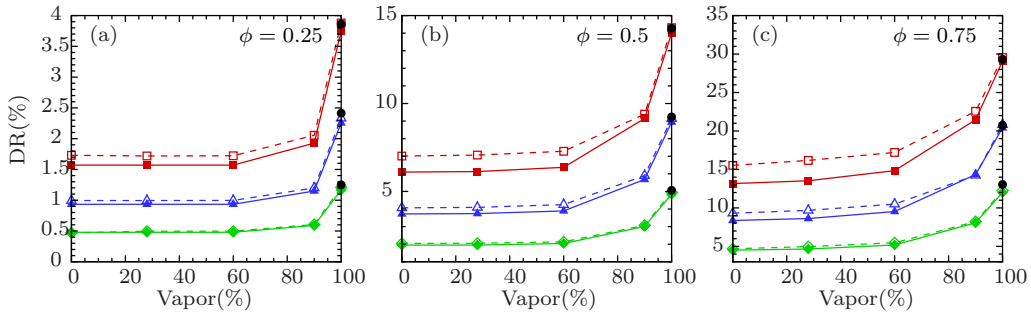

Figure 3.4: Drag reduction comparison. The open symbols represent the DNS result; the solid symbols are predicted by the analytical solution from equation (3.20). The black dots are VOF simulations results. (a) Coverage ratio $\phi = 0.25$. (b) $\phi = 0.5$. (c) $\phi = 0.25$. –□–, case I7; –△–, case I12; –◇–, case I25.

where

$$L_{mn} = \frac{\sin[\pi(ma + n - 0.5)]}{2\pi[m + (n - 0.5)/a]} + \frac{\sin[\pi(ma - n + 0.5)]}{2\pi[m - (n - 0.5)/a]}. \tag{3.16}$$

Multiplying equation (3.13) by $\cos(\alpha_m x)$ and integrating from 0 to a gives

$$\sum_{n=1}^{\infty} -B_n L_{nm}\gamma_n - \frac{(-1)^m}{\alpha_m} = \frac{a}{4} C_m \alpha_m \left[-e^{\alpha_m(f+2g)} + e^{\alpha_m f}\right] \times \left[\left(\frac{\mu_r}{g\alpha_m} + 1\right) e^{\alpha_m f} + \left(\frac{\mu_r}{g\alpha_m} - 1\right) e^{-\alpha_m f}\right]. \tag{3.17}$$

B_m is truncated to M terms and A_n is truncated to $N = Int[aM]$ terms. Solving equations (3.15) and (3.17) as a system of equations, we can solve for the mean slip velocity B_0 from equation (3.14). Table 3.2 shows the convergence of B_0 with respect to M, with two sets of f and g.

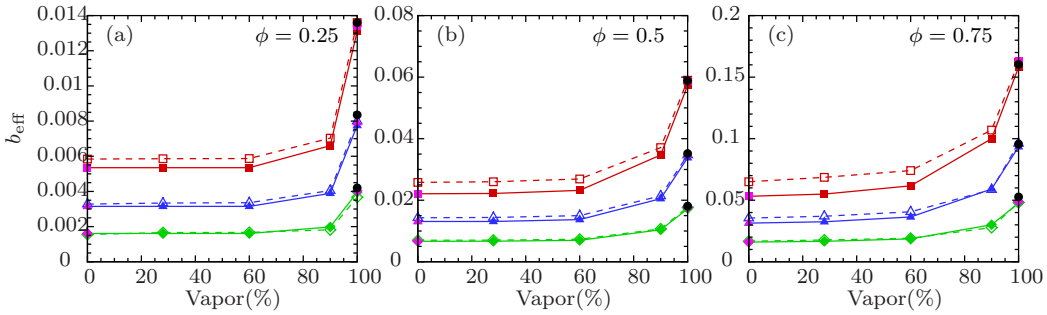

Figure 3.5: Effective slip length comparison. The open symbols stand for the DNS result; the solid colored ones are from the analytical solution of equation (3.24); the black dots are VOF simulations results; the purple symbols are predicted by equations (3.28) and (3.29). –□–, case I7; –△–, case I12; –◇–, case I25.

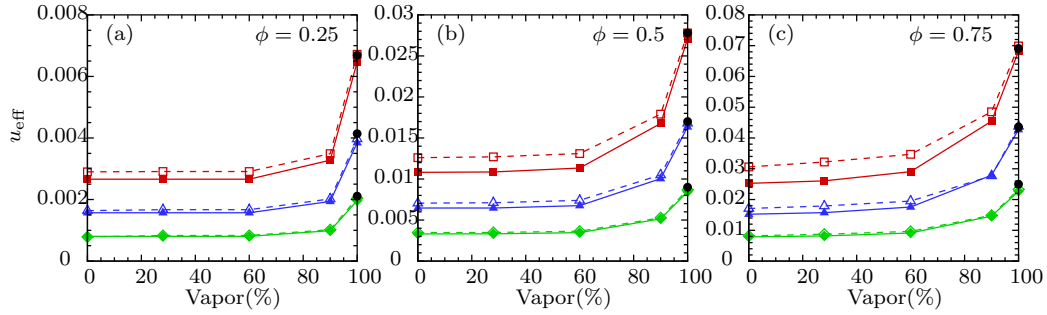

Figure 3.6: Effective slip velocity comparison. The open symbols stand for the DNS result; the solid ones are from the analytical solution derived in this chapter. The black dots are VOF simulations results. –□–, case I7; –△–, case I12; –◇–, case I25.

3.3.2 Results

The drag reduction originally predicted in [33] is based on constant pressure drop:

$$\mathrm{DR}_{\mathrm{ZS,CPD}} = \frac{Q_{\mathrm{no-slip}} - Q_{\mathrm{SHS}}}{Q_{\mathrm{no-slip}}} = 3\left(1 - \frac{B_1}{B}\right), \tag{3.18}$$

where $B_1 = \frac{K(k_1)}{K'(k_1)}\frac{2H}{w}$, $B = \frac{w+d}{w}$. For a constant flow rate, the drag reduction is defined by equation (3.1) and the theoretical solution by Philip [33] can be converted to:

$$\mathrm{DR}_{\mathrm{ZS,CFR}} = \frac{3(B - B_1)}{4B - 3B_1}, \tag{3.19}$$

where the subscripts "CPD" and "CFR" denote constant pressure drop and constant flow rate respectively. Using the partial slip concept expressed in equation (3.5), with the B_0 derived in equation (3.14), the DR in a channel flow with grooved wall on one side can be solved analytically:

$$\mathrm{DR} = \frac{3\zeta}{4\zeta + 1} \tag{3.20}$$

where $\zeta = B_0(w+d)/(2H)$. Figure 3.4 compares the analytical drag reductions predicted by equation (3.20) and DNS results of cases F7–F25 and I7–I25 in table 3.1 with the approximate boundary condition given by equation (3.5). The modeled simulations agree with multiphase VOF simulations. Also, it shows good agreement between the analytical solution and the DNS results for cases F12, F25, I12. and I25, whose size of the texture is relatively small compared to the channel height, consistent with the assumption. For case I7, The deviation is large when $\phi = 0.75$ or when the channel height is comparable to the groove.

The effective slip length b_{eff} for a pipe flow with periodic no-slip or no-shear slots was derived in [34] using bulk quantities such as flow rate and pressure drop. For a plane channel flow, we obtain:

$$b_{\mathrm{eff}} = -\frac{12\frac{QH}{W} - 1}{12\frac{QH}{W} - 4}, \tag{3.21}$$

where all lengths are normalized by the channel height H, the velocities are normalized

by KH^2/μ, and Q is the nondimensionalized volume flow rate.

Using the expression for Q in [32], equation (3.21) yields the zero-shear model effective slip length:

$$b_{\text{eff}-\text{ZS}} = \frac{B}{B_1} - 1. \tag{3.22}$$

From equation (3.19):

$$\text{DR}_{\text{ZS,CFR}} = \frac{3b_{\text{eff}-\text{ZS}}}{4b_{\text{eff}-\text{ZS}} + 1}. \tag{3.23}$$

Note that the drag reduction of a CPD channel can be written as $\text{DR}_{\text{ZS,CPD}} = 3[1 - 1/(1 + b_{\text{eff}-\text{ZS}})]$. In [109], the drag reduction in a Couette flow between two surfaces of distance h with a slip length δ on one surface has a similar form: $\text{DR} = 1 - 1/(1 + \delta/h)$, where δ/h can be seen as the effective slip length in a Couette flow.

Comparing to equation (3.23), we observe that

$$b_{\text{eff}} = \zeta. \tag{3.24}$$

In the same manner as the definition of the effective slip length, the effective slip velocity u_{eff} can be defined as

$$u_{\text{eff}} = \frac{2QH}{W} - \frac{1}{6}. \tag{3.25}$$

And the analytical solution of the effective slip velocity for the zero-shear model is:

$$u_{\text{eff}-\text{ZS}} = \frac{1}{2}\left(1 - \frac{B_1}{B}\right). \tag{3.26}$$

Written in terms of the analytical solution obtained, the effective slip velocity is:

$$u_{\text{eff}} = \frac{\zeta}{2(\zeta + 1)}. \tag{3.27}$$

Figures 3.5 and 3.6 compare the DNS results with equations (3.24) and (3.27) and VOF simulations respectively. Similar to the plots of drag reduction, the solution performs best when the size of the groove is small compared to the channel.

3.3.3 Scaling law for the drag reduction

To use equation (3.23) as a scaling law, one must know b_{eff} *a priori*. A theoretical prediction for b_{eff} is needed for three scenarios: (i) fully wetted grooved surface; (ii) partially wetted grooved surface; and (iii) grooves filled with gas.

When the depth of the fully wetted groove is large enough, which is true for the models in this chapter, b_{eff} of the grooved surface asymptotes to

$$b^{i}_{\text{eff}} = \frac{(w+d)}{2H\pi}\left[(1-\phi)\ln(1-\phi)+(1+\phi)\ln(1+\phi)\right], \tag{3.28}$$

which has been solved in [110] using the conformal mapping method and validated by Wang [57] for all $f \geq 2$ in the notation of this paper. The superscript ^{i}, ^{ii}, ^{iii} represents the scenarios itemized above. The b^{i}_{eff} for all the fully wetted simulations F7–F25 and all the flat interface simulations I7–I25 are computed and plotted against the DR results in figure 3.7 as the gray shaded area. Note that since b^{i}_{eff} is not a function of the gas height, the results do not fall onto one line.

When the surface has zero-shear boundary condition, the exact expression for b_{eff} in [111] can be converted to be

$$b^{iii}_{\text{eff}} = \frac{-(w+d)}{H\pi}\ln\left[\cos\left(\frac{\pi}{2}\phi\right)\right]. \tag{3.29}$$

Similarly, the b^{iii}_{eff} for each simulation result is computed; the $b^{iii}_{\text{eff}}-$DR results are plotted in figure 3.7 as the blue shaded area. Again, because b^{iii}_{eff} is independent of the gas height, the results do not collapse.

Taking into account those two extreme conditions, b^{ii}_{eff} is a function of the groove geometry (w, d, b, H) and the shear rate of the interface (approximated by μ_r, h). The expression for b^{ii}_{eff} is

$$b^{ii}_{\text{eff}} = \frac{(w+d)}{2H}B_0, \tag{3.30}$$

where B_0 is from equation (3.14). $b^{ii}_{\text{eff}}-$DR relations from fully wetted and flat interface results are presented in figure 3.7 as symbols. The solid line is the prediction by equation (3.23). The figure shows that DR satisfies the scaling with respect to b^{ii}_{eff} derived

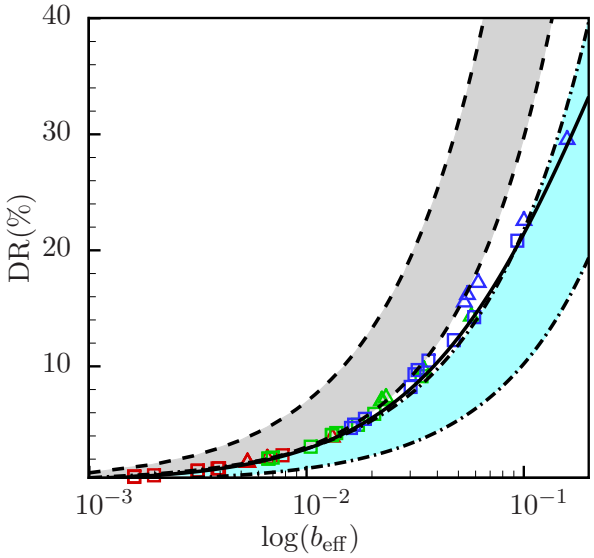

Figure 3.7: DR scales with b_{eff}. Solid line: equation (3.23); red: $\phi = 0.25$; green: $\phi = 0.5$; blue: $\phi = 0.75$; $\triangle$: cases F7 and I7; $\square$: cases F12 and I12; $\Diamond$: cases F25 and I25; blue shaded area: prediction by Wang [57]; gray shaded area: prediction by Ybert et al. [111].

in equation (3.30). The drag reductions DR of all the fully wetted grooved cases and all the flat interface cases, plotted against b_{eff}, collapse onto a single line. To conclude, equation (3.28) can only predict the b_{eff} of scenario (i); equation (3.29) can only predict scenario (iii); however, the analytical solution in this chapter bridges the gap between these two scenarios. Figure 3.7 shows that our solution performs well over the full range of the gas portion.

3.3.4 A first order approximation using analytical solution

In [40], the relation between the effective slip length and the friction factor-Reynolds number product is

$$b_{\text{eff}} = 2\left(\frac{8}{fRe} - \frac{1}{12}\right). \tag{3.31}$$

In this section, the analytical solution is examined with the experimental data in [40] by estimating a 16% liquid penetration and the interface being flat. Figure 3.8 shows

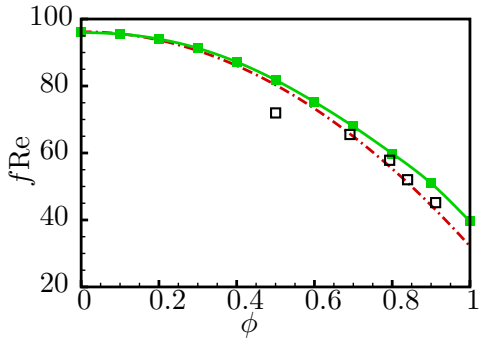

Figure 3.8: Comparison of fRe with varying groove fractions ϕ. ■ analytical solution with 16% liquid penetration; □ experimental results by Maynes et al. [40]; ·— VOF simulation of flat interface with 16% liquid penetration.

that the analytical solution agrees with experiment data, especially when the coverage ratio is small. However, this approximation using the gas to liquid fraction inside the groove is strictly valid only when the channel height is large relative to the penetration; or when the contact angle is low so that the interface can be assumed to be flat.

3.4 A note on interface curvature

3.4.1 Predicting meniscus shape

Interface curvature can be modeled using the Young-Laplace equation:

$$\Delta p = \sigma \nabla \cdot \mathbf{n}, \tag{3.32}$$

where Δp is the pressure difference across the interface, σ is the gas-liquid surface tension, and $\mathbf{n}$ is the local normal. Assuming Δp to be constant along the interface, the interface shape for a groove is

$$F_{zz} = \xi(1 + F_z^2)^{3/2}, \tag{3.33}$$

where $\xi = \Delta p/\sigma$. A three-dimensional expression is given in [112]. Integrating equation 3.33 twice with the boundary conditions $F(\pm\frac{w}{2}) = 0, F_z(0) = 0$ yields the interface

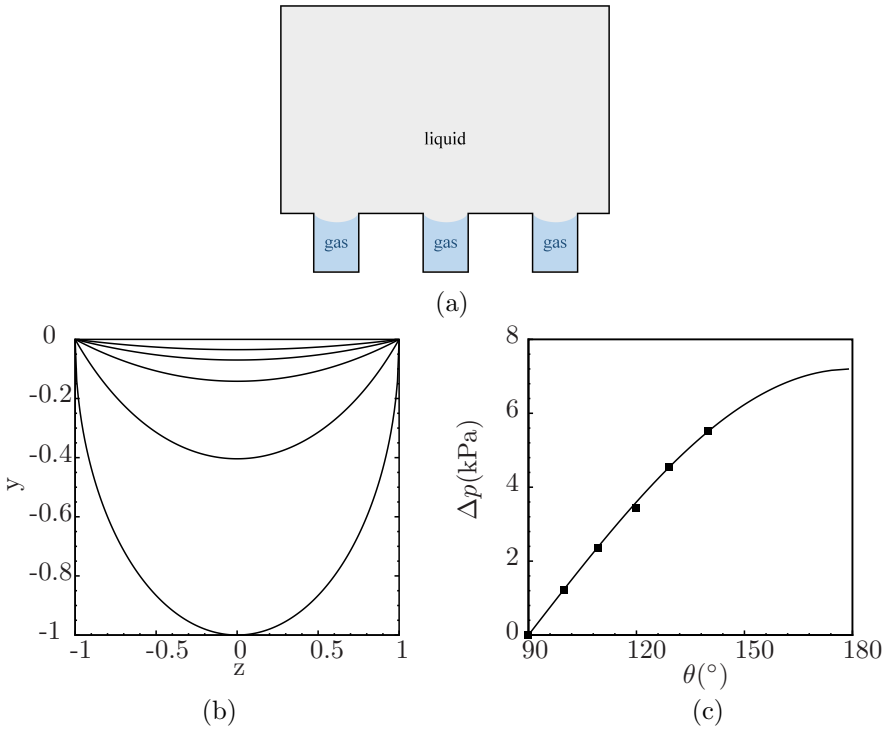

Figure 3.9: (a) Schematic diagram of the meniscus interface. (b) The shape of the gas-liquid interface changes with increasing pressure difference. From top to bottom: Δp = 500, 1000, 2000, 5000, 7200 Pa, from top to bottom. Unit: 10 μm (c) Contact angle θ vs Δp. The solid line represents the analytical solution. The symbols are VOF results.

shape:

$$F(z) = -\frac{\sqrt{1-\xi^2 z^2}}{\xi} + \frac{\sqrt{1-\xi^2 w^2/4}}{\xi}. \tag{3.34}$$

Figure 3.9(b) shows the interface shapes for varying pressure difference. As the pressure difference increases, the interface penetrates towards the bottom of the groove and contact angle increases. VOF simulations of the same configuration were performed and compared to the results of the Young-Laplace equation; good agreement was observed [figure 3.9(c)].

3.4.2 Wetting: failure

The slope of the interface is

$$\eta = F_z = \tan(\theta - \pi/2), \tag{3.35}$$

therefore

$$\xi = -\frac{\eta}{(w/2)\sqrt{1+\eta^2}} = \frac{2\cos\theta}{w}, \tag{3.36}$$

which is similar to equation (1.1) from [55] when $\phi_g \approx \phi = w/(w+d)$.

A critical pressure difference Δp_{cr} can be defined as the pressure difference across the meniscus when contact angle $\theta = \pi$, provided that the groove is deep enough so that the interface does not touch the bottom first. The slope of the interface at $z = w/2$,

$$\lim_{\eta \to -\infty} \xi = \frac{2\cos(\pi)}{w} = \frac{2}{w}. \tag{3.37}$$

The critical pressure difference which quantifies failure due to wetting on the sides is:

$$\Delta p_{cr} = \frac{2\sigma}{w}. \tag{3.38}$$

in this chapter, for case F7 with $\phi = 0.5$, $\sigma = 7.2E-2$ N/m for water at 20°C, $\Delta p_{cr} = 7.2$ kPa.

3.4.3 Results

Simulations are performed to study the effect of the interface curvature in the grooved channel using both the VOF method, and DNS of the liquid region alone, while modeling the curved interface using equation (3.33). The modeled simulations used the approximate boundary condition equation (3.5) at the curved interface, whose height varies across the span of the groove. Figure 3.10 shows the variation in drag reduction with respect to contact angle θ and pressure difference Δp. Good agreement is observed between the VOF calculations and the calculations with the approximate boundary condition. Intriguingly, drag reduction initially increases with increasing Δp and θ following

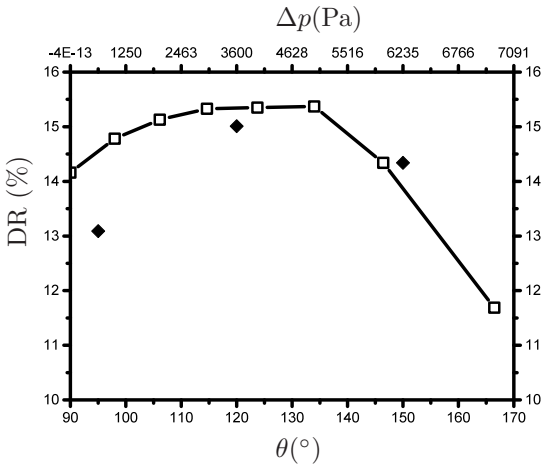

Figure 3.10: Variation of drag reduction with contact angle θ and pressure difference Δp. (Open symbols are approximate boundary condition with meniscus shape simulations; solid symbols are VOF simulations).

which it decreases. Such a trend is also observed in [41, 46, 47]. This behavior is due to the competing effects of interface area and height of the interface from the no-slip wall. The large reductions in drag obtained for $\Delta p < 5$ kPa results from the increase in the surface area over which larger slip velocities occur. For larger Δp, the interface approaches the bottom of the groove where the gas layer is thin, which results in the slip velocity decreasing and therefore the total shear stress is greater on the interface than that on an interface with lower Δp.

3.5 Asymptotic analysis of the analytical solution

By modifying the shear rate matching between regions I and II in the solution of [57], it is straightforward to analytically solve the Stokes shear flow over grooves filled with gas:

$$\frac{\partial u_{\mathrm{I}}(-b^{\mathrm{w}}, z)}{\partial y} = \mu_r \frac{\partial u_{\mathrm{II}}(-b^{\mathrm{w}}, z)}{\partial y}.x \tag{3.39}$$

Here the superscript "w" is used to represent Wang's notation. b^{w} is the depth of the groove normalized by $(w + d)/2$. The expression for B_0 and B_m remain the same (see

[57] for detailed solution) and the matrix integrated from equation (3.39) becomes

$$\sum_{n=1}^{\infty} -B_n^{\mathrm{w}} L_{nm}\gamma_n - \frac{(-1)^m}{\alpha_m} = \mu_r \frac{a}{2} A_m^{\mathrm{w}} \alpha_m \left[1 + e^{-2\alpha_m b^{\mathrm{w}}}\right]. \tag{3.40}$$

Moreover, the fully wetted solution by Wang [57] can be recovered from the partial slip solution. When gas escapes from the liquid, $g = 0$, $f = b^{\mathrm{w}}$, $\mu_r = 1$. Taking the limit of the right hand side (RHS) of equation (5.27),

$$\begin{aligned}\lim_{g\to 0} \mathrm{RHS} &= \lim_{g\to 0} \frac{a}{4} C_m \alpha_m \left[-e^{\alpha_m (b^{\mathrm{w}}+2g)} + e^{\alpha_m b^{\mathrm{w}}}\right] \left[(\frac{\mu_r}{g\alpha_m} + 1)e^{\alpha_m b^{\mathrm{w}}} + (\frac{\mu_r}{g\alpha_m} - 1)e^{-\alpha_m b^{\mathrm{w}}}\right] \\ &= \frac{a}{2} C_m (-e^{2\alpha_m b^{\mathrm{w}}}) \alpha_m \left[1 + e^{-2\alpha_m b^{\mathrm{w}}}\right]. \end{aligned} \tag{3.41}$$

Comparing to the solution for fully wetted grooves: $C_m(-e^{2\alpha_m b}) = A_m^{\mathrm{w}}$.

Taking the limit of equation (3.14) and applying L'Hoȋtal's rule, and substituting C_m,

$$\begin{aligned}\lim_{g\to 0} B_0 = \lim_{g\to 0} &- \sum_{n=1}^{\infty} \frac{1}{2} C_n \frac{(-1)^n}{\alpha_n} \left[-e^{\alpha_n (f+2g)} + e^{\alpha_n f}\right] \\ &\times \left[(\frac{\mu_r}{g\alpha_n} + 1)e^{\alpha_n f} - (\frac{\mu_r}{g\alpha_n} - 1)e^{-\alpha_n f}\right] \\ = &- \sum_{n=1}^{\infty} \frac{(-1)^n}{\alpha_n} A_n^{\mathrm{w}} (1 - e^{-2\alpha_n b^{\mathrm{w}}}). \end{aligned} \tag{3.42}$$

Similar to B_m from equation (3.15):

$$\begin{aligned}\lim_{g\to 0} B_m =& \lim_{g\to 0} \sum_{n=1}^{\infty} C_n L_{mn} \left[-e^{\alpha_n (b^{\mathrm{w}}+2g)} + e^{\alpha_n b^{\mathrm{w}}}\right] \left[(\frac{\mu_r}{g\alpha_n} + 1)e^{\alpha_n b^{\mathrm{w}}} - (\frac{\mu_r}{g\alpha_n} - 1)e^{-\alpha_n b^{\mathrm{w}}}\right] \\ =& 2 \sum_{n=1}^{\infty} A_n^{\mathrm{w}} L_{mn} (1 - e^{-2\alpha_n b^{\mathrm{w}}}). \end{aligned} \tag{3.43}$$

Thus, the solution in [57] for fully wetted grooves is recovered from the partial-slip solution. Also, the solution for fully wetted grooves can be converted to full-gas solution with minor adjustments, as is shown in equation (3.40).

3.6 Summary

Multiphase, feature-resolved simulations have been performed to study the factors that contribute to the drag reduction effect of SHS: interface shear rate and the shape of the gas-liquid interface. First, VOF simulation results confirmed that the gas flow behavior inside the groove has an effect on drag reduction but the liquid penetration into the grooves is more significant. Next, an analytical solution of the shear flow over longitudinal grooves with coupled gas-liquid interface has been derived and validated with simulations using approximate gas-liquid boundary condition and VOF simulations. A scaling law of the drag reduction with respect to effective slip length has been obtained from the analytical solution. The solution can also be extended to liquid-infused surfaces. Consider for example two of the liquid conditions in the experiment of [48], $\mu_r = 1/2.7$ and 30, and the geometric parameters of case I7 with the grooves filled with a second fluid; the analytical solutions predict the drag reduction to be 9.50% and 0.35% respectively. Lastly, the shape of the interface has been examined by prescribing the location of the interface with the Young-Laplace equation and applying the approximate boundary condition. A series of physically representative meniscal interfaces which provided spanwise varying gas height in the groove have been simulated. For the meniscal cases, the drag reduction does not behave monotonically but peaks at a certain meniscal interface and then drops dramatically. This result can be explained as a compromise between the gas-liquid contact area and the shear stress on the gas-liquid interface. When liquid penetrates into the groove, the interface area increases but the local gas is depressed, which increases the shear stress on the interface. This behavior is also confirmed by VOF simulations.

Chapter 4

Turbulent flow over longitudinal grooved surfaces

DNS is used to study the geometric effect of grooved surfaces with feature size comparable to realistic SHS at a moderate Reynolds number $Re_\tau = 400$. Also, a model problem of unsteady Stokes flow over grooved surfaces is introduced. This chapter is organized as follows. §4.1 presents the numerical methodology and the cases studied. In §4.2, the results of the simulations are discussed. Unsteady Stokes flow over grooved surfaces is presented in §4.3. A summary in §4.4 concludes the chapter.

4.1 Simulation parameters

Throughout this chapter, x, y and z denote streamwise, wall-normal and spanwise directions, respectively. The mean and instantaneous velocity vectors are denoted by $(\overline{U}, \overline{V}, \overline{W})$ and (u, v, w) in the $x-$, $y-$, and $z-$ directions, respectively. The prime symbol $(')$ represents fluctuating variables. Density is assumed constant. All simulations in this chapter are performed at $Re_\tau = 400$, and all wall boundaries are treated as no-slip. The channel is periodic in spanwise and streamwise directions.

Figure 4.1 describes the grooved channel geometry and the coordinate system, where w, d, h, ϕ denote the groove's width, spacing, depth, and coverage ratio $\phi = w/(w + d)$

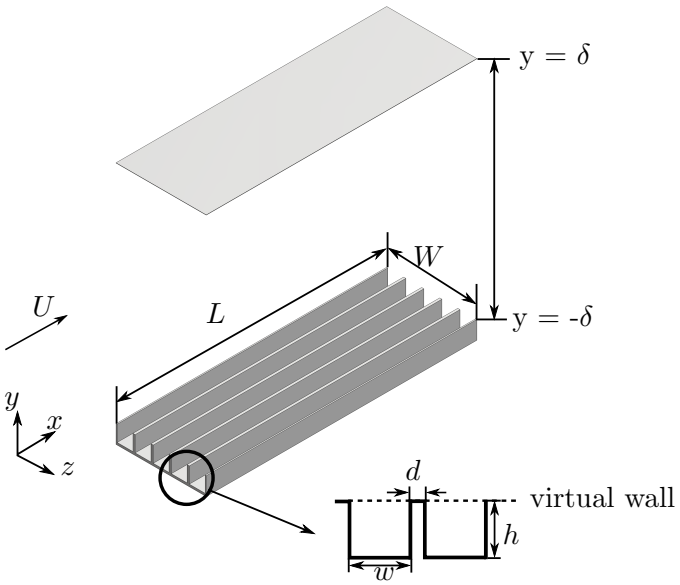

Figure 4.1: The channel geometry and groove configuration. x, y and z denote streamwise, wall-normal and spanwise directions respectively.

respectively. The channel half-height δ is unity for all cases. The bottom reference plane is taken to be the ridge tip $y = -\delta$ in analogy to the flat-wall channel. This choice of the reference plane raises the issue of virtual origin, which is discussed in detail in §4.2.1. Because the channel is asymmetric, the wall-shear stresses on the top and bottom planes are different. in this chapter, a superscript '+' denotes that a quantity is normalized by the *local* wall-shear velocity u_τ obtained from the wall-shear stress averaged over the corresponding plane.

As listed in table 4.1, four DNS at $Re_\tau = 400$ with different surface configurations are performed. C0 is the baseline and is validated against the data of [113] at $Re_\tau \approx 395$. The mean velocity profiles and turbulent intensities are in good agreement with [113] (figure 4.2). C1 is a turbulent channel with one groove on the bottom wall to study the effect of an isolated groove. C320 and C160 are turbulent channels with 320 and 160 grooves mounted on one wall. The computational domain is $2\pi \times 2 \times \pi$ for C0 and $6.58 \times 2 \times 3.29$ for the other cases to resolve an integer number of grooves. The

Case	Surface	$(w+d)^+$	h^+	$\phi(\%)$	Δx^+	$\Delta y^+_{\min}$	Δy^+_c	$\Delta z^+_{\min}$	$\Delta z^+_{\max}$	$N_x \times N_y \times N_z$
C0	Flat (—)	–	–	–	7.78	0.40	6.38	3.20	3.20	$323 \times 210 \times 393$
C1	Unit groove (■)	1316.57	3.60	0.27	11.45	0.40	6.00	0.257	3.20	$230 \times 323 \times 601$
C320	320 grooves (○)	4.11	3.60	87.50	11.45	0.40	6.00	0.257	0.257	$230 \times 323 \times 5123$
C160	160 grooves (▲)	8.23	7.20	87.50	11.45	0.40	6.00	0.514	0.514	$230 \times 323 \times 2561$

Table 4.1: Parameters for the simulations of channel flow with unit groove and 320 grooves and 160 grooves. The symbols apply for the following figures.

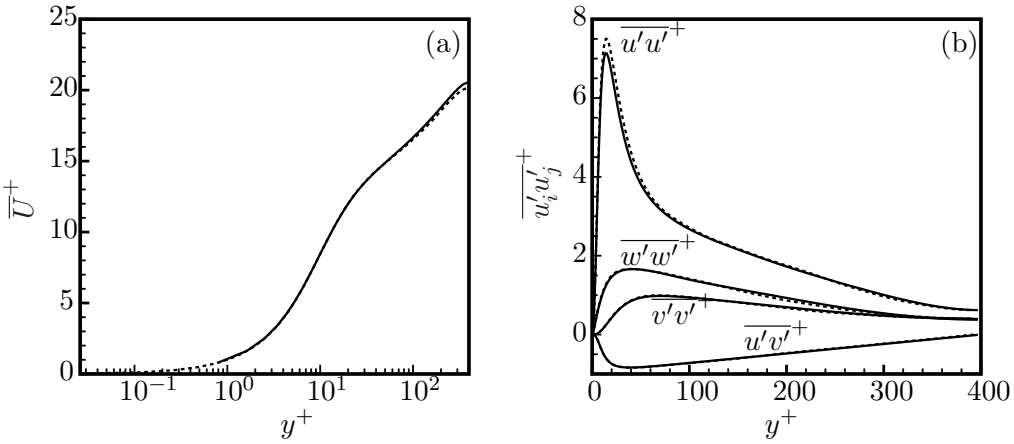

Figure 4.2: Mean profiles for the smooth wall channel (—) at $Re_\tau = 400$ and [113] (- - -) data at $Re_\tau \approx 395$. (a) $\overline{U}^+$–y^+ (b)$\overline{u_i'u_j'}$–y^+

domain length is evaluated using the correlation plots in section 4.2.6. Note that all spatial correlations decay to zero at $y^+ = 5$. The resolution of the channel is outlined in table 4.1. The resolution of the ridge in the span is $\Delta z^+ = 0.257$ in wall units for C1 and C320 which is much finer than the resolution in a flat-wall DNS of $\Delta z^+ = 3.2$. Also, the near-wall turbulent kinetic energy spectra decays up to 6 decades at the wavenumber $k_z = \pi/\Delta z$ (not shown). In the grid refinement study by Choi et al. [70], refining the grid from $\Delta z^+ = 0.64$ (finest case in [70]) to $\Delta z^+ = 0.32$ changes the drag on the riblet surface by less than 1%. The computational cost for the largest simulation is 700 hours using 7968 Blue Gene/Q processors.

Case	$\epsilon_1 \times 10^{-3}$	$\epsilon_2 \times 10^{-3}$	$\epsilon_3 \times 10^{-3}$	ϵ_4
C0	-	-	-	-
C1	-0.4	-	0	0
C320	-2.0	$(-1.3, -1.7)$	-1.5	0
C160	-4.4	$(-2.6, -3.4)$	-3.0	0

Table 4.2: Virtual origins relative to $y = -\delta$ computed using [114] (ϵ_1), [77] (ϵ_2), [57] (ϵ_3) and the ridge tip (ϵ_4).

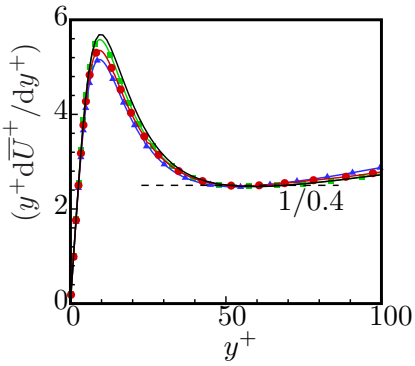

Figure 4.3: $y^+ \mathrm{d}\overline{U}^+/\mathrm{d}y^+$ as a function of y^+.

4.2 Results

4.2.1 Virtual origin

Before discussing the statistics, the choice of the virtual origin for which there exist multiple choices is discussed, since it might affect the mean profiles. In experiments, the virtual origin is determined from the modified Clauser chart method. For the current Reynolds number, the logarithmic region is not wide enough (figure 4.3) to yield an accurate estimation [70, 115]. Alternatively, one can employ the mean momentum absorption plane method introduced by Thom [114]. Here, the virtual origin relative to $y = -\delta$,

$$\epsilon_1 = \int_{-\delta-h}^{-\delta} y F_d(y) \mathrm{d}y \Big/ \int_{-\delta-h}^{-\delta} F_d(y) \mathrm{d}y - \delta, \tag{4.1}$$

Case	k^+_{rms}	τ^B/τ_{w0} (groove)	τ^B/τ_{w0} (ridge)	τ^B_w/τ_{w0}	τ^T_w/τ_{w0}	$\mathrm{DR_{SS}}(\%)$	$\mathrm{DR}(\%)$	b^+	ΔU^+
C0	0.00	1.00	1.00	1.00	1.00	0.00	0.00	0.00	0.00
C1	0.16	0.47	1.00	1.00	1.00	0.17	0.00	0.00	0.00
C320	3.36	0.80	2.35	0.99	1.01	1.01	0.16	0.71	0.10
C160	6.73	0.76	2.45	0.98	1.02	2.48	0.53	1.24	0.35

Table 4.3: A summary of wall-shear stress, effective slip length b^+, $\mathrm{DR_{SS}}$ and DR drag reduction. τ_{w0} is the averaged wall-shear stress between the top and bottom walls. τ^B_w and τ^T_w are the mean shear rate on the bottom and top walls respectively. ΔU^+ is the roughness function.

where $F_d(y)$ is the total drag acting on the grooves averaged over time and (x, z). This method was also applied in [115] for sinusoidal roughness in pipe flow.

A second method is to use the 'protrusion height' ϵ_2 of riblets obtained by Luchini et al. [77] using conformal mapping. In [77], the groove shapes are chosen to be sinusoidal, triangular or parabolic, so we can only estimate the range of the virtual origin for the current square groove shape. A third choice is to apply the analytical solution of unsteady Stokes flow over the grooved surfaces introduced in [57] to compute the slip length, which yields the virtual origin ϵ_3. A final option is to apply the same argument as Chan et al. [115] to compute the volume integral of the streamwise momentum equation, and find the equivalent channel height where the wall-shear stress represents the drag acting on the projected area of the grooved surfaces. For a constant pressure gradient flow, this is also the height of the bulk channel. Table 4.2 summarizes the virtual origins computed using these four methods. The locations are all below or equal to the ridge tip, as expected for longitudinal riblets within the viscous sublayer. C160 has the largest offset, but it is less than 2 in wall units. Therefore, the location of the virtual origin is defined as the ridge tip.

4.2.2 Change in drag

The statistics are temporally averaged over at least 25 large-eddy-turnover times δ/u_τ after the flow is fully developed, then spatially averaged in both spanwise and streamwise

directions over all spanwise grooves. The data inside the grooves is multiplied by the coverage ratio ϕ using the superficial spatial average introduced in [116]. As a result, the data below $y = -\delta$ contains information from every point inside the groove at the same depth. The change in wall-shear stress, effective slip length b^+, wall-shear stress reduction $\mathrm{DR_{SS}}$ and overall drag reduction DR are listed in table 4.3, where 'groove' refers to the averaged shear stress over the grooves alone at $y = -\delta$; 'ridge' refers to the averaged shear stress over the ridges alone. The total shear stress is determined from $\tau_w = \mu \frac{\mathrm{d}\overline{U}}{\mathrm{d}y} - \rho\overline{u'v'}$ at $y = -\delta$. The groove height is converted to a roughness parameter defined as $k^+_{\mathrm{rms}} = h^+\sqrt{\phi}$ using a square wave to characterize the roughness height $k(z)$, where

$$|k(z)| = \begin{cases} h, & 0 \leqslant \left(\dfrac{z}{w+d} \bmod 1\right) < \phi; \\ 0, & \phi < z \leqslant 1. \end{cases} \tag{4.2}$$

Note that although C1 has the same groove geometry as C320, its k^+_{rms} value is smaller since the k^+_{rms} value not only depends on individual groove size but also the distribution of the roughness element. $k^+_{\mathrm{rms}} < 4$ for C1 and C320, which is presumably within the hydrodynamically smooth regime. No obvious overall drag reduction would be expected. However, there is a significant jump of the wall-shear stress from the averaged shear stress over the groove to the averaged shear stress over the ridge. The low shear stress is caused by the slip velocity induced by the groove, and the high shear stress is imposed by the ridges. For this reason, the shear stress at the reference plane is taken as the average $\tau^B_w = \tau^B|_{\mathrm{groove}}\phi + \tau^B|_{\mathrm{ridge}}(1-\phi)$.

As discussed in [117], the definition of the friction coefficient can cause ambiguity when comparing drag reduction for internal flows, especially when the internal flow is asymmetric about the centerline of the channel. For example, in [7], the reduction of wall friction factor on the bottom wall is 11%, and the channel averaged wall friction factor is only reduced by 6%. The definition of drag reduction varies depending on how the flow is driven: by a constant flow rate (CFR) or by a CPG. The averaged wall-shear

stresses τ_w can be derived from balance of forces:

$$\tau_w^T + \tau_w^B = -2\delta(\mathrm{d}P/\mathrm{d}x), \tag{4.3}$$

where $\mathrm{d}P/\mathrm{d}x$ is the mean pressure gradient. Under CPG condition, the right hand side of equation (4.3) remains unchanged. It is inappropriate to use the skin friction to assess the drag reduction in the current study, as the decreased shear stress at the reference plane at $y = -\delta$ should be counterbalanced by the increased shear stress on the opposite wall $y = \delta$. Therefore, as is done in [26], the change in bulk velocity is used to define DR as:

$$\mathrm{DR} = \frac{\overline{U}_{\mathrm{gr}} - \overline{U}_0}{\overline{U}_0}, \tag{4.4}$$

where $\overline{U}_0$ and $\overline{U}_{\mathrm{gr}}$ denote the averaged bulk velocity between $y = -\delta$ and $y = \delta$ for C0 and the grooved case respectively. The reduction in τ_w ($\mathrm{DR_{SS}}$) is quoted in table 4.3 as a reference and is defined as:

$$\mathrm{DR_{SS}} = \frac{\tau_{w0} - \tau_w^B}{\tau_{w0}}, \tag{4.5}$$

where τ_{w0} is the shear stress on the flat-wall channel, τ_w^B is the averaged shear stress at the bottom reference plane. $\mathrm{DR_{SS}}$ can be interpreted as the amount of drag reduction on the grooved plane.

The effective slip length is defined as:

$$b^+ = \overline{U}_s^+ / (\partial \overline{U}/\partial y)^+, \tag{4.6}$$

where $\overline{U}_s^+$ is the slip velocity at $y = -\delta$, and $(\partial \overline{U}/\partial y)^+$ is the gradient of streamwise velocity at the same location. $b^+ \sim O(1)$ for C320 and C160 implying that locally $\overline{U}_s^+ \sim (\partial \overline{U}/\partial y)^+$.

ΔU^+ is obtained as the difference between the flat-wall log law constant of integration $C = 5.1$ and the rough wall $C - \Delta U^+$ where the logarithmic region overlaps the most with that of the flat-wall [118]. Among the three grooved cases, using the

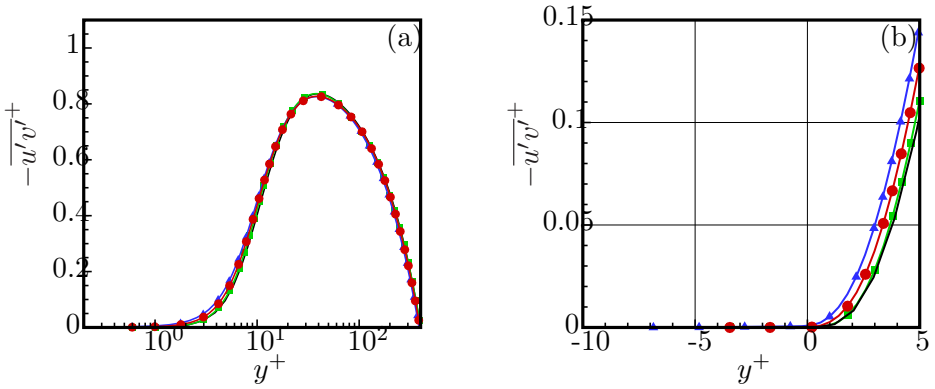

Figure 4.4: (a) Reynolds shear stresses $-\overline{u'v'}^+$. (b) Close-up view. Symbols are consistent with the cases listed in table 4.1.

definition:

$$\Delta U^+ = \frac{1}{\kappa}\ln(k_s^+) + C - B, \quad \text{where} \quad \kappa = 0.40, \quad B = 8.5,$$

$k_s^+ < 4.3$, which falls into the hydrodynamically smooth regime [80].

4.2.3 Wall-shear stresses

Because the channel is asymmetric, the mean flow profiles are asymmetric, too. The linear profile of $\mathrm{d}\overline{U}^+/\mathrm{y}^+$ (not shown) reveals that for the largest grooves, the location of $\mathrm{d}\overline{U}^+/\mathrm{y}^+ = 0$ is shifted by 12 in wall units towards the grooved surfaces, which is within 3 grid points at the channel center. Therefore, the profiles presented in the following only consider the domain $y \in (-\delta - h, 0)$ unless stated.

Reynolds shear stresses over the lower half of the channel flow are compared in figure 4.4(a). The difference from flat-wall behavior is not pronounced. Near the grooved surfaces, Reynolds shear stresses are higher than the flat-wall channel profile. The grooved cases and flat-wall results collapse in the outer region. In linear scale within the viscous sublayer (figure 4.4(b)), C160 has the highest magnitude of $\overline{u'v'}$, which is an outcome of the large slip velocity produced by the large grooves. Noticeably, inside the grooves, the Reynolds shear stresses are nearly zero.

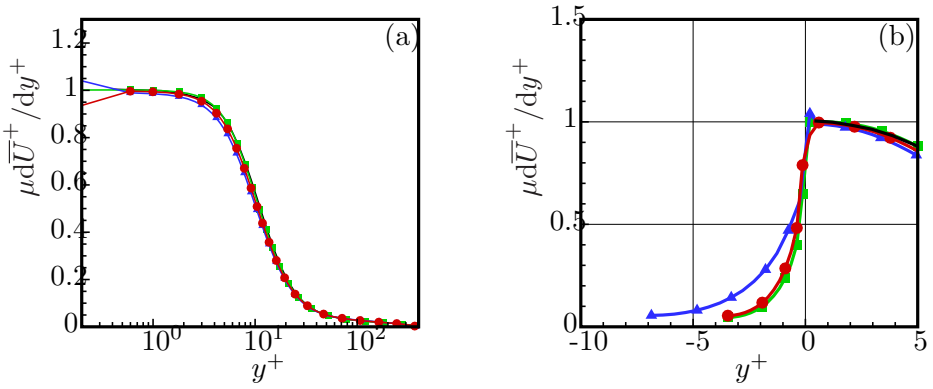

Figure 4.5: (a) Viscous shear stress profiles for the grooved surfaces (symbols) and flat-wall channel (solid line). (b) Close-up view. Symbols are consistent with the cases listed in table 4.1.

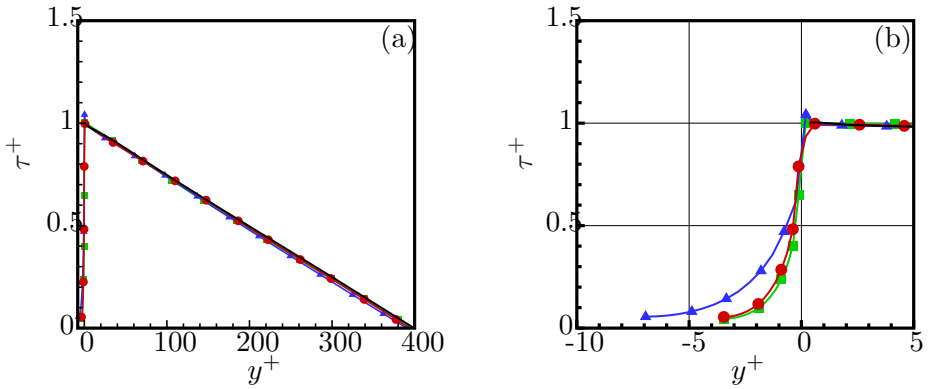

Figure 4.6: (a) Profiles of the total shear stress τ^+. (b) Close-up view. Symbols are consistent with the cases listed in table 4.1.

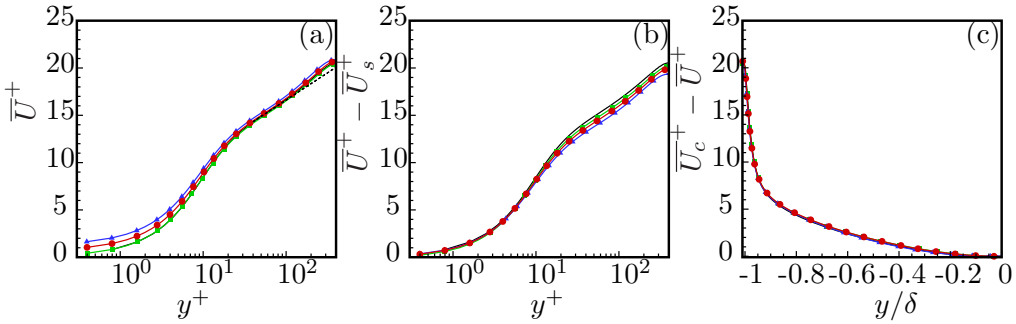

Figure 4.7: (a) Velocity profiles for the grooved surfaces (–symbols–) and flat-wall channel (solid line). The dashed line represents the log law $1/\kappa \ln y^+ + C$, with $C = 5.1$ and $\kappa = 0.40$. (b) Velocity profiles offset with slip velocity of each case respectively. (c) Velocity defect profiles. Symbols are consistent with the cases listed in table 4.1.

The viscous shear stress profiles in figure 4.5(a) show competing phenomena between slip and roughness effects. Large grooves (C160) show the highest viscous shear stress among all cases at $y = -\delta$, but it moves to the lowest than all other cases until $y^+ < 10$. Although small grooves (C320) display a low viscous shear stress near the grooved surfaces, this slip effect does not sustain in the outer region. It is quickly overcome by the external flow. Its profile overlaps with the flat-wall result when $y^+ > 10$. In linear scale, within the groove, the viscous shear stress is higher inside the large groove compared to the other two cases in figure 4.5(b).

The distribution of the total shear stress over the grooved surfaces in figure 4.6(a) collapses over the domain $y \in (-\delta, \delta)$. This supports Townsend's outer-layer similarity hypothesis [119]. in this chapter $\delta/k_s > 93$, which is within the range of $\delta/k_s \geqslant 40$ that Flack et al. [118] reported inside a turbulent boundary layer and the $\delta/k \geqslant 6.75$ range in [115] for pipe flow. When normalized with the local inner units, the total shear stress is 1 at $y^+ = 0$ in figure 4.6(b).

4.2.4 Mean profiles

Profiles of mean streamwise velocity $\overline{U}^+$ are shown in figure 4.7(a). Note that C160 shows the highest slip velocity. All profiles overlap in the buffer layer and above. Figure 4.7(b) shows the profiles offset by the slip velocity for each case. The logarithmic

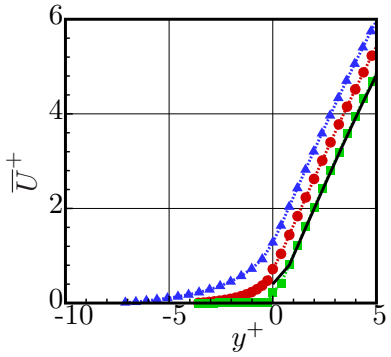

Figure 4.8: Linear scale velocity profiles of the near-wall region. Symbols are consistent with the cases listed in table 4.1.

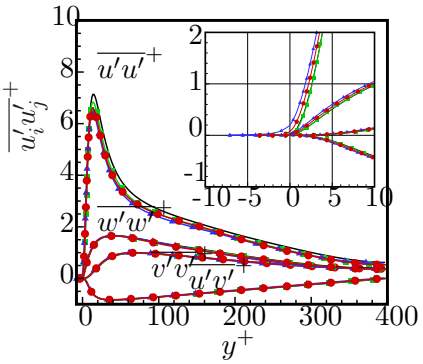

Figure 4.9: Reynolds stress profiles for the grooved surfaces (symbols) and flat-wall channel (solid line). Inset: close-up view of the near-wall region. Symbols are consistent with the cases listed in table 4.1.

region increases towards the wall as the size of the grooves increase. The velocity defect profiles are presented in figure 4.7(c). All profiles collapse on top of the flat-wall data supporting the universal defect profile for rough and smooth walls [118]. Figure 4.8 focuses on the near-wall velocity using a linear scale. Within the viscous sublayer $0 < y^+ < 5$, all profiles remain linear. The profile for C160 shifts the most, which indicates the largest slip velocity.

Reynolds stresses profiles are shown in figure 4.9. The peak values of $\overline{u'u'}$ are lower in magnitude than the flat-wall profile, and shifted slightly towards the grooved wall. Again, the profile for C160 shifts the most and has the lowest peak value. This result is in agreement with the experiments of [7] in which longitudinal SH grooves of comparable order of size were used. Similar trends have also been observed in the DNS of [120] over porous media and in the DNS of [70] over riblets with spacing less than $s^+ = 20$. Other quantities overlap with flat-wall data, indicating a weaker influence by the grooved surfaces. Inside the grooves (inset, figure 4.9), all quantities are small.

4.2.5 Turbulent kinetic energy (TKE)

Figure 4.10 shows the mean profiles of the budget terms of the total TKE for the 4 cases studied in this chapter. For fully developed channel flow, the balance equation for the budgets of TKE can be written as:

$$0 = \underbrace{-\overline{u_i' u_j'} \frac{\partial U_i}{\partial x_j}}_{\text{Production}} \underbrace{-\nu \overline{\frac{\partial u_i'}{\partial x_j} \frac{\partial u_i'}{\partial x_j}}}_{\text{viscous dissipation}} + \underbrace{\nu \frac{\partial^2}{\partial x_j x_j} \frac{1}{2} \overline{u_i' u_i'}}_{\text{viscous diffusion}} \underbrace{-\frac{1}{2} \frac{\partial}{\partial x_j} \overline{u_i' u_i' u_j'}}_{\text{turbulent transport}} \underbrace{-\overline{u_i' \frac{\partial p'}{\partial x_i}}}_{\text{pressure transport}} , \quad (4.7)$$

where the Einstein notation is used. Overall, there is not much difference when each term is normalized with flat-wall units in figure 4.10. This further emphasizes that the channel is hydrodynamically smooth. All quantities are zero inside the grooves. The production for case 160 is slightly reduced, which happens when the near-wall vortices are more organized [121].

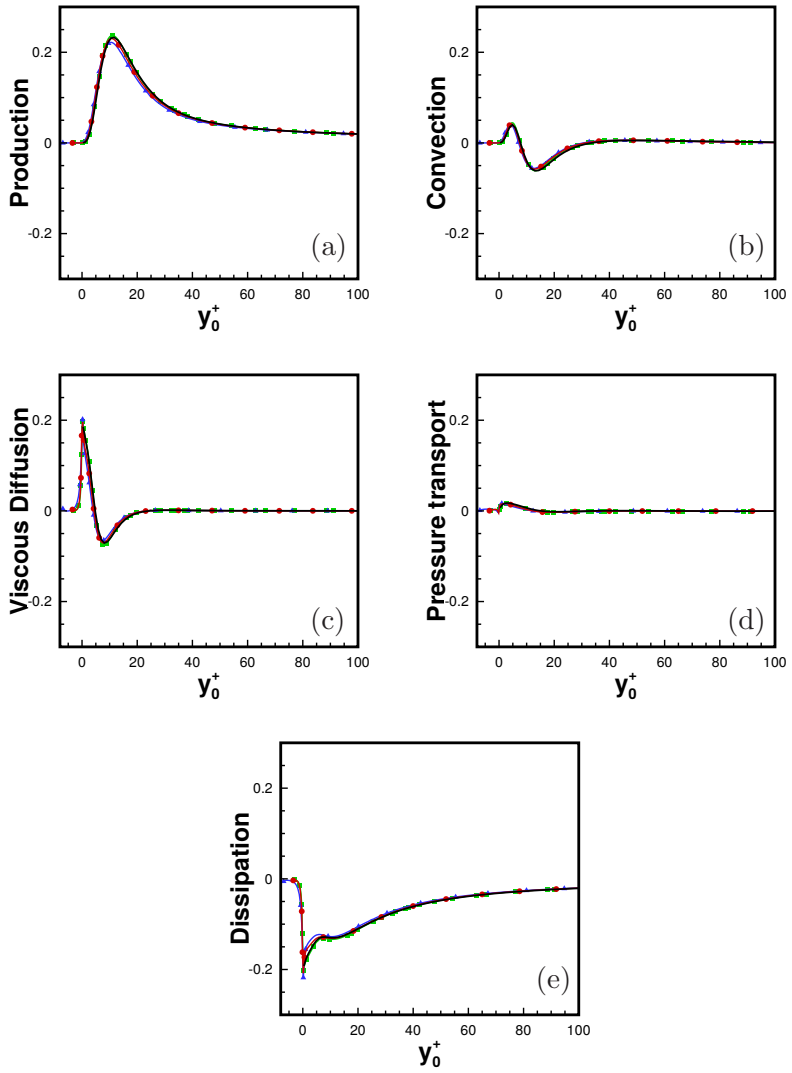

Figure 4.10: TKE budgets normalized by flat-wall scales. The symbols are consistent with the cases listed in table 4.1.

4.2.6 Spatial correlations

Figures 4.11-4.14 shows the correlation and cross-correlation profiles in streamwise and spanwise directions near the bottom walls. After the simulations are statistically stationary, instantaneous fluctuations of variables u_i, p at fixed wall distances are collected over $M = 100$ intervals. The 2D power spectral density at the mth interval ($\Delta T^+ = \Delta t u_\tau^2/\nu = 4$) is

$$\Phi^m(k_1, k_3)|_y = \frac{1}{2}(\hat{f}^m \hat{g}^{m*} + \hat{f}^{m*} \hat{g}^m), \tag{4.8}$$

where $f^m(x, z)|_y$ or $g^m(x, z)|_y$ represents either the velocity fluctuation or the pressure fluctuation at the mth interval, and $\hat{f}^m(k_1, k_3)$ or $\hat{g}^m(x, z)|_y$ is its corresponding 2D discrete Fourier transform. Then the averaged 2D power spectral density at each y location is:

$$\Phi(k_1, k_3)|_y = \frac{1}{M} \sum_{m=1}^{M} \Phi^m(k_1, k_3)|_y. \tag{4.9}$$

$R(\Delta x, \Delta z)$ was obtained by inverse discrete Fourier transforming the corresponding spectrum $\Phi(k_1, k_3)|_y$. The correlations were normalized such that $R_{\mathrm{ff}}(0, 0) = 1$.

The small differences between C1 and other correlation profiles are due to the non-homogeneity of the surface geometry in the domain calculated. All discussions in this subsection are confined to the comparison among C0, C320 and C160. The grooves have no effect outside the viscous sublayer, which is consistent with the hydrodynamically smooth surface condition.

The cross-correlations R_{uv} in streamwise (figure 4.13(a-b)) and spanwise directions (figure 4.14(a-b)) of C320 and C160 are lower than C0, indicating a reduction in the local shear.

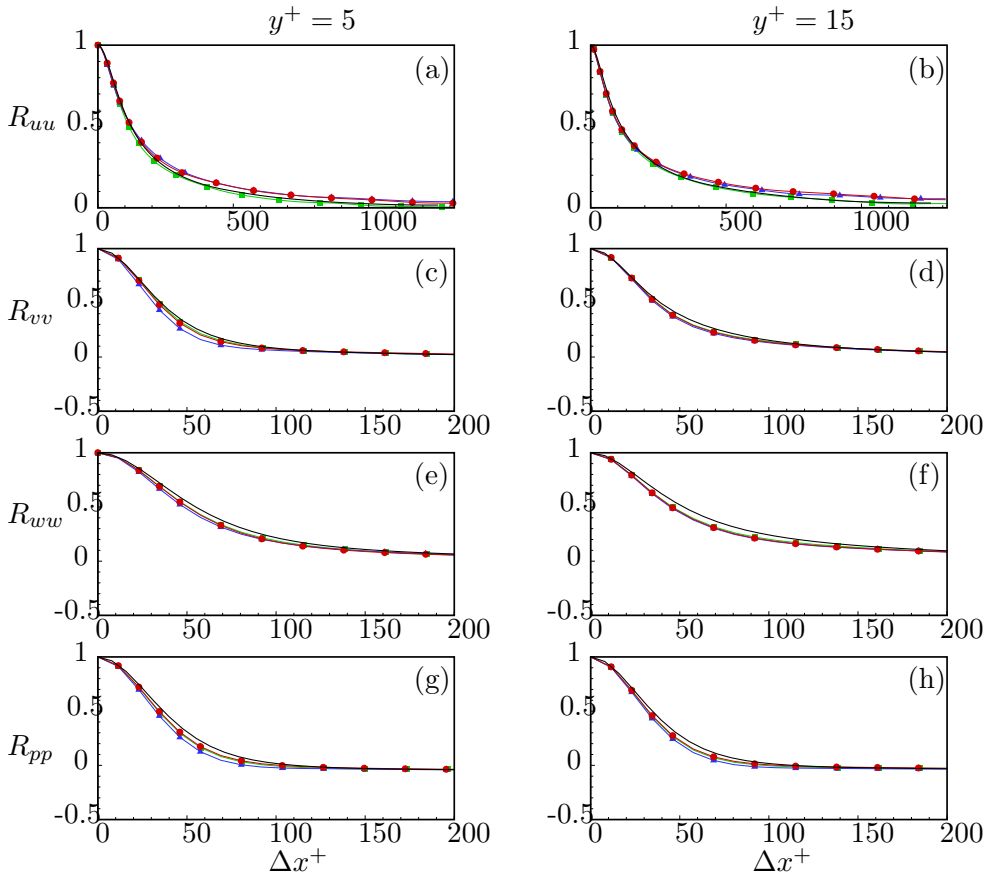

Figure 4.11: Streamwise correlations $R_{uu}, R_{vv}, R_{ww}, R_{pp}$ (a, c, e, g) at $y^+ = 5$; (b, d, f, h) at $y^+ = 15$.

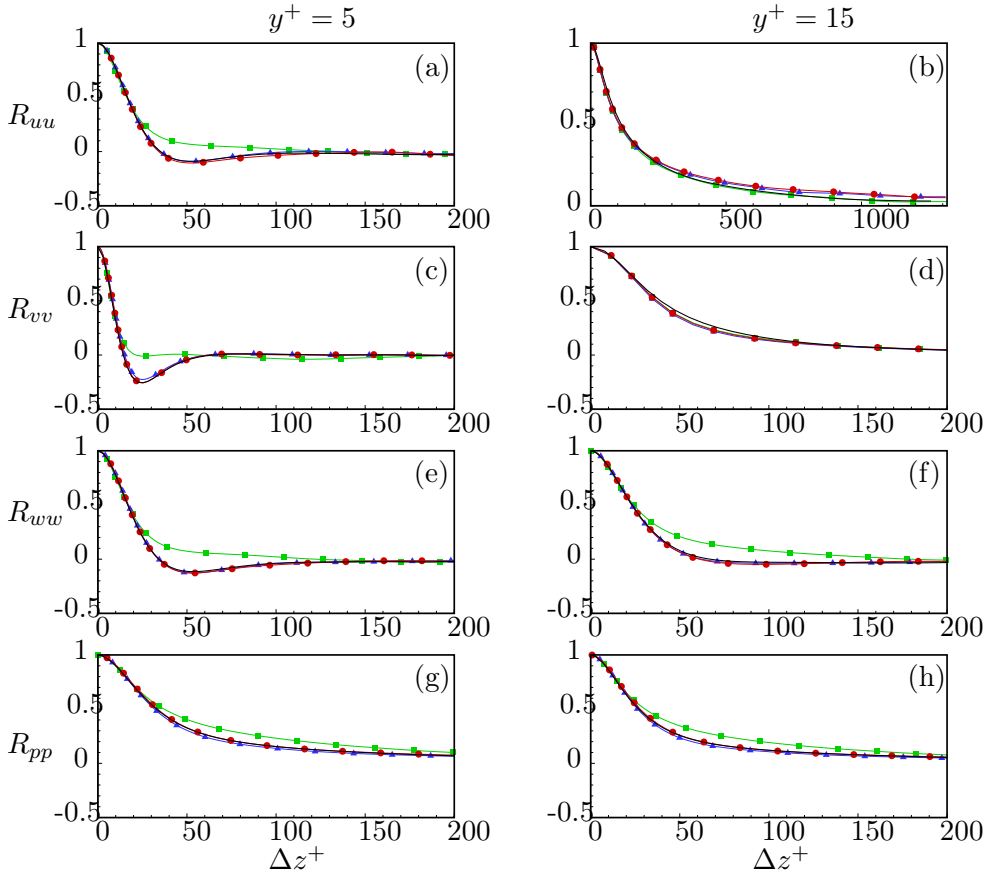

Figure 4.12: Spanwise correlations $R_{uu}, R_{vv}, R_{ww}, R_{pp}$ (a, c, e, g) at $y^+ = 5$; (b, d, f, h) at $y^+ = 15$.

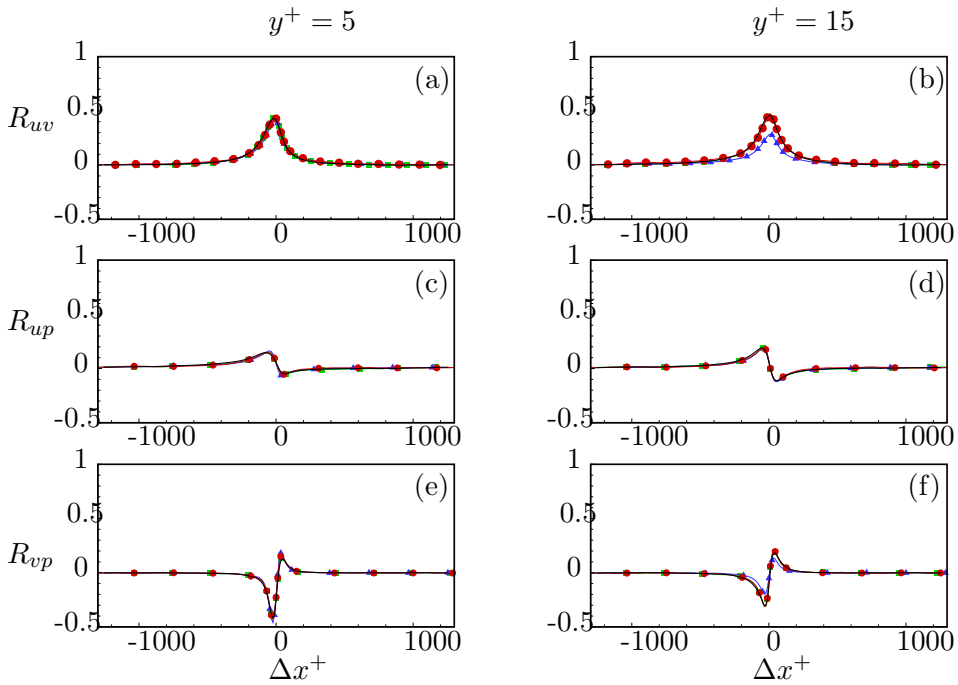

Figure 4.13: Streamwise cross-correlations R_{uv}, R_{up}, R_{vp} (a, c, e) at $y^+ = 5$; (b, d, f) at $y^+ = 15$.

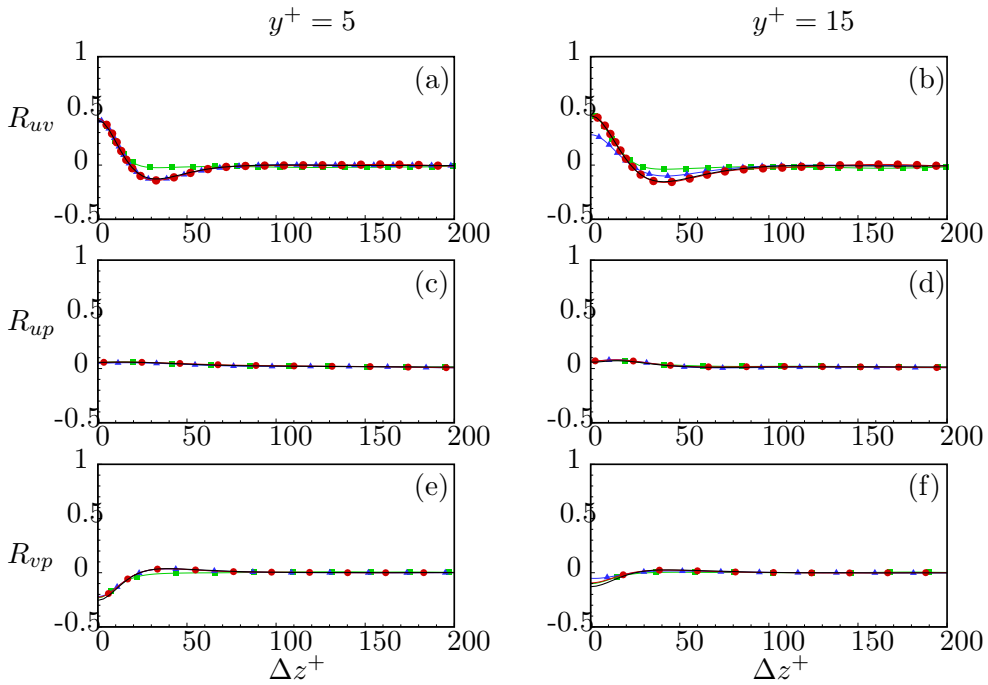

Figure 4.14: Spanwise cross-correlations R_{uv}, R_{up}, R_{vp} (a, c, e) at $y^+ = 5$; (b, d, f) at $y^+ = 15$.

4.2.7 Temporal spectra of near-wall signals

The averaged spectra of fluctuations of velocity components u', v', w', and pressure p' for points outside and inside each groove at the same groove phase location are plotted in figure 4.15. In each case, $N = 21$ grooves were selected. At each groove phase, the time history of velocity and pressure at two locations, one above the groove center at $y^+ = 5$, the other at the center of the groove at $y^+ = -1.8$ at $(z/(w+d) \bmod 1) = 0.5$ were stored over 72 000 time steps. The record was divided into 23 segments with 50% overlapping and averaged over each segment.

The power spectrum at the same wall-normal location is averaged as:

$$\Phi(\omega)|_y = \frac{1}{N}\sum_{j=1}^{N} \Phi^j(\omega)|_y, \tag{4.10}$$

where $\Phi^j(\omega)|_y$ is the power spectrum of each point with the same wall-normal coordinate. The transfer function is defined as the ratio of the spectrum inside the groove to the spectrum of the outside flow, considering the external flow as an energy input to the internal flow of the grooves:

$$\mathcal{H}(\omega) = \sqrt{\frac{\Phi_{uu}(\omega)|_{y^+=-1.8}}{\Phi_{uu}(\omega)_{y^+=5}}}. \tag{4.11}$$

The symbols in figure 4.15 represent the transfer function for a flat wall:

$$\mathcal{H}(\omega) = \sqrt{\frac{\Phi_{uu}|_{y^+=1.8}}{\Phi_{uu}|_{y^+=8.6}}}. \tag{4.12}$$

The location of $y^+ = 1.8$ was chosen such that its vertical distance to the bottom wall is the same as the point $y^+ = -1.8$ for the grooved cases. The distance between $y^+ = 8.6$ and $y^+ = 1.8$ is the same as the distance taken from inside the groove ($y^+ = -1.8$) to outside the groove ($y^+ = 5$). By comparing to the flat-wall channel data in figure 4.15, it is seen that the grooves suppress most of the low frequency ($\omega^+ 0.2$) energy of u' and w'. The grooves filter out the transverse fluctuation energy across all frequency

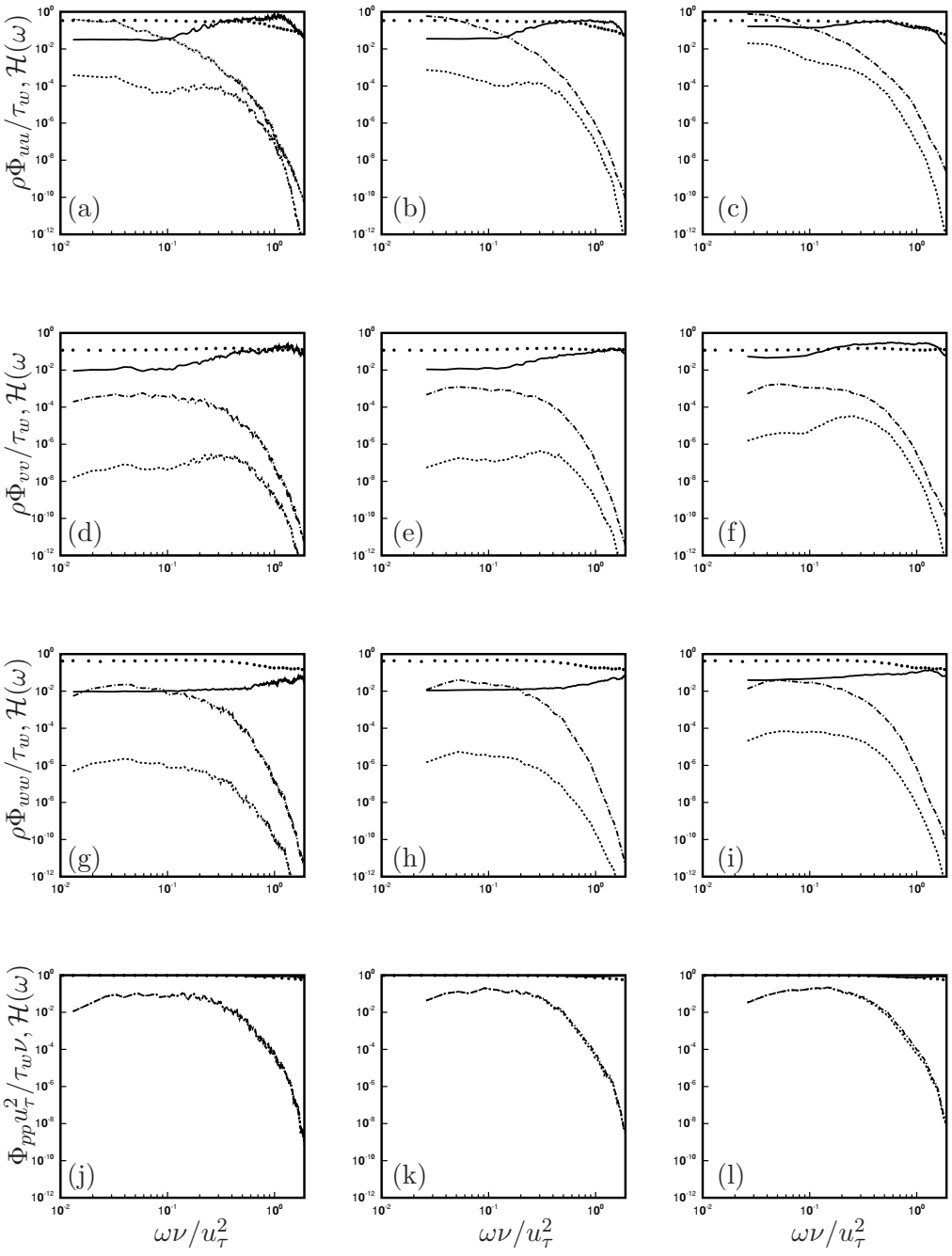

Figure 4.15: Averaged spectra of u', v', w' and p' fluctuations for the points at $y^+ = 5$ outside the groove (dashed-dotted line), and $y^+ = -1.8$ inside the grooves (dashed line) at the same groove phase location, and the transfer function $\mathcal{H}(\omega)$ of each pair of points (solid line) for C1 (first column), C320 (second column) and C160 (third column). Symbols stand for the transfer function of the corresponding spectra at $y^+ = 1.8$ to the spectra at $y^+ = 8.6$ in the flat-wall channel flow.

range. This agrees with [77] and [70] in their study of riblets that the riblets have a greater resistance to cross flow than parallel flow. But these two components have a lower energy overall than the streamwise component. There is no significant change in the pressure spectra.

4.3 Unsteady Stokes flow approximation

The DNS results in the previous sections suggest that the flow near the grooved surfaces is dominated by viscous effects and may therefore be approximated by the unsteady Stokes equation. Luchini et al. [77] made a similar approximation. They further argued that the Stokes equations for unsteady flow can be simplified to the steady Stokes equations since the inertia term and the convective term is of the same order and therefore can be neglected as well. But from the current DNS, the spectra of the transfer function inside the grooved surfaces show that the response is different at different frequencies. In this section, we study the effect of unsteadiness on the response of grooved surfaces by a set of numerical experiments. The unsteady component of the flow is modeled as an oscillating velocity of varying frequency and spanwise wavenumber. The numerical solutions are verified for the case of zero spatial wavenumber with analytical solutions derived in chapter 5. Instantaneous velocity and pressure fields are examined. The effect of the wavelength, frequency, and the location of the outside flow is studied.

4.3.1 Numerical details

We consider the unsteady Stokes flow bounded between an oscillating plane and a spanwise-periodic grooved wall (figure 4.16). The following scales are used for non-dimensionalization: the amplitude of the velocity of the top plane U_0 as the characteristic velocity; the half of the the groove span L as characteristic length; $1/\omega$ as

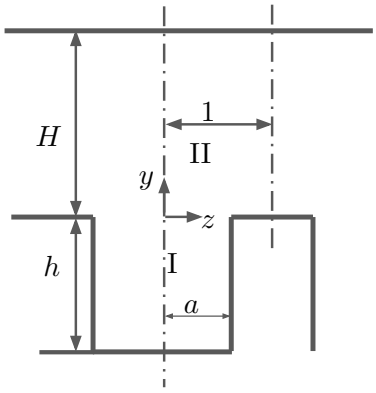

Figure 4.16: Schematic of the model problem and its geometric parameters.

characteristic time. The non-dimensional governing equations are:

$$\frac{\partial u_i}{\partial t} = -\frac{\partial p}{\partial x_i} + \frac{\nu}{L^2\omega}\frac{\partial^2 u_i}{\partial x_j \partial x_j}, \tag{4.13}$$

$$\frac{\partial u_i}{\partial x_i} = 0, \tag{4.14}$$

where the non-dimensional number $L^2\omega/\nu$ is the Womersley number. After expressing the variables as $f = \Re(\tilde{f}\exp(it))$, the equations become:

$$\mathrm{i}\tilde{u} = \frac{\nu}{L^2\omega}\nabla_*^2\tilde{u}, \tag{4.15}$$

$$\mathrm{i}\tilde{v} = -\frac{\partial \tilde{p}}{\partial y} + \frac{\nu}{L^2\omega}\nabla_*^2\tilde{v}, \tag{4.16}$$

$$\mathrm{i}\tilde{w} = -\frac{\partial \tilde{p}}{\partial z} + \frac{\nu}{L^2\omega}\nabla_*^2\tilde{w}, \tag{4.17}$$

$$0 = \nabla_*^2\tilde{p}, \tag{4.18}$$

where ∇_* is the gradient operator in $y-z$ plane. The pressure gradient in x-direction is 0 due to periodicity. Equation (4.15) is independent from equations (4.16)-(4.18). The

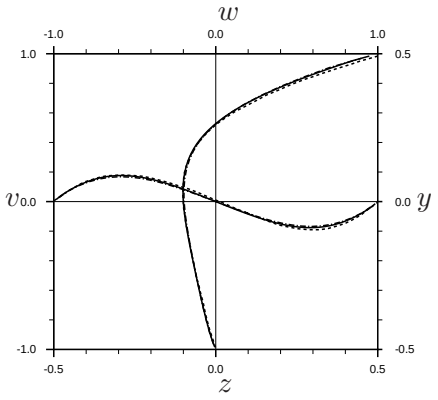

Figure 4.17: Lid driven cavity validation. Dashed line, [122], $Re = 10$; dashed-dotted line, 32×32; solid line, 64×64.

velocities are subject to the no-slip boundary condition at the walls:

$$u = v = w = 0,$$

and the boundary condition at the top:

$$\mathrm{BC}_i = u_j = \cos(k_z \pi / Lz + t)\delta_{ij},\ j = 1,\ 2,\ 3,$$

where BC_i is the boundary condition specified for each case, k_z is the wavenumber of the perturbation. We introduce the vorticity, $\tilde{\omega}_x = \frac{\partial \tilde{w}}{\partial y} - \frac{\partial \tilde{v}}{\partial z}$ and streamfunction ($\tilde{\Psi}$) to replace $\tilde{w}$ ($= \frac{\partial \tilde{\Psi}}{\partial y}$) and $\tilde{v}$ ($= -\frac{\partial \tilde{\Psi}}{\partial z}$) in equations (4.15)-(4.18), and solve for the streamfunction-vorticity using a finite-volume method. After obtaining $\tilde{\omega}_x$ and $\tilde{\Psi}$, $\tilde{p}$, $\tilde{u}$, $\tilde{v}$, and $\tilde{w}$ are computed. Note that to ensure continuity in the plane, the vertical velocity boundary condition always has a wavelength in span.

4.3.2 Validation

The canonical lid-driven cavity flow serves as a benchmark case and a test of grid convergence. The results are compared to [122] in figure 4.17. Both 32×32 and 64×64 resolutions agree well with the benchmark data. In the following cases, a uniform grid of 32×32 is used to resolve the groove and the same spacing is used for the outside

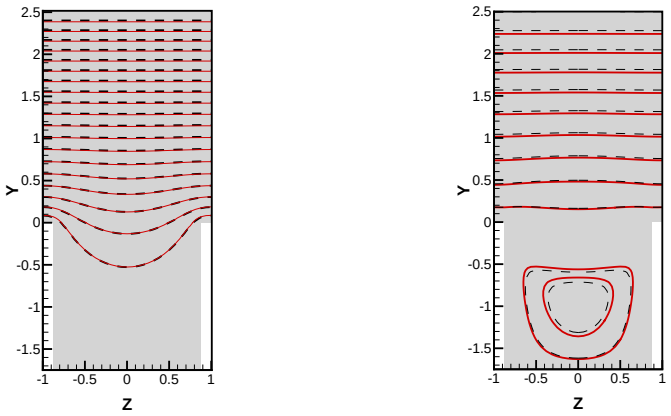

(a) BC_1, contour of u (b) BC_3, contour of w

Figure 4.18: Comparison of the contours of the solution calculated analytically (§5, red solid lines) and numerically (dashed lines). (a) The levels of u are from 0 to 1 from bottom to top with an increment of 0.1. (b) The levels of w are from 0.1 to 1 from bottom to top with an increment of 0.1 outside the groove. The two levels inside the groove are -0.005 and -0.002 from interior to exterior. $H = 2.5$, $a = 0.875$, $h = 1.75$, $L^2\omega/\nu = 0.423$.

region.

The solution to streamwise/spanwise velocities that are constant in z can be obtained analytically (derivation is presented in chapter 5). This problem is reminiscent of the Stokes second problem [80] or spatially oscillating forcing [82]. Figure 4.18 shows that for both streamwise and spanwise flow, the agreement between the numerical simulation and the analytical solution is good. More details of the analytical solution can be found in chapter 5.

Next, the perturbation is decomposed into three directions and the problem is solved separately. All the following cases are based on the probing locations of C320 (input location is at $H = 2.5$, output location is at $-b/2$). For each perturbation direction, a broad range of wavenumbers and frequencies is explored numerically.

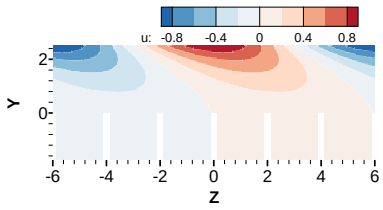

Figure 4.19: Instantaneous contours of u generated by a streamwise velocity BC_1: $u = \cos(k_z \pi z/L + t)$. $k_z = 1/6$, $L^2\omega/\nu = 1.45$.

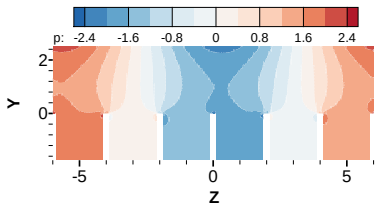

(a) p

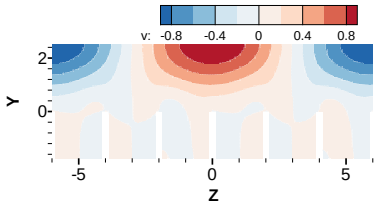

(b) v

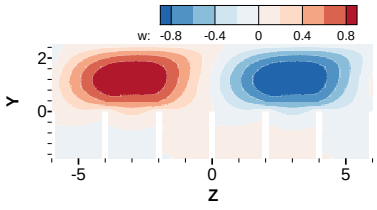

(c) w

Figure 4.20: Instantaneous contours of (a) p; (b) v; (c) w generated by a vertical velocity BC_2: $v = \cos(k_z \pi z/L + t)$. $k_z = 1/6$, $L^2\omega/\nu = 1.45$.

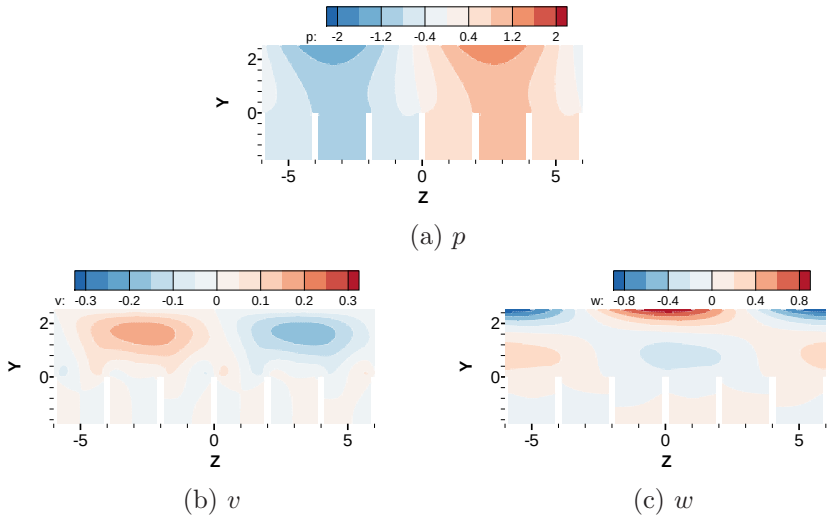

(a) p

(b) v

(c) w

Figure 4.21: Instantaneous contours of (a) p; (b) v; (c) w generated by a spanwise velocity BC_3: $w = \cos(k_z \pi z/L + t)$. $k_z = 1/6$, $L^2\omega/\nu = 1.45$.

Instantaneous solution

Figures 4.19-4.21 show instantaneous contour plots of the velocity and pressure fields due to an oscillating velocity boundary conditions in different directions. For longitudinal grooves, when the perturbation is in the streamwise direction (figure 4.19), it only induces streamwise velocity due to diffusion. Perturbations in the vertical direction (figure 4.20) travel in both spanwise and vertical directions, causing the velocity components in these two directions to oscillate simultaneously. A reverse flow in spanwise direction is formed inside the grooves. Similar behavior is observed in the spanwise perturbed flow (figure 4.21), however, the range of v velocity in figures 4.20(b) and 4.21(b) suggests that the energy does not propagate as much as that in vertical perturbed flow indicating that the grooved surfaces provides a shielding effect to transverse flow.

Effect of frequency and wavelength of the outside flow

Figure 4.22 shows the transfer functions generated by oscillating velocities in different directions. For BC_2 and BC_3, although the boundary condition is applied in either vertical or spanwise direction, as is observed from the instantaneous plots, v and w

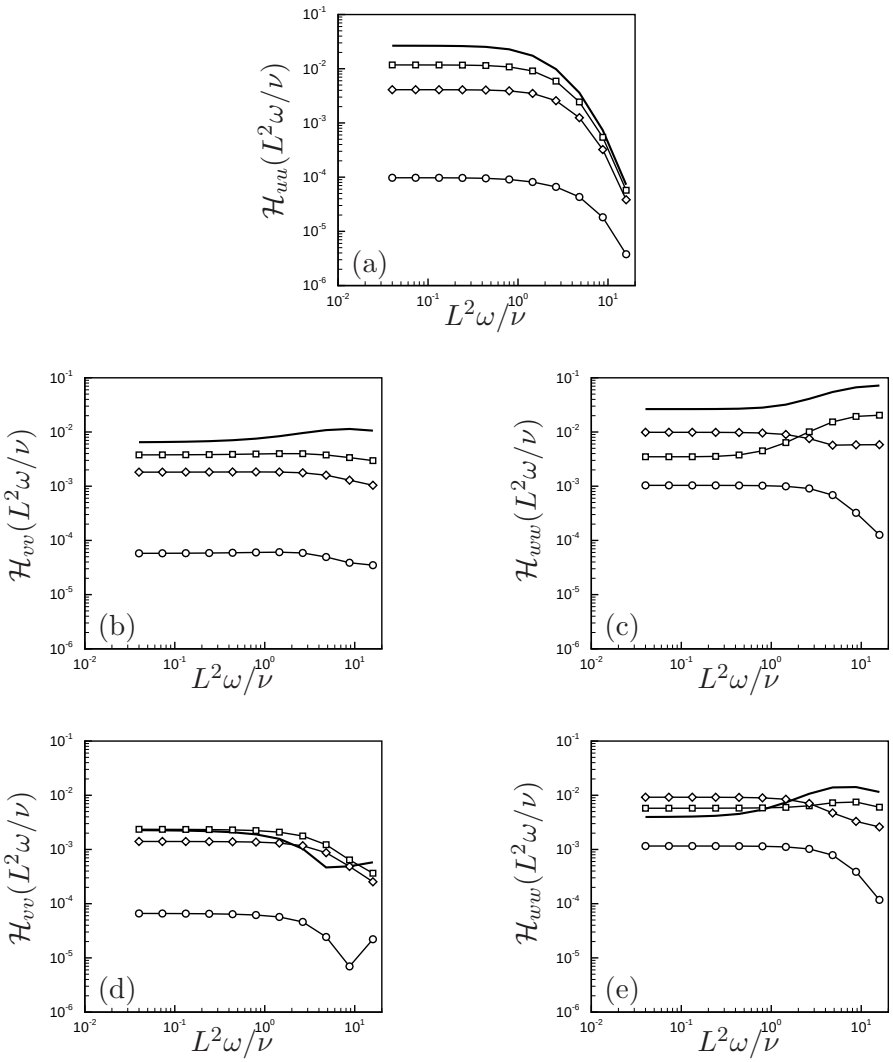

Figure 4.22: Transfer function $\mathcal{H}$ produced by perturbation in (a) BC_1; (b, c) BC_2; (d, e) BC_3. Solid line, $k_z = 1/6$; $\square$, $k_z = 1/3$; $\Diamond$, $k_z = 1/2$; $\bigcirc$, $k_z = 1$.

velocities induce each other by pressure gradient. Therefore, the definition of the transfer function is changed to:

$$\mathcal{H}(L^2\omega/\nu) = \sqrt{\frac{\Phi_{u_i u_i}(L^2\omega/\nu)}{\Phi_k(L^2\omega/\nu)}}, \tag{4.19}$$

to avoid singularity, the input energy is defined as the kinetic energy k at the oscillating boundary. The transfer function due to streamwise perturbation decreases monotonically with increasing k_z. As is supported by the instantaneous plots, v velocity causes the most response, whereas, the response to transverse flow is weak. This behavior agrees with the finding of Choi et al. [70] that such surfaces impede cross-flow motion. The trend of $\mathcal{H}_{ww}$ generally decreases with increasing frequency except a rise beyond $L^2\omega/\nu = 1$ for both v and w induced motion at $k_z = 1/6$ and $k_z = 1/3$. Overall, kinetic energy at long wavelengths penetrates more than short wavelengths. Observed from the previous section, the intensity of $\overline{v'v'}$ only takes up 1% of the turbulent kinetic energy at the probed location, so the response of the grooved surfaces to vertical perturbation is not discussed any further.

The instantaneous slip length $b = u_i/(\partial u_i/\partial y)$, where i indicates either spanwise or streamwise direction, varies along the span (figure 4.23). Cases that are induced by vertical velocity are not considered. At this instant, the distribution of both $b_\parallel$ and $b_\perp$ are similar with $b_\parallel$ larger than $b_\perp$ in general. Singularities occur where both velocity and its gradient are zero. The distribution of the streamwise slip length becomes asymmetric about the peak location of the boundary condition as frequency increases. This is because the boundary condition is traveling to the right at a speed of $\omega L/(k_z\pi)$; as the frequency increases the convection velocity increases. Since the groove shape is not in phase with the cosine wave of the outside flow, the distribution of the slip length becomes asymmetric within each groove. As the frequency increases, the slip length decreases except at singular points. Instantaneously, each groove experiences a different part of the perturbation wave, therefore showing a different distribution across each groove span.

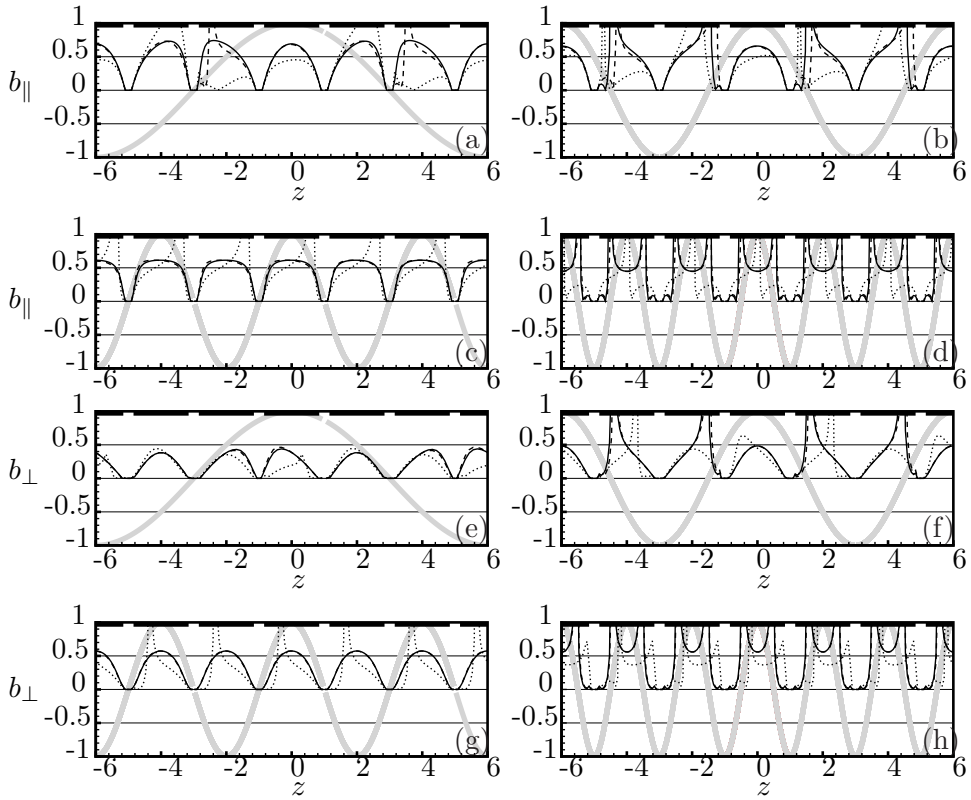

Figure 4.23: (a-d) Instantaneous distribution of $b_\parallel$ induced by streamwise velocity BC_1 along the grooved span at $y = 0$. (e-h) Distribution of $b_\perp$ induced by spanwise velocity BC_3 along the grooved span at $y = 0$. (a, e) $k_z = 1/6$, (b, f) $k_z = 1/3$, (c, g) $k_z = 1/2$, (d, h) $k_z = 1$. The light grey curve indicates the slip velocity boundary condition. Black curves represent the distribution of different Womersley number: solid line ($L^2\omega/\nu = 0.01$); dashed line ($L^2\omega/\nu = 0.06$); dotted line ($L^2\omega/\nu = 1.20$). The short bars on the top axis show the location of the grooves.

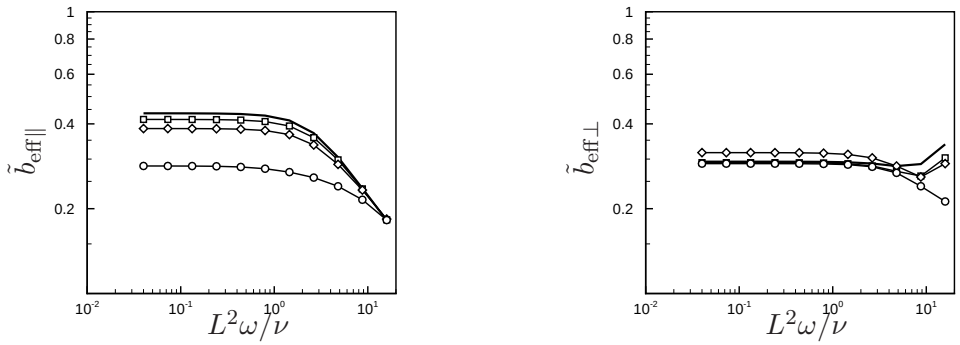

(a) Streamwise velocity BC_1 (b) Spanwise velocity BC_3

Figure 4.24: $\tilde{b}_{\text{eff}}$ produced by boundary conditions with wavenumbers: solid line, $k_z = 1/6$; $\square$, $k_z = 1/3$; $\Diamond$, $k_z = 1/2$; $\bigcirc$, $k_z = 1$.

The effective slip length is defined as:

$$\tilde{b}_{\text{eff}\parallel} = \frac{k_z}{2}\int_{-1/k_z}^{1/k_z} \frac{\tilde{u}(0,z)}{\partial\tilde{u}/\partial y(0,z)}\mathrm{d}z, \tag{4.20}$$

$$\tilde{b}_{\text{eff}\perp} = \frac{k_z}{2}\int_{-1/k_z}^{1/k_z} \frac{\tilde{w}(0,z)}{\partial\tilde{w}/\partial y(0,z)}\mathrm{d}z. \tag{4.21}$$

Figure 4.24 shows the effective slip length at each frequency for different wavenumbers. $\tilde{b}_{\text{eff}\parallel}$ has a similar trend as $\mathcal{H}_{uu}$. $\tilde{b}_{\text{eff}\perp}$ increases at high frequency because the velocity gradient approaches zero. Overall, for both directions, $\tilde{b}_{\text{eff}}$ remains between 0.1 and 1 within the frequency range of interest and does not vary much by wavelength. At low frequency, the effective slip lengths in both directions are close.

Effect of the input location

The effect of the input location H is examined by varying H and computing the corresponding transfer function $\mathcal{H}$ in figure 4.25. For streamwise flow, in figure 4.25(a), $\mathcal{H}$ decreases monotonically with increasing input height; for spanwise flow, the trend is generally the same except the rise at high frequency for $H = 2.5$.

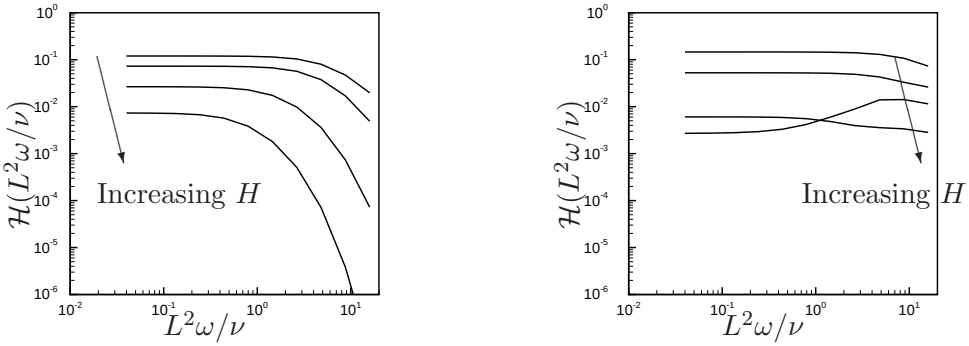

(a) Streamwise velocity BC_1 (b) Spanwise velocity BC_3

Figure 4.25: Raising the input location H decreases the spectra inside the groove. The arrows indicate the direction of increasing $H \in 0.5, 1, 2.5, 5$. $k_z = 1/6$.

4.3.3 Relationship to turbulent flow

The dimensionless parameter governing the unsteady Stokes flow considered is $\omega L^2/\nu$. In a turbulent flow, it is related Re_τ as $\frac{\omega L^2}{\nu} = \omega^+ Re_\tau^2 \left(\frac{L}{\delta}\right)^2$. Figure 4.26 shows the transfer function predicted by the model at $H = 2.5$, $k_z = 0$ compared to DNS. The model solution shows a good agreement at low frequencies, but at high frequencies, it deviates from the DNS data and does not show the increasing trend within the frequency range $\omega^+ = 0.1 - 1.0$. According to figure 4.22(a), varying the wavelength in the span does not increase the transfer function significantly. There are two hypotheses for this behavior. One is that it could be the response of the grooved surfaces to perturbations with streamwise variation. Since the typical wavelength of the near-wall structure is $\lambda_x^+ = 1000$, that is $k_x = 0.01$ for the model problem, this is not considered in this chapter. The other is that in turbulent flow at high frequencies, structures of small wavelength near the grooved surfaces could excite the flow inside the grooves that would all contribute to the increase of the transfer function (figure 4.25). This mechanism is illustrated in the diagram in figure 4.27. For the Stokes flow problem considered in this section, only one wavelength at a fixed height is considered: the transfer function cannot therefore capture this effect. Varying H and k_z in figure 4.28 offers support for this conjecture. For streamwise spectra, two locations $H = 2.5$ (lower symbols) and

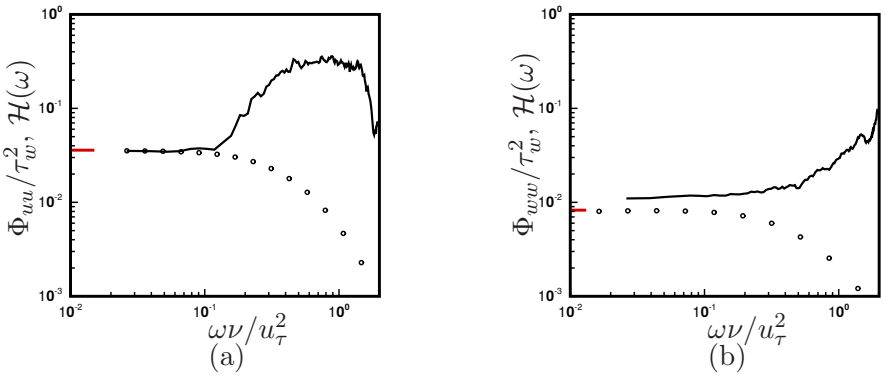

Figure 4.26: Transfer functions $\mathcal{H}(\omega)$ of (a) u, (b) w velocity fluctuations for the points at $y^+ = 5$ outside the groove and $y^+ = -1.8$ inside the groove in solid lines. The Stokes flow predictions of $\mathcal{H}(\omega)$ are in ◯ for C320. The short red lines at the y-axis indicate the analytical solutions of $\mathcal{H}(\omega)$ in steady flow.

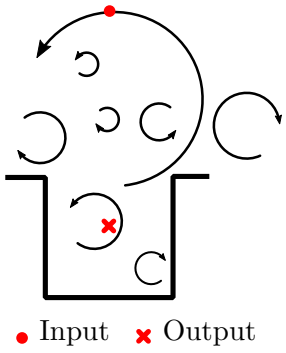

Figure 4.27: Schematic of transfer function increasing mechanism at high frequency.

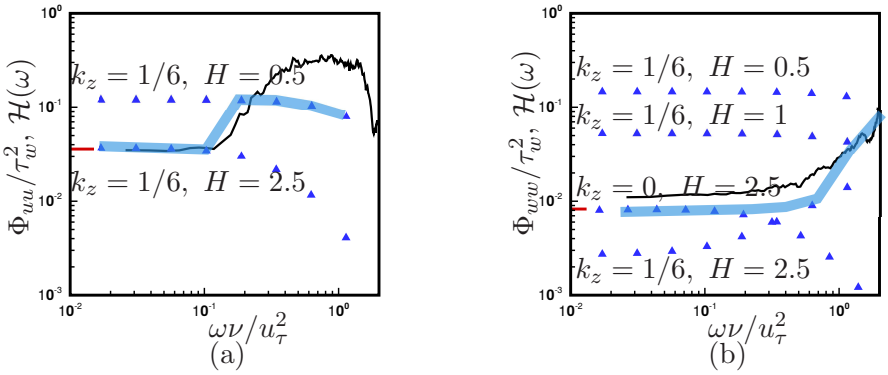

Figure 4.28: Transfer functions $\mathcal{H}(\omega)$ of (a) u, (b) w velocity fluctuations for the points at $y^+ = 5$ outside the groove and $y^+ = -1.8$ inside the groove in solid lines. The Stokes flow prediction of $\mathcal{H}(\omega)$ (▲) by (a) BC_1 streamwise velocity boundary condition and (b) BC_3 spanwise velocity boundary condition. The blue line highlights the combination of k_z and H that matches with DNS data the most. The short red line at the y-axis indicate the solutions of $\mathcal{H}(\omega)$ in the steady flow.

$H = 0.5$ (higher symbols) at $k_z = 1/6$ are plotted in figure 4.28(a), where the blue line resembles the DNS result the most. For spanwise spectra, the blue line corresponds to $k_z = 0$, $H = 2.5$ at low frequency, at high frequency the perturbation at $H = 1$ and $H = 0.5$ contribute the most. Note that the wavenumber $k_z = 1/6$ corresponds to $\lambda_z^+ \approx 25$, which is close to the typical diameter of the dynamically significantly streamwise vortices 30 in wall units as is assumed in [70].

4.4 Summary

We have performed DNS of turbulent channel flows with grooved surfaces on one wall. Differences in the mean profiles are found to be limited to the viscous sublayer of the boundary layer. Overall, all cases are hydrodynamically smooth. In C1, the grooves are isolated with a coverage ratio of $\phi = 0.27\%$, the surface has no overall effect. When the grooves have a coverage ratio of $\phi = 87.5\%$ in C320, the grooved surfaces act as one flat wall, the slip effect is only limited to the inner region of the boundary layer. For C160, the groove size is twice as large as the one in C320. The drag reduction increases to 0.53%. Spectral analysis of the results shows that the transfer function between the

signal in the outer flow and that inside the groove is suppressed within a frequency range of $\omega^+ < 0.2$. Similar behavior is found in v and w components.

In order to explain this phenomenon, we have proposed a model problem in which the external signal is Fourier decomposed, and the unsteady Stokes equations describe the flow near the grooves. The problem is parameterized by $\omega L^2/\nu$ and the unsteady Stokes equations are solved analytically and numerically. It is shown that at low frequency the solution with $k_z = 0$ predicts the suppression of energy by the grooves accurately. A series of numerical experiments of oscillating Stokes flow parameterized by the spanwise wavenumber k_z, location of the input H, and the non-dimensional number $\omega L^2/\nu$ were performed. According to the numerical experiments, the grooves impede the cross-flow motion, which is consistent with the drag reduction mechanism for riblets proposed by Choi et al. [70]. Furthermore, the response of the grooved surfaces to the forcing (representative of the external flow) depends on its wavenumber and location. It is hypothesized that small structures that are close to the grooves excite the internal flow at high frequencies, which makes the transfer function grow in that frequency range. By varying the wavenumber and location of the outside perturbation, we are able to recover the turbulent DNS behavior using the Stokes flow solution.

Chapter 5

Theoretical study of single-phase unsteady Stokes flow over grooved surfaces

The unsteady flow over grooved surfaces is simplified into an incompressible Stokes flow driven by a streamwise/spanwise velocity oscillating in time over longitudinal, spanwise-periodic grooves. This simplification is based on the observation from chapter 4 that $\overline{u'v'}$ is very low in the vicinity of the grooves in the turbulent flow. The solutions to streamwise or spanwise oscillating flows are derived in §5.1 and §5.2, respectively. In §5.3, DNS is performed to validate the solution.

5.1 Oscillating streamwise unsteady Stokes flow

We consider the incompressible and viscous flow over an array of grooves driven by an oscillating velocity. A schematic of the model is shown in figure 5.1. We introduce the

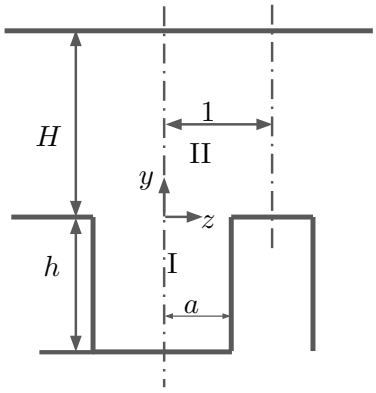

Figure 5.1: Schematic of the model problem and its geometric parameters.

non-dimensional variables as:

$$u = u^*/U_0, \tag{5.1}$$

$$y = y^*/L, \tag{5.2}$$

$$t = t^*\omega, \tag{5.3}$$

where the variables with the asterisks represent dimensional variables, U_0 is the velocity magnitude U_0, L is the half period of the groove, and *omega* is the frequency of the oscillating velocity. The groove geometry at the lower wall, $y = 0$ is defined by its depth b and half-groove width a. The oscillating velocity $u(H, z, t) = \cos(t)$. The groove is periodic in the span and symmetric at the center. The dimensionless governing equation is

$$\frac{\partial u}{\partial t} = \frac{\nu}{L^2\omega}(\frac{\partial^2 u}{\partial z^2} + \frac{\partial^2 u}{\partial y^2}). \tag{5.4}$$

where u is the streamwise velocity, ν is the viscosity, and the non-dimensional number $L^2\omega/\nu$ is the Womersley number. For an oscillatory flow, we assume the solution is of the form:

$$u(y, z, t) = \Re(\tilde{u}(y, z)\exp(it)) = \Re(Y(y)Z(z)\exp(it)). \tag{5.5}$$

Substituting (5.5) into (5.4), we obtain

$$i\tilde{u} = \frac{\nu}{L^2\omega}\left(\frac{\partial^2\tilde{u}}{\partial y^2} + \frac{\partial^2\tilde{u}}{\partial z^2}\right). \tag{5.6}$$

Let $\tilde{u}(y,z) = Y(y)Z(z)$, then

$$\frac{Y''}{Y} + \frac{Z''}{Z} = \frac{iL^2\omega}{\nu}.$$

The domain of interest is divided into two rectangular regions. Region I represents the fluid inside the grooves and region II represents the fluid from $y = 0$ to the oscillating boundary at $y = H$. The strategy is to solve for the general solutions, which are series of eigensolutions, in the two regions independently and determine the constant coefficients by matching the boundary conditions between the neighboring regions. The separable solutions are independent of time, therefore could be written in dimensionless form as:

$$\tilde{u}_{\mathrm{II}} = \begin{cases} \tilde{u}_{\mathrm{I}}, & 0 \leqslant z < a, \\ 0, & a < z \leqslant 1; \end{cases} \tag{5.7}$$

$$\frac{\partial\tilde{u}_{\mathrm{I}}(0,z)}{\partial y} = \frac{\partial\tilde{u}_{\mathrm{II}}(0,z)}{\partial y}. \tag{5.8}$$

5.1.1 Region I

In region I the boundary conditions are no-slip at the walls ($z = a$ and $y = -b$), symmetric at the groove center ($z = 0$), and the common boundary between I and II, which is retained for determining the constants in proceeding procedures. The boundary conditions are expressed in terms of $\tilde{u}(y,z) = Y(y)Z(z)$ as:

$$\frac{\partial\tilde{u}_{\mathrm{I}}(y,0)}{\partial z} = 0 \Rightarrow Z'(0) = 0, \tag{5.9}$$

$$\tilde{u}_{\mathrm{I}}(y,a) = 0 \Rightarrow Z(a) = 0, \tag{5.10}$$

$$\tilde{u}_{\mathrm{I}}(-b,z) = 0 \Rightarrow Y(-b) = 0. \tag{5.11}$$

From (5.9) and (5.10), we get:

$$Z_n(z) = \cos(\alpha_n z).$$

where $\alpha_n = (n - \frac{1}{2})\frac{\pi}{a}$. Then there must be $\frac{Y''}{Y} = \frac{iL^2\omega}{\nu} + \alpha_n^2$.

Similarly, the general solution for $Y(y)$ has the eigenfunction:

$$Y_n(y) = \exp\left[\sqrt{\alpha_n^2 + \frac{iL^2\omega}{\nu}}y\right] - \exp\left[-\sqrt{\alpha_n^2 + \frac{iL^2\omega}{\nu}}(y + 2b)\right].$$

So a separable solution for $\tilde{u}_{\mathrm{I}}(y, z)$ is:

$$\tilde{u}_{\mathrm{I}}(y, z) = \sum_{n=1}^{\infty} A_n \cos(\alpha_n z)\left\{\exp\left[\sqrt{\alpha_n^2 + \frac{iL^2\omega}{\nu}}y\right] - \exp\left[-\sqrt{\alpha_n^2 + \frac{iL^2\omega}{\nu}}(y + 2b)\right]\right\}. \tag{5.12}$$

5.1.2 Region II

The boundary conditions of region II are symmetric at the center ($z = 0$) and between grooves ($z = 1$). At the fixed height $y = H$, the velocity is oscillating with time.

$$\frac{\partial \tilde{u}_{\mathrm{II}}(y, 0)}{\partial z} = 0 \Rightarrow Z'(0) = 0 \tag{5.13}$$

$$\frac{\partial \tilde{u}_{\mathrm{II}}(y, 1)}{\partial z} = 0 \Rightarrow Z'(1) = 0 \tag{5.14}$$

$$\tilde{u}_{\mathrm{II}}(H, z) = 1 \tag{5.15}$$

The solution for Z must satisfy equation (5.13) and (5.14), e.g.:

$$Z_n(z) = \cos(n\pi z),$$

Hence the solutions for $Y(y)$ must satisfy

$$\frac{Y''}{Y} = \frac{iL^2\omega}{\nu} + (n\pi)^2 \tag{5.16}$$

for any integer n. Therefore the solutions for $Y(y)$ is:

$$Y_n(y) = B_n \exp\left(\sqrt{(n\pi)^2 + \frac{iL^2\omega}{\nu}}y\right) + C_n \exp\left(-\sqrt{(n\pi)^2 + \frac{iL^2\omega}{\nu}}y\right). \tag{5.17}$$

Let $R = \sqrt{(n\pi)^4 + (\frac{L^2\omega}{\nu})^2}$, $\theta = \arctan\left[\frac{L^2\omega}{\nu(n\pi)^2}\right]$, then

$$Y_n(y) = B_n \exp\left[\sqrt{R}\left(\cos\frac{\theta}{2} + i\sin\frac{\theta}{2}\right)y\right] \tag{5.18}$$

$$+C_n \exp\left[-\sqrt{R}\left(\cos\frac{\theta}{2} + i\sin\frac{\theta}{2}\right)y\right]. \tag{5.19}$$

So the general solution in region II is:

$$\begin{aligned}\tilde{u}_{\mathrm{II}}(y,z) = {} & B_0 \exp\left[\sqrt{\frac{L^2\omega}{2\nu}}(1+i)\,y\right] + C_0 \exp\left[-\sqrt{\frac{L^2\omega}{2\nu}}(1+i)\,y\right] \\ & + \sum_{n=1}^{\infty}\cos(n\pi z)\left\{B_n \exp\left[\sqrt{R}\left(\cos\frac{\theta}{2} + i\sin\frac{\theta}{2}\right)y\right] + \right. \\ & \left. C_n \exp\left[-\sqrt{R}\left(\cos\frac{\theta}{2} + i\sin\frac{\theta}{2}\right)y\right]\right\}.\end{aligned} \tag{5.20}$$

The non-homogeneous behavior of the flow in spanwise direction is caused by the groove, which is reflected in the form of $\cos(n\pi z)$. It should diminish as the distance to the groove increases, therefore the coefficients $B_n = 0$. Furthermore, the boundary condition (5.15) gives

$$\begin{aligned}& B_0 \exp\left[\sqrt{\frac{L^2\omega}{2\nu}}(1+i)\,H\right] + C_0 \exp\left[-\sqrt{\frac{L^2\omega}{2\nu}}(1+i)\,H\right] \\ & - \sum_{n=1}^{\infty}\cos(n\pi z) C_n \exp\left[-\sqrt{R}\left(\cos\frac{\theta}{2} + i\sin\frac{\theta}{2}\right)H\right] = 1.\end{aligned} \tag{5.21}$$

Integrating (5.21) from 0 to 1 gives

$$B_0 \exp\left[\sqrt{\frac{L^2\omega}{2\nu}}\,(1+i)\,H\right] + C_0 \exp\left[-\sqrt{\frac{L^2\omega}{2\nu}}\,(1+i)\,H\right] = 1. \tag{5.22}$$

$$B_0 = \exp\left[-\sqrt{\frac{L^2\omega}{2\nu}}\,(1+i)\,H\right] - C_0 \exp\left[-2\sqrt{\frac{L^2\omega}{2\nu}}\,(1+i)\,H\right]. \tag{5.23}$$

5.1.3 Between Region I and Region II

Next, we determine the unknown constants C_0, C_n and A_n by applying the boundary condition between the two regions defined by (5.7) and (5.8). Integrating (5.7) from 0 to 1:

$$B_0 + C_0 = \sum_{n=1}^{\infty} -A_n \frac{(-1)^n}{\alpha_n}\left[1 - \exp\left(-2b\sqrt{\alpha_n^2 + \frac{iL^2\omega}{\nu}}\right)\right]. \tag{5.24}$$

Multiplying (5.7) by $\cos(m\pi z)$ then integrating from 0 to 1:

$$C_m = 2\sum_{n=1}^{\infty} A_n L_{mn}\left[1 - \exp\left(-2b\sqrt{\alpha_n^2 + \frac{iL^2\omega}{\nu}}\right)\right], \tag{5.25}$$

where

$$L_{mn} = \frac{\sin[\pi(ma+n-0.5)]}{2\pi[m+(n-0.5)/a]} + \frac{\sin[\pi(ma-n+0.5)]}{2\pi[m-(n-0.5)/a]}. \tag{5.26}$$

Multiplying (5.8) by $\cos(\alpha_m z)$ then integrating from 0 to a:

$$-\sqrt{\frac{iL^2\omega}{\nu}}\frac{(-1)^m}{\alpha_m}(B_0 - C_0) - \sum_{n=1}^{\infty} C_n L_{nm}\left(\sqrt{R}\cos\frac{\theta}{2} + i\sqrt{R}\sin\frac{\theta}{2}\right) = \frac{a}{2}A_m\sqrt{\alpha_m^2 + \frac{iL^2\omega}{\nu}}\left[1 + \exp\left(-2b\sqrt{\alpha_m^2 + \frac{iL^2\omega}{\nu}}\right)\right]. \tag{5.27}$$

Finally, C_m is truncated to M terms and A_n is truncated to $N = \mathrm{Int}[aM]$ terms. By solving equations (5.25) and (5.27) as a system of equations, we get all the unknown coefficients in the solution. A set of validation cases are given in §5.3.

The energy spectra is

$$\Phi(\omega) = \tilde{u}\tilde{u}^*. \tag{5.28}$$

The transfer function is given by

$$H(\omega) = \sqrt{\frac{\Phi(\omega)_{\text{output}}}{\Phi(\omega)_{\text{input}}}} = \tilde{u}_{\text{I}}\tilde{u}_{\text{I}}^*, \tag{5.29}$$

where $\tilde{u_{\text{I}}}$ is the Fourier transform of the solution in region I given in equation (5.12). Therefore the analytical solution can predict the transfer function of any signal inside the groove versus the a signal in the outside flow.

5.2 Oscillating spanwise unsteady Stokes flow

The procedure to solve for the oscillating spanwise unsteady Stokes flow is similar to the streamwise problem. The non-dimensional governing equation becomes:

$$\nabla^4\tilde{\Psi} = \frac{iL^2\omega}{\nu}\nabla^2\tilde{\Psi}, \tag{5.30}$$

where $(\Psi_y, -\Psi_z) = (w, v)$ and is normalized by U_0/L, and $\Psi = \Re(\tilde{\Psi})$. The boundary conditions are no-slip and $\partial\tilde{\Psi}/\partial n$ is zero at the walls. At $y = H$, $\tilde{\Psi}_y = 1$. At $y = 0$, the conditions are matched by:

$$\tilde{\Psi}_{\text{II}} = \begin{cases} \tilde{\Psi}_{\text{I}}, & 0 \leqslant z < a, \\ 0, & a < z \leqslant 1; \end{cases} \tag{5.31}$$

$$\tilde{\Psi}_{\text{II}y} = \begin{cases} \tilde{\Psi}_{\text{I}y}, & 0 \leqslant z < a, \\ 0, & a < z \leqslant 1; \end{cases} \tag{5.32}$$

$$\tilde{\Psi}_{\text{I}yy} = \tilde{\Psi}_{\text{II}yy}, \quad 0 \leqslant z < a, \tag{5.33}$$

$$\tilde{\Psi}_{\text{I}yyy} = \tilde{\Psi}_{\text{II}yyy}, \quad 0 \leqslant z < a. \tag{5.34}$$

5.2.1 Region I

$\hat{\Psi}$ and its normal derivatives are zero at the walls and symmetric at the groove center ($z = 0$). The common boundaries between region I and II, and between region I and III, are retained for determining the constants in the proceeding procedures. A separable solution for $\hat{\Psi}_{\mathrm{I}}$ is:

$$\hat{\Psi}_I(y,z) = \sum_{n=1}^{\infty} \cos(\alpha_n z) f_n(y) + \sum_{n=1}^{\infty} C_n \sin(\beta_n y)\phi_n(\beta_n; z), \tag{5.35}$$

where $\beta_n = n\pi/b$, and

$$\begin{aligned} f_n(y) = {} & A_{1n} \exp\left(\sqrt{\alpha_n^2 + \frac{iL^2\omega}{\nu}}\, y\right) + A_{2n} \exp\left[-\sqrt{\alpha_n^2 + \frac{iL^2\omega}{\nu}}\,(y+2b)\right] \\ & + A_{3n}\exp(\alpha_n y) + A_{4n}\exp[-\alpha_n(y+2b)], \end{aligned} \tag{5.36}$$

$$\begin{aligned} \phi_n(\beta_n; z) = {} & \exp\left(\sqrt{\beta_n^2 + \frac{iL^2\omega}{\nu}}\,(z-a)\right) + \exp\left(-\sqrt{\beta_n^2 + \frac{iL^2\omega}{\nu}}\,(z+a)\right) \\ & - \frac{1 + \exp\left(-2\sqrt{\beta_n^2 + \frac{iL^2\omega}{\nu}}\, a\right)}{1 + \exp\left(-2\beta_n a\right)} \left[\exp\left(\beta_n(z-a)\right) + \exp\left(-\beta_n(z+a)\right)\right]. \end{aligned} \tag{5.37}$$

At the side wall

$$\tilde{\Psi}_{Iz}(y,a) = 0. \tag{5.38}$$

Multiplying this by $\sin(\beta_m y)$ and integrating from $-b$ to 0 yields:

$$\sum_{n=1}^{\infty} \alpha_n (-1)^n (A_{1n}K_{1mn} + A_{2n}K_{2mn} + A_{3n}K_{3mn} + A_{4n}K_{4mn}) + \frac{b}{2} C_m \phi_m'(a) = 0, \tag{5.39}$$

where

$$K_{1mn} = \frac{\beta_m \left[\exp\left(-\sqrt{\alpha_n^2 + \frac{iL^2\omega}{\nu}}b\right)(-1)^m - 1\right]}{\alpha_n^2 + \beta_m^2 + \frac{iL^2\omega}{\nu}},$$

$$K_{2mn} = \frac{\beta_m \left[\exp\left(\sqrt{\alpha_n^2 + \frac{iL^2\omega}{\nu}}b\right)(-1)^m - 1\right]\exp\left(-2\sqrt{\alpha_n^2 + \frac{iL^2\omega}{\nu}}b\right)}{\alpha_n^2 + \beta_m^2 + \frac{iL^2\omega}{\nu}},$$

$$K_{3mn} = \frac{\beta_m \left[\exp\left(-\alpha_n b\right)(-1)^m - 1\right]}{\alpha_n^2 + \beta_m^2},$$

$$K_{4mn} = \frac{\beta_m \left[\exp\left(\alpha_n b\right)(-1)^m - 1\right]\exp\left(-2\alpha_n b\right)}{\alpha_n^2 + \beta_m^2}.$$

$\hat{\Psi}_I$ satisfies:

$$\hat{\Psi}_{\mathrm{I}}(-b, z) = 0, \tag{5.40}$$

$$\hat{\Psi}_{\mathrm{I}y}(-b, z) = 0, \tag{5.41}$$

at the bottom wall. Equation (5.40) yields:

$$\exp\left(-\sqrt{\alpha_n^2 + \frac{iL^2\omega}{\nu}}b\right)(A_{1n} + A_{2n}) + \exp(-\alpha_n b)(A_{3n} + A_{4n}) = 0. \tag{5.42}$$

Multiplying equation (5.41) by $\cos(\alpha_m z)$ and integrating from 0 to a:

$$\frac{a}{2}\left[\sqrt{\alpha_m^2 + \frac{iL^2\omega}{\nu}}\exp\left(-\sqrt{\alpha_m^2 + \frac{iL^2\omega}{\nu}}b\right)(A_{1m} - A_{2m}) + \alpha_m \exp\left(-\alpha_m b\right)(A_{3m} - A_{4m})\right] + \sum_{n=1}^{\infty} C_n \beta_n (-1)^n H_{mn} = 0, \tag{5.43}$$

where

$$H_{mn} = \frac{\frac{iL^2\omega}{\nu}\alpha_m(-1)^m\left[\exp\left(-2\sqrt{\beta_n^2 + \frac{iL^2\omega}{\nu}}a\right)\right]}{(\alpha_m^2 + \beta_n^2)(\alpha_m^2 + \beta_n^2 + \frac{iL^2\omega}{\nu})}. \tag{5.44}$$

5.2.2 Region II

The boundary conditions in region II are symmetric at the center ($z = 0$) and periodic between grooves ($z = 1$). At the fixed height $y = H$, the slip velocity is oscillating with time. The boundary condition at $y = H$ is:

$$\hat{\Psi}_{\mathrm{II}y}(H, z) = 1. \tag{5.45}$$

The general solution in region II is:

$$\begin{aligned}\hat{\Psi}_{\mathrm{II}}(y, z) = E_0 \exp\left[\sqrt{\frac{iL^2\omega}{\nu}}y\right] + F_0 \exp\left[-\sqrt{\frac{iL^2\omega}{\nu}}y\right] + R_0 \\ + \sum_{n=1}^{\infty} \cos(\gamma_n z)\left[E_n \exp\left(-\gamma_n y\right) + F_n \exp\left(-\sqrt{\gamma_n^2 + \frac{iL^2\omega}{\nu}}y\right)\right].\end{aligned} \tag{5.46}$$

Integrating the top boundary condition (5.45) from 0 to 1 gives:

$$\sqrt{\frac{iL^2\omega}{\nu}}\left[E_0 \exp\left(\sqrt{\frac{iL^2\omega}{\nu}}H\right) - F_0 \exp\left(-\sqrt{\frac{iL^2\omega}{\nu}}H\right)\right] = 1. \tag{5.47}$$

5.2.3 Between Region I and Region II

The dimensionless boundary condition between regions I and II:

$$\hat{\Psi}_{\mathrm{II}} = \begin{cases} \hat{\Psi}_{\mathrm{I}}, & 0 \leqslant z < a, \\ 0, & a < z \leqslant 1; \end{cases} \tag{5.48}$$

$$\hat{\Psi}_{\mathrm{II}y} = \begin{cases} \hat{\Psi}_{\mathrm{I}y}, & 0 \leqslant z < a, \\ 0, & a < z \leqslant 1; \end{cases} \tag{5.49}$$

$$\hat{\Psi}_{\mathrm{II}yy} = \hat{\Psi}_{\mathrm{I}yy}, \quad 0 \leqslant z \leqslant a, \tag{5.50}$$

$$\hat{\Psi}_{\mathrm{II}yyy} = \hat{\Psi}_{\mathrm{I}yyy}, \quad 0 \leqslant z \leqslant a. \tag{5.51}$$

Integrating equation (5.48) from 0 to 1 gives:

$$E_0 + F_0 + R_0 = \sum_{n=1}^{\infty} \frac{(-1)^{n+1}}{\alpha_n} \left[A_{1n} + A_{2n} \exp\left(-2\sqrt{\alpha_n^2 + \frac{iL^2\omega}{\nu}} b \right) + A_{3n} + A_{4n} \exp\left(-2\alpha_n b\right) \right]. \tag{5.52}$$

Multiplying by $\cos(\gamma_m z)$ and integrating yields:

$$\frac{1}{2}(E_m + F_m) = \sum_{n=1}^{\infty} L_{mn} \left[A_{1n} + A_{2n} \exp\left(-2\sqrt{\alpha_n^2 + \frac{iL^2\omega}{\nu}} b \right) + A_{3n} + A_{4n} \exp(-2\alpha_n b) \right] \tag{5.53}$$

Integrating equation (5.49) from 0 to 1 yields:

$$(E_0 - F_0)\sqrt{\frac{iL^2\omega}{\nu}} = \sum_{n=1}^{\infty} \frac{(-1)^{n+1}}{\alpha_n} \cdot \left\{ \sqrt{\alpha_n^2 + \frac{iL^2\omega}{\nu}} \left[A_{1n} - A_{2n} \exp\left(-2\sqrt{\alpha_n^2 + \frac{iL^2\omega}{\nu}} b \right) \right] + \alpha_n \left[A_{3n} - A_{4n} \exp(-2\alpha_n b) \right] \right\} + \sum_{n=1}^{\infty} C_n \beta_n J_{0n}. \tag{5.54}$$

Multiplying by $\cos(\gamma_m z)$ and integrating equation (5.49) from 0 to 1 yields:

$$-\frac{1}{2}\left(\gamma_m E_m + \sqrt{\gamma_m^2 + \frac{iL^2\omega}{\nu}} F_m \right) = \sum_{n=1}^{\infty} L_{mn} \left\{ \sqrt{\alpha_n^2 + \frac{iL^2\omega}{\nu}} \cdot \left[A_{1n} - A_{2n} \exp\left(-2\sqrt{\alpha_n^2 + \frac{iL^2\omega}{\nu}} b \right) \right] + \alpha_n \left[A_{3n} - A_{4n} \exp(-2\alpha_n b) \right] \right\} + \sum_{n=1}^{\infty} C_n \beta_n J_{mn}, \tag{5.55}$$

where

$$J_{0n} = \frac{1 - \exp\left(-2\sqrt{\beta_n^2 + \frac{iL^2\omega}{\nu}}a\right)}{\sqrt{\beta_n^2 + \frac{iL^2\omega}{\nu}}} + \frac{\left[1 + \exp\left(-2\sqrt{\beta_n^2 + \frac{iL^2\omega}{\nu}}a\right)\right]\left[1 - \exp(2\beta_n a)\right]}{\beta_n\left[1 + \exp(2\beta_n a)\right]}, \tag{5.56}$$

$$\begin{aligned} J_{mn} = &-\left\{\frac{iL^2\omega}{\nu}\gamma_m\left[1 + \exp(-2\beta_n a)\right]\left(1 + \exp\left(-2\sqrt{\beta_n^2 + \frac{iL^2\omega}{\nu}}a\right)\right)\sin(\gamma_m a)\right. \\ &+\left[\beta_n\left(\beta_n^2 + \gamma_m^2 + \frac{iL^2\omega}{\nu}\right)\left(1 - \exp(-2\beta_n a)\right)\left(1 + \exp\left(-2\sqrt{\beta_n^2 + \frac{iL^2\omega}{\nu}}a\right)\right)\right. \\ &\left.\left.+\sqrt{\beta_n^2 + \frac{iL^2\omega}{\nu}}\left(\beta_n^2 + \gamma_m^2\right)\left(1 + \exp\left(-2\beta_n a\right)\right)\left(1 - \exp\left(-2\sqrt{\beta_n^2 + \frac{iL^2\omega}{\nu}}a\right)\right)\right]\right. \\ &\left.\cos(\gamma_m a)\right\} \Big/ \left\{\left[1 + \exp(-2\beta_n a)\right]\left(\beta_n^2 + \gamma_m^2\right)\left(\beta_n^2 + \gamma_m^2 + \frac{iL^2\omega}{\nu}\right)\right\} \end{aligned} \tag{5.57}$$

Multiplying equation (5.50) and equation (5.51) by $\cos(\alpha_m z)$ and integrating from 0 to a yields:

$$\begin{aligned} &\frac{a}{2}\left\{\left(\alpha_m^2 + \frac{iL^2\omega}{\nu}\right)\left[A_{1m} + A_{2m}\exp\left(-2\sqrt{\alpha_m^2 + \frac{iL^2\omega}{\nu}}b\right)\right]\right. \\ &\left.+\alpha_m^2\left[A_{3m} + A_{4m}\exp\left(-2\alpha_m b\right)\right]\right\} \\ &= \frac{iL^2\omega}{\nu}(E_0 + F_0)\frac{(-1)^{m+1}}{\alpha_m} + \sum_{n=1}^{\infty} L_{nm}\left[\gamma_n^2 E_n + \left(\gamma_n^2 + \frac{iL^2\omega}{\nu}\right)F_n\right], \end{aligned} \tag{5.58}$$

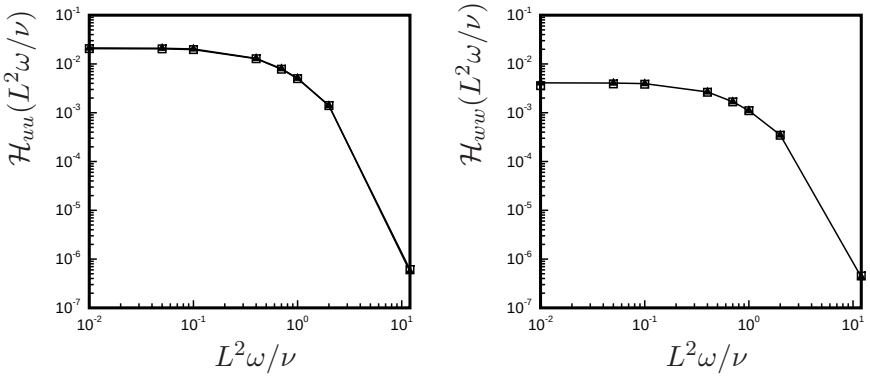

Figure 5.2: Comparison of $\mathcal{H}$ computed from DNS (▲) with analytical solutions (□). $H = 5$. (a) Streamwise slip velocity boundary condition. (b) Spanwise slip velocity boundary condition.

and

$$\frac{a}{2}\left\{\left(\sqrt{\alpha_m^2+\frac{iL^2\omega}{\nu}}\right)^3\left[A_{1m}-A_{2m}\exp\left(-2\sqrt{\alpha_m^2+\frac{iL^2\omega}{\nu}}b\right)\right]\right.$$
$$\left.+\alpha_m^3\left(A_{3m}-A_{4m}\exp\left(-2\alpha_m b\right)\right)\right\}$$
$$=\left(\sqrt{\frac{iL^2\omega}{\nu}}\right)^3(E_0-F_0)\frac{(-1)^{m+1}}{\alpha_m}-\sum_{n=1}^{\infty}L_{nm}\left[\gamma_n^3E_n+\left(\sqrt{\gamma_n^2+\frac{iL^2\omega}{\nu}}\right)^3F_n\right], \quad (5.59)$$

respectively. Finally, E_m and F_m are truncated to M terms, A_n and B_n are truncated to $N = \mathrm{Int}[aM]$ terms, C_n and D_n are truncated to $K = \mathrm{Int}[bM]$ terms and solved from a system of equations constructed with equations (5.39), (5.42), (5.43), (5.47), (5.52), (5.53), (5.54), (5.55), (5.58), (5.59) in MATLAB. Comparison of the transfer functions between the DNS results and the analytical solutions over the range of interest $L^2\omega/\nu \in (0.01, 12)$ is shown in figure 5.2, and seen to be in excellent agreement. Here, analytically the energy spectra is $\Phi_(\omega) = \tilde{u_i}\tilde{u_i}^*$, and the transfer function is given by

$$\mathcal{H}_{u_iu_i}(L^2\omega/\nu)=\sqrt{\frac{\Phi_{\mathrm{output}}(L^2\omega/\nu)}{\Phi_{\mathrm{input}}(L^2\omega/\nu)}}=\tilde{u}_{i\mathrm{I}}\tilde{u}_{i\mathrm{I}}^*, \quad (5.60)$$

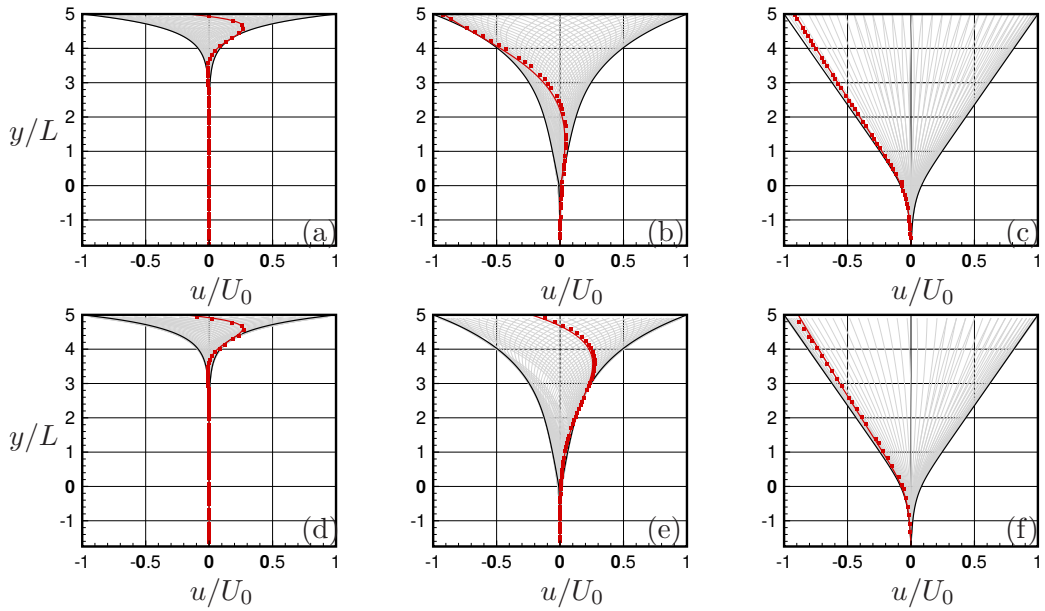

Figure 5.3: Black solid lines: envelopes of the analytical solutions; grey solid lines: DNS solutions at different time instance; red solid lines: analytical instantaneous solutions; red symbols: DNS instantaneous solutions at the same time phase as the analytical solutions. $H/L = 5$. (a-c)$L = 1$, (d-f)$L = 18/3500$. (a)(d) $L^2\omega/\nu = 12$, (b)(e) $L^2\omega/\nu = 1$, (c)(f) $L^2\omega/\nu = 0.01$.

where $\tilde{u_{i\mathrm{I}}}$ is the Fourier transform of the solution of the point in region I in streamwise or spanwise direction.

5.3 Validation of the unsteady Stokes solution

The analytical solution agrees well with DNS results as is shown in figure 5.3. The boundary condition in DNS is the same as the modeled problem. By comparing the upper rows and lower rows in figure 5.3, it is clear that the results scale with the dimensionless number $(L^2\omega/\nu)$. Also, as $(L^2\omega/\nu)$ decreases, the freestream oscillations penetrate deeper into the grooves, thereby increasing the transfer function.

Chapter 6

Theoretical study of multiphase unsteady Stokes flow over grooved surfaces

We study the effect of freestream unsteadiness on the *multiphase* flow inside the SHS grooves. We obtain analytical solutions for unsteady Stokes flow over an array of longitudinal grooves with two different fluids of arbitrary density and viscosity. The interfacial stress is finite and obtained as part of the solution. The solution is applicable to both air and liquid-infused surfaces. §6.1 and §6.2 construct and solve the model problem analytically for longitudinal and transverse flows respectively. In §6.3, the analytical solution is validated against VOF simulation results. A parametric study of oscillating frequency, Reynolds number, and multiphase interface location is performed in §6.4. Concluding remarks are made in §6.5.

6.1 Longitudinal flow

We consider the incompressible and viscous flow over an array of grooves driven by an oscillating velocity. A schematic of the problem is shown in figure 6.1. We introduce

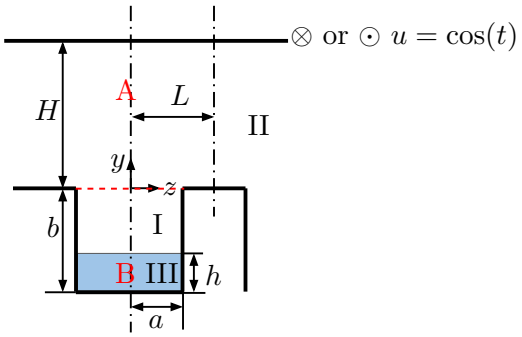

Figure 6.1: Schematic of the model problem for longitudinal flow and the coordinate system. The red dashed line indicates the boundary between region I and region II. x-direction is into the paper.

non-dimensional variables as:

$$u = u^*/U_0, \tag{6.1}$$

$$y = y^*/L, \tag{6.2}$$

$$t = t^*\omega, \tag{6.3}$$

where the variables with the asterisks represent dimensional variables, u is the streamwise velocity, U_0 is the velocity magnitude, L is the half period of the groove, and ω is the frequency of the oscillating velocity. The groove geometry at the lower wall, $y = 0$ is defined by its depth b and half-groove width a. The multiphase interface is located at $y = -(b - h)$, and does not change with time. In this section, the velocity is along the direction of the grooves. The oscillating velocity $u(H, z, t) = \cos(t)$. The groove is periodic in the span and symmetric at the center.

The dimensionless governing equation is:

$$\frac{\partial u}{\partial t} = \frac{\nu}{L^2\omega}\left(\frac{\partial^2 u}{\partial z^2} + \frac{\partial^2 u}{\partial y^2}\right), \tag{6.4}$$

where $L^2\omega/\nu$ is the non-dimensional Womersley number. The domain of interest is

divided into three rectangular regions. Regions I and III represent the two types of fluid inside the grooves and region II represents the fluid between $y = 0$ and the oscillating plane at $y = H$.

For oscillatory flow, the solution is assumed to be of the form:

$$u = \Re(\hat{u}\exp(it)) = \Re(Y(y)Z(z)\exp(it)). \tag{6.5}$$

Substituting (6.5) into (6.4) we obtain:

$$i\hat{u} = \frac{\nu}{L^2\omega}\left(\frac{\partial^2\hat{u}}{\partial y^2} + \frac{\partial^2\hat{u}}{\partial z^2}\right). \tag{6.6}$$

By separation of variables $\hat{u}(y,z) = Y(y)Z(z)$, we obtain $\frac{Y''}{Y} + \frac{Z''}{Z} = \frac{iL^2\omega}{\nu}$.

We obtain the general solutions as a series of eigensolutions in the three regions independently, and determine the constant coefficients by matching the boundary conditions between each of the neighboring regions. The separable solutions are independent of time, therefore the boundary conditions can be written as:

$$\hat{u}_{\mathrm{II}} = \begin{cases} \hat{u}_{\mathrm{I}}, & 0 \leqslant z < a, \\ 0, & a < z \leqslant 1; \end{cases} \tag{6.7}$$

$$\frac{\partial\hat{u}_{\mathrm{I}}(0,z)}{\partial y} = \frac{\partial\hat{u}_{\mathrm{II}}(0,z)}{\partial y}; \quad 0 \leqslant z < a \tag{6.8}$$

$$\hat{u}_{\mathrm{I}}(-b+h,z) = \hat{u}_{\mathrm{III}}(-b+h,z); \quad 0 \leqslant z < a, \tag{6.9}$$

$$\frac{\partial\hat{u}_{\mathrm{I}}(-b+h,z)}{\partial y} = \mu_r\frac{\partial\hat{u}_{\mathrm{III}}(-b+h,z)}{\partial y}; \quad 0 \leqslant z < a \tag{6.10}$$

where $\mu_r = \mu_A/\mu_B$ is the viscosity ratio between the external fluid A and the internal fluid B (blue shaded area in figure 6.1). When $\mu_r = 0$, the interface is shear-free. Fluid A can penetrate into the groove.

6.1.1 Region I

The boundary conditions are no-slip at the wall ($z = a$), and symmetry at the groove center ($z = 0$). In terms of $\hat{u}(y, z) = Y(y)Z(z)$,

$$\frac{\partial \hat{u}_{\mathrm{I}}(y,0)}{\partial z} = 0 \Rightarrow Z'(0) = 0, \tag{6.11}$$

$$\hat{u}_{\mathrm{I}}(y,a) = 0 \Rightarrow Z(a) = 0. \tag{6.12}$$

From (6.11) and (6.12), we get $Z_n(z) = \cos(\alpha_n z)$, where $\alpha_n = (n - \frac{1}{2})\frac{\pi}{a}$. This implies $\frac{Y''}{Y} = \frac{iL^2\omega}{\nu} + \alpha_n^2$. The solution for Y is therefore:

$$Y_n(y) = A_{1n} \exp\left(\sqrt{\alpha_n^2 + \frac{iL^2\omega}{\nu}}\, y\right) + A_{2n} \exp\left(-\sqrt{\alpha_n^2 + \frac{iL^2\omega}{\nu}}\, y\right).$$

A separable solution for $\hat{u}_{\mathrm{I}}$ is:

$$\begin{aligned}\hat{u}_{\mathrm{I}}(y,z) = \sum_{n=1}^{\infty} \cos(\alpha_n z) \Bigg\{ & A_{1n} \exp\left[\sqrt{\alpha_n^2 + \frac{iL^2\omega}{\nu}}\, y\right] \\ & + A_{2n} \exp\left[-\sqrt{\alpha_n^2 + \frac{iL^2\omega}{\nu}}\,(y + 2b - 2h)\right]\Bigg\}.\end{aligned} \tag{6.13}$$

The coefficients A_{1n} and A_{2n} will be obtained by matching adjoining regions below.

6.1.2 Region II

The boundary conditions in region II are symmetry at the center ($z = 0$), and between grooves ($z = 1$). Also, at the fixed height $y = H$, the slip velocity oscillates with time.

$$\frac{\partial \hat{u}_{\mathrm{II}}(y,0)}{\partial z} = 0 \Rightarrow Z'(0) = 0, \tag{6.14}$$

$$\frac{\partial \hat{u}_{\mathrm{II}}(y,1)}{\partial z} = 0 \Rightarrow Z'(1) = 0, \tag{6.15}$$

$$\hat{u}(H,z) = 1. \tag{6.16}$$

The solution for Z must satisfy equations (6.14) and (6.15), i.e.: $Z_n(z) = \cos(\gamma_n z)$, where $\gamma_n = n\pi$. Hence the solutions for Y must satisfy: $\frac{Y''}{Y} = \frac{iL^2\omega}{\nu} + \gamma_n^2$, for any integer $n \geqslant 0$. Therefore the eigensolution for Y is:

$$Y_n(y) = B_n \exp\left(\sqrt{\gamma_n^2 + \frac{iL^2\omega}{\nu}}y\right) + C_n \exp\left(-\sqrt{\gamma_n^2 + \frac{iL^2\omega}{\nu}}y\right). \tag{6.17}$$

Therefore, the general solution in region II is:

$$\begin{aligned} \hat{u}_{\mathrm{II}}(y,z) &= B_0 \exp\left[\sqrt{\frac{iL^2\omega}{\nu}}y\right] + C_0 \exp\left[-\sqrt{\frac{iL^2\omega}{\nu}}y\right] \\ &+ \sum_{n=1}^{\infty} \cos(\gamma_n z)\left[B_n \exp\left(\sqrt{\gamma_n^2 + \frac{iL^2\omega}{\nu}}y\right) + C_n \exp\left(-\sqrt{\gamma_n^2 + \frac{iL^2\omega}{\nu}}y\right)\right]. \end{aligned} \tag{6.18}$$

The inhomogeneous behavior of the flow in the spanwise direction caused by the groove is represented by $\cos(\gamma_n z)$, and should diminish as the distance to the groove increases; therefore the coefficients $B_n = 0$. Integrating the boundary condition (6.16) from 0 to 1 yields:

$$B_0 \exp\left[\sqrt{\frac{L^2\omega}{2\nu}}(1+i)H\right] + C_0 \exp\left[-\sqrt{\frac{L^2\omega}{2\nu}}(1+i)H\right] = 1. \tag{6.19}$$

6.1.3 Region III

The general solution for region III that satisfies the no-slip condition on the walls and symmetry is:

$$\begin{aligned} \hat{u}_{\mathrm{III}}(y,z) = \sum_{n=1}^{\infty} D_n \cos(\alpha_n z)\Bigg[&\exp\left(\sqrt{\alpha_n^2 + \frac{iL^2\omega}{\nu}}(y+b-h)\right) \\ &- \exp\left(-\sqrt{\alpha_n^2 + \frac{iL^2\omega}{\nu}}(y+b+h)\right)\Bigg]. \end{aligned} \tag{6.20}$$

6.1.4 Solving for coefficients in the general solutions

Between region I and region III

At the interface, the boundary satisfies equations (6.9) and (6.10). Multiplying (6.9) and (6.10) by $\cos(\alpha_m z)$ and integrating from 0 to a respectively, yields:

$$(A_{1m} + A_{2m}) \exp\left[-\sqrt{\alpha_m^2 + \frac{iL^2\omega}{\nu}}(b-h)\right] = D_m \left[1 - \exp\left(-2\sqrt{\alpha_m^2 + \frac{iL^2\omega}{\nu}}h\right)\right], \tag{6.21}$$

and

$$(A_{1m} - A_{2m}) \exp\left[-\sqrt{\alpha_m^2 + \frac{iL^2\omega}{\nu}}(b-h)\right] = \mu_r D_m \left[1 + \exp\left(-2\sqrt{\alpha_m^2 + \frac{iL^2\omega}{\nu}}h\right)\right]. \tag{6.22}$$

Between region I and region II

Next, we determine the unknown constants C_0, C_n and D_n by applying the boundary condition between the two regions. Integrating (6.7) from 0 to 1,

$$B_0 + C_0 = \sum_{n=1}^{\infty} -\frac{(-1)^n}{\alpha_n}\left[A_{1n} + A_{2n}\exp\left(-2\sqrt{\alpha_n^2 + \frac{iL^2\omega}{\nu}}(b-h)\right)\right]. \tag{6.23}$$

Multiplying (6.7) by $\cos(\gamma_m z)$ and integrating from 0 to 1,

$$C_m = 2\sum_{n=1}^{\infty} L_{mn}\left[A_{1n} + A_{2n}\exp\left(-2\sqrt{\alpha_n^2 + \frac{iL^2\omega}{\nu}}(b-h)\right)\right], \tag{6.24}$$

where $L_{mn} = \int_0^a \cos(\alpha_n z)\cos(\gamma_m z)dz$. Multiplying (6.8) by $\cos(\alpha_m z)$ and integrating from 0 to a,

$$\begin{aligned} &-\frac{(-1)^m}{\alpha_m}\sqrt{\frac{iL^2\omega}{\nu}}(B_0 - C_0) - \sum_{n=1}^{\infty} C_n L_{nm}\sqrt{\gamma_n^2 + \frac{iL^2\omega}{\nu}} \\ &= \frac{a}{2}\sqrt{\alpha_m^2 + \frac{iL^2\omega}{\nu}}\left[A_{1m} - A_{2m}\exp\left(-2\sqrt{\alpha_m^2 + \frac{iL^2\omega}{\nu}}(b-h)\right)\right]. \end{aligned} \tag{6.25}$$

$L^2\omega/\nu\backslash$M	5	10	15	20	25	30	35	40	45
0.1875	0.0232	0.0234	0.0234	0.0234	0.0235	0.0235	0.0235	0.0235	0.0235
0.0625	0.0366	0.0369	0.0369	0.0369	0.0370	0.0370	0.0370	0.0370	0.0370

Table 6.1: Convergence of $\Re\left(B_0 + C_0\right)$, $a = 0.6$, $b = 1.25$, $h = 0.9b$, $H = 5$, $\mu_r = 0.02$.

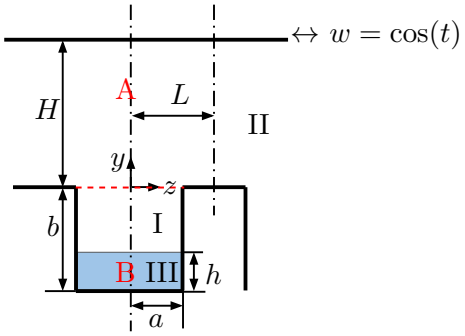

Figure 6.2: Schematic of the model problem for transverse flow. The red dashed line indicates the boundary between region I and region II. x-direction is into the paper.

Finally, C_m is truncated to M terms and D_n is truncated to $N = \text{Int}[aM]$ terms. By solving equations (6.19), and (6.21) to (6.25) as a system of equations in MATLAB, we can obtain all the unknown coefficients in the solution. Table 6.1 shows the convergence of $B_0 + C_0$ with M. $B_0 + C_0$ is accurate up to the fourth digit when M is greater than 25.

6.2 Transverse flow

For transverse flow, the freestream oscillating velocity is in the z direction: $w(H, z, t) = \cos(t)$. A schematic of the problem is shown in figure 6.2. The dimensionless governing equation is:

$$i\nabla^2\hat{\Psi} = \frac{\nu}{L^2\omega}\nabla^4\hat{\Psi}, \tag{6.26}$$

with the streamfunction ($\hat{\Psi}$) to replace $\hat{w} = \frac{\partial\hat{\Psi}}{\partial y}$ and $\hat{v} = -\frac{\partial\hat{\Psi}}{\partial z}$.

6.2.1 Region I

$\hat{\Psi}$ and its normal derivatives are zero at the walls and symmetric at the groove center ($z = 0$). A separable solution for $\hat{\Psi}_{\mathrm{I}}$ is:

$$\hat{\Psi}_I(y,z) = \sum_{n=1}^{\infty} \cos(\alpha_n z) f_n(y) + \sum_{n=1}^{\infty} C_n \sin(\lambda_n y)\phi_n(\lambda_n; z), \tag{6.27}$$

where $\lambda_n = n\pi/(b-h)$, and

$$\begin{aligned} f_n(y) = A_{1n} \exp\left(\sqrt{\alpha_n^2 + \frac{iL^2\omega}{\nu}}\, y\right) + A_{2n} \exp\left[-\sqrt{\alpha_n^2 + \frac{iL^2\omega}{\nu}}\,(y + 2(b-h))\right] \\ + A_{3n}\exp(\alpha_n y) + A_{4n}\exp[-\alpha_n(y+2(b-h))], \end{aligned} \tag{6.28}$$

$$\begin{aligned} \phi_n(\lambda_n; z) = \exp\left(\sqrt{\lambda_n^2 + \frac{iL^2\omega}{\nu}}\,(z-a)\right) + \exp\left(-\sqrt{\lambda_n^2 + \frac{iL^2\omega}{\nu}}\,(z+a)\right) \\ - \frac{1 + \exp\left(-2\sqrt{\lambda_n^2 + \frac{iL^2\omega}{\nu}}\, a\right)}{1 + \exp(-2\lambda_n a)} \left[\exp(\lambda_n(z-a)) + \exp(-\lambda_n(z+a))\right]. \end{aligned} \tag{6.29}$$

At the side wall

$$\tilde{\Psi}_{Iz}(y,a) = 0. \tag{6.30}$$

Multiplying this by $\sin(\lambda_m y)$ and integrating from $-(b-h)$ to 0 yields:

$$\sum_{n=1}^{\infty} \alpha_n (-1)^n (A_{1n}K_{1mn} + A_{2n}K_{2mn} + A_{3n}K_{3mn} + A_{4n}K_{4mn}) + \frac{b-h}{2} C_m \phi_m'(\lambda_m; a) = 0, \tag{6.31}$$

where

$$K_{1mn} = \frac{\lambda_m \left[\exp\left(-\sqrt{\alpha_n^2 + \frac{iL^2\omega}{\nu}}(b-h)\right)(-1)^m - 1\right]}{\alpha_n^2 + \lambda_m^2 + \frac{iL^2\omega}{\nu}},$$

$$K_{2mn} = \frac{\lambda_m \left[\exp\left(\sqrt{\alpha_n^2 + \frac{iL^2\omega}{\nu}}(b-h)\right)(-1)^m - 1\right]\exp\left(-2\sqrt{\alpha_n^2 + \frac{iL^2\omega}{\nu}}(b-h)\right)}{\alpha_n^2 + \lambda_m^2 + \frac{iL^2\omega}{\nu}},$$

$$K_{3mn} = \frac{\lambda_m \left[\exp\left(-\alpha_n(b-h)\right)(-1)^m - 1\right]}{\alpha_n^2 + \lambda_m^2},$$

$$K_{4mn} = \frac{\lambda_m \left[\exp\left(\alpha_n(b-h)\right)(-1)^m - 1\right]\exp\left(-2\alpha_n(b-h)\right)}{\alpha_n^2 + \lambda_m^2}.$$

The location of the interface is assumed to be fixed at $y = -(b-h)$ such that $\frac{\partial \hat{\Psi}_I}{\partial z} = 0$, yielding,

$$\exp\left(-\sqrt{\alpha_n^2 + \frac{iL^2\omega}{\nu}}(b-h)\right)(A_{1n} + A_{2n}) + \exp\left(-\alpha_n(b-h)\right)(A_{3n} + A_{4n}) = 0. \quad (6.32)$$

6.2.2 Region II

The boundary conditions in region II are symmetry at the center ($z = 0$) and periodic between grooves ($z = 1$). At the fixed height $y = H$, the slip velocity oscillates with time. The boundary condition at $y = H$ is:

$$\hat{\Psi}_{\mathrm{II}y}(H, z) = 1. \quad (6.33)$$

The general solution in region II is:

$$\begin{aligned}\hat{\Psi}_{\mathrm{II}}(y, z) = E_0 \exp\left[\sqrt{\frac{iL^2\omega}{\nu}}y\right] + F_0 \exp\left[-\sqrt{\frac{iL^2\omega}{\nu}}y\right] + R_0 \\ + \sum_{n=1}^{\infty} \cos(\gamma_n z)\left[E_n \exp\left(-\gamma_n y\right) + F_n \exp\left(-\sqrt{\gamma_n^2 + \frac{iL^2\omega}{\nu}}y\right)\right].\end{aligned} \quad (6.34)$$

Integrating the top boundary condition (6.33) from 0 to 1 gives:

$$\sqrt{\frac{iL^2\omega}{\nu}}\left[E_0\exp\left(\sqrt{\frac{iL^2\omega}{\nu}}H\right)-F_0\exp\left(-\sqrt{\frac{iL^2\omega}{\nu}}H\right)\right]=1. \tag{6.35}$$

6.2.3 Region III

The general solution for region III that satisfies $\hat{\Psi}=0$ on the walls and symmetry at the center is:

$$\hat{\Psi}_{\mathrm{III}}(y,z)=\sum_{n=1}^{\infty}\cos(\alpha_n z)g_n(y)+\sum_{n=1}^{\infty}\sin[\beta_n(y+b-h)]\phi_n(\beta_n;z), \tag{6.36}$$

where $\beta_n=n\pi/h$,

$$\begin{aligned}g_n(y)=&B_{1n}\exp\left(\sqrt{\alpha_n^2+\frac{iL^2\omega}{\nu}}(y+b-h)\right)+B_{2n}\exp\left(-\sqrt{\alpha_n^2+\frac{iL^2\omega}{\nu}}(y+b+h)\right)\\&+B_{3n}\exp(\alpha_n(y+b-h))+B_{4n}\exp(-\alpha_n(y+b+h)),\end{aligned} \tag{6.37}$$

and $\phi_n(\beta_n;z)$ is the same as (6.29) with a different eigenvalues. $\hat{\Psi}_{\mathrm{III}}$ satisfies:

$$\hat{\Psi}_{\mathrm{III}}(-b,z)=0, \tag{6.38}$$

$$\hat{\Psi}_{\mathrm{III}y}(-b,z)=0, \tag{6.39}$$

at the bottom wall, and

$$\hat{\Psi}_{\mathrm{III}z}(y,a)=0, \tag{6.40}$$

at the side wall $z=a$. Equation (6.38) yields:

$$\exp\left(-\sqrt{\alpha_n^2+\frac{iL^2\omega}{\nu}}h\right)(B_{1n}+B_{2n})+\exp(-\alpha_n h)(B_{3n}+B_{4n})=0. \tag{6.41}$$

Multiplying equation (6.39) by $\cos(\alpha_m z)$ and integrating from 0 to a:

$$\frac{a}{2}\left[\sqrt{\alpha_m^2+\frac{iL^2\omega}{\nu}}\exp\left(-\sqrt{\alpha_m^2+\frac{iL^2\omega}{\nu}}h\right)(B_{1m}-B_{2m})+\right.$$
$$\left.\alpha_m\exp\left(-\alpha_m h\right)(B_{3m}-B_{4m})\right]+\sum_{n=1}^{\infty}D_n\beta_n(-1)^n H_{1mn}=0, \tag{6.42}$$

where

$$H_{1mn}=\frac{\frac{iL^2\omega}{\nu}\alpha_m(-1)^m\left[\exp\left(-2\sqrt{\beta_n^2+\frac{iL^2\omega}{\nu}}a\right)\right]}{(\alpha_m^2+\beta_n^2)(\alpha_m^2+\beta_n^2+\frac{iL^2\omega}{\nu})}. \tag{6.43}$$

Multiplying equation (6.40) by $\sin(\beta_m(y+b-h))$ and integrating from $-b$ to $-(b-h)$ gives

$$\sum_{n=1}^{\infty}\alpha_n(-1)^n(B_{1n}P_{1mn}+B_{2n}P_{2mn}+B_{3n}P_{3mn}+B_{4n}P_{4mn})+\frac{h}{2}D_m\phi'_m(\beta_m;a)=0, \tag{6.44}$$

where

$$P_{1mn}=\frac{\beta_m\left[\exp\left(-\sqrt{\alpha_n^2+\frac{iL^2\omega}{\nu}}h\right)(-1)^m-1\right]}{\alpha_n^2+\beta_m^2+\frac{iL^2\omega}{\nu}},$$
$$P_{2mn}=\frac{\beta_m\left[\exp\left(\sqrt{\alpha_n^2+\frac{iL^2\omega}{\nu}}h\right)(-1)^m-1\right]\exp\left(-2\sqrt{\alpha_n^2+\frac{iL^2\omega}{\nu}}h\right)}{\alpha_n^2+\beta_m^2+\frac{iL^2\omega}{\nu}},$$
$$P_{3mn}=\frac{\beta_m\left[\exp\left(-\alpha_n h\right)(-1)^m-1\right]}{\alpha_n^2+\beta_m^2},$$
$$P_{4mn}=\frac{\beta_m\left[\exp\left(\alpha_n h\right)(-1)^m-1\right]\exp\left(-2\alpha_n h\right)}{\alpha_n^2+\beta_m^2}.$$

The location of the interface is assumed to be fixed at $y=-(b-h)$, yielding,

$$B_{1n}+B_{2n}\exp\left(-2\sqrt{\alpha_n^2+\frac{iL^2\omega}{\nu}}h\right)+B_{3n}+B_{4n}\exp\left(-2\alpha_n h\right)=0. \tag{6.45}$$

6.2.4 Solving for coefficients in the general solutions

Between region I and region III

The boundary conditions between region I and region III are:

$$\hat{\Psi}_{\mathrm{I}y}(-b+h,z) = \hat{\Psi}_{\mathrm{III}y}(-b+h,z), \tag{6.46}$$

$$\hat{\Psi}_{\mathrm{I}yy}(-b+h,z) = \mu_r \hat{\Psi}_{\mathrm{III}yy}(-b+h,z). \tag{6.47}$$

Multiplying (6.46) and (6.47) by $\cos(\alpha_m z)$ and integrating from 0 to a, respectively:

$$\frac{a}{2} f'_m(-(b-h)) + \sum_{n=1}^{\infty} C_n \lambda_n H_{2mn} = \frac{a}{2} g'_m(-(b-h)) + \sum_{n=1}^{\infty} D_n \beta_n H_{1mn}. \tag{6.48}$$

and

$$\frac{a}{2} f''_n(-(b-h)) = \mu_r \left[\frac{a}{2} g''_n(-(b-h))\right], \tag{6.49}$$

where

$$H_{2mn} = \frac{\frac{iL^2\omega}{\nu}\alpha_m(-1)^m \left[\exp\left(-2\sqrt{\lambda_n^2 + \frac{iL^2\omega}{\nu}}a\right)\right]}{(\alpha_m^2+\lambda_n^2)(\alpha_m^2+\lambda_n^2+\frac{iL^2\omega}{\nu})}. \tag{6.50}$$

Between region I and region II

The boundary condition between regions I and II:

$$\hat{\Psi}_{\mathrm{II}} = \begin{cases} \hat{\Psi}_{\mathrm{I}}, & 0 \leqslant z < a, \\ 0, & a < z \leqslant 1; \end{cases} \tag{6.51}$$

$$\hat{\Psi}_{\mathrm{II}y} = \begin{cases} \hat{\Psi}_{\mathrm{I}y}, & 0 \leqslant z < a, \\ 0, & a < z \leqslant 1; \end{cases} \tag{6.52}$$

$$\hat{\Psi}_{\mathrm{II}yy} = \hat{\Psi}_{\mathrm{I}yy}; \quad 0 \leqslant z \leqslant a, \tag{6.53}$$

$$\hat{\Psi}_{\mathrm{II}yyy} = \hat{\Psi}_{\mathrm{I}yyy}; \quad 0 \leqslant z \leqslant a. \tag{6.54}$$

Integrating equation (6.51) from 0 to 1 gives:

$$E_0 + F_0 + R_0 = \sum_{n=1}^{\infty} \frac{(-1)^{n+1}}{\alpha_n} \left[A_{1n} + A_{2n} \exp\left(-2\sqrt{\alpha_n^2 + \frac{iL^2\omega}{\nu}}(b-h) \right) \right.$$
$$\left. + A_{3n} + A_{4n} \exp\left(-2\alpha_n(b-h)\right) \right]. \tag{6.55}$$

Multiplying by $\cos(\gamma_m z)$ and integrating yields:

$$\frac{1}{2}(E_m + F_m) = \sum_{n=1}^{\infty} L_{mn} \left[A_{1n} + A_{2n} \exp\left(-2\sqrt{\alpha_n^2 + \frac{iL^2\omega}{\nu}}(b-h) \right) \right.$$
$$\left. + A_{3n} + A_{4n} \exp(-2\alpha_n(b-h)) \right]. \tag{6.56}$$

Integrating equation (6.52) from 0 to 1 gives:

$$(E_0 - F_0)\sqrt{\frac{iL^2\omega}{\nu}} = \sum_{n=1}^{\infty} \frac{(-1)^{n+1}}{\alpha_n}$$
$$\cdot \left\{ \sqrt{\alpha_n^2 + \frac{iL^2\omega}{\nu}} \left[A_{1n} - A_{2n} \exp\left(-2\sqrt{\alpha_n^2 + \frac{iL^2\omega}{\nu}}(b-h) \right) \right] \right.$$
$$\left. + \alpha_n \left[A_{3n} - A_{4n} \exp(-2\alpha_n(b-h)) \right] \right\} + \sum_{n=1}^{\infty} C_n \lambda_n J_{0n}. \tag{6.57}$$

Multiplying by $\cos(\gamma_m z)$ and integrate equation (6.52) from 0 to 1 yields:

$$-\frac{1}{2}\left(\gamma_m E_m + \sqrt{\gamma_m^2 + \frac{iL^2\omega}{\nu}} F_m \right) = \sum_{n=1}^{\infty} L_{mn} \left\{ \sqrt{\alpha_n^2 + \frac{iL^2\omega}{\nu}} \right.$$
$$\cdot \left[A_{1n} - A_{2n} \exp\left(-2\sqrt{\alpha_n^2 + \frac{iL^2\omega}{\nu}}(b-h) \right) \right]$$
$$\left. + \alpha_n \left[A_{3n} - A_{4n} \exp(-2\alpha_n(b-h)) \right] \right\} + \sum_{n=1}^{\infty} C_n \lambda_n J_{mn}, \tag{6.58}$$

where

$$J_{0n} = \frac{1 - \exp\left(-2\sqrt{\lambda_n^2 + \frac{iL^2\omega}{\nu}}a\right)}{\sqrt{\lambda_n^2 + \frac{iL^2\omega}{\nu}}} + \frac{\left[1 + \exp\left(-2\sqrt{\lambda_n^2 + \frac{iL^2\omega}{\nu}}a\right)\right]\left[1 - \exp(2\lambda_n a)\right]}{\lambda_n\left[1 + \exp(2\lambda_n a)\right]}, \tag{6.59}$$

$$\begin{aligned} J_{mn} = &-\left\{\frac{iL^2\omega}{\nu}\gamma_m\left[1 + \exp(-2\lambda_n a)\right]\left(1 + \exp\left(-2\sqrt{\lambda_n^2 + \frac{iL^2\omega}{\nu}}a\right)\right)\sin(\gamma_m a)\right. \\ &+\left[\lambda_n\left(\lambda_n^2 + \gamma_m^2 + \frac{iL^2\omega}{\nu}\right)\left(1 - \exp(-2\lambda_n a)\right)\left(1 + \exp\left(-2\sqrt{\lambda_n^2 + \frac{iL^2\omega}{\nu}}a\right)\right)\right. \\ &\left.\left.+\sqrt{\beta_n^2 + \frac{iL^2\omega}{\nu}}\left(\lambda_n^2 + \gamma_m^2\right)\left(1 + \exp\left(-2\lambda_n a\right)\right)\left(1 - \exp\left(-2\sqrt{\lambda_n^2 + \frac{iL^2\omega}{\nu}}a\right)\right)\right]\right. \\ &\left.\cos(\gamma_m a)\right\} \Big/ \left\{\left[1 + \exp(-2\lambda_n a)\right]\left(\lambda_n^2 + \gamma_m^2\right)\left(\lambda_n^2 + \gamma_m^2 + \frac{iL^2\omega}{\nu}\right)\right\}. \end{aligned} \tag{6.60}$$

Multiplying equation (6.53) and equation (6.54) by $\cos(\alpha_m z)$ and integrating from 0 to a yields:

$$\begin{aligned} &\frac{a}{2}\left\{\left(\alpha_m^2 + \frac{iL^2\omega}{\nu}\right)\left[A_{1m} + A_{2m}\exp\left(-2\sqrt{\alpha_m^2 + \frac{iL^2\omega}{\nu}}(b-h)\right)\right]\right. \\ &\left.+\alpha_m^2\left[A_{3m} + A_{4m}\exp\left(-2\alpha_m(b-h)\right)\right]\right\} \\ &= \frac{iL^2\omega}{\nu}(E_0 + F_0)\frac{(-1)^{m+1}}{\alpha_m} + \sum_{n=1}^{\infty} L_{nm}\left[\gamma_n^2 E_n + \left(\gamma_n^2 + \frac{iL^2\omega}{\nu}\right)F_n\right], \end{aligned} \tag{6.61}$$

$L^2\omega/\nu\backslash$M	10	20	30	40	50	60	70
0.1875	0.0069	0.0068	0.0068	0.0068	0.0067	0.0067	0.0067
0.0625	0.0102	0.0101	0.0101	0.0100	0.0100	0.0100	0.0100

Table 6.2: Convergence of $\Re\left(\sqrt{\frac{iL^2\omega}{\nu}}(E_0-F_0)\right)$, $a=0.6$, $b=1.25$, $h=0.9b$, $H=5$, $\mu_r=0.02$.

and

$$\frac{a}{2}\left\{\left(\sqrt{\alpha_m^2+\frac{iL^2\omega}{\nu}}\right)^3\left[A_{1m}-A_{2m}\exp\left(-2\sqrt{\alpha_m^2+\frac{iL^2\omega}{\nu}}(b-h)\right)\right]\right.$$
$$\left.+\alpha_m^3\left(A_{3m}-A_{4m}\exp\left(-2\alpha_m(b-h)\right)\right)\right\}$$
$$=\left(\sqrt{\frac{iL^2\omega}{\nu}}\right)^3(E_0-F_0)\frac{(-1)^{m+1}}{\alpha_m}-\sum_{n=1}^{\infty}L_{nm}\left[\gamma_n^3E_n+\left(\sqrt{\gamma_n^2+\frac{iL^2\omega}{\nu}}\right)^3F_n\right], \quad (6.62)$$

respectively. Finally, E_m and F_m are truncated to M terms, A_n and B_n are truncated to $N=\text{Int}[aM]$ terms, C_n and D_n are truncated to $K=\text{Int}[bM]$ terms and solved from a system of equations constructed with equations (6.31), (6.32), (6.35), (6.41), (6.42), (6.44), (6.45), (6.48), (6.49), (6.55) to (6.58), (6.61), (6.62) in MATLAB. Table 6.2 shows the convergence of averaged velocity magnitude $\Re\left(\sqrt{\frac{iL^2\omega}{\nu}}(E_0-F_0)\right)$ at $y=0$ with M. $\Re\left(\sqrt{\frac{iL^2\omega}{\nu}}(E_0-F_0)\right)$ is accurate up to the fourth digit when M is greater than 30.

6.3 Validation

The solution is first validated against DNS data using the numerical methodology of [83], implemented with VOF given in [108]. Then the lower bound of the solution, representing a steady flow result is validated using the analytical solution in [33], [35], and the simulation result in [61].

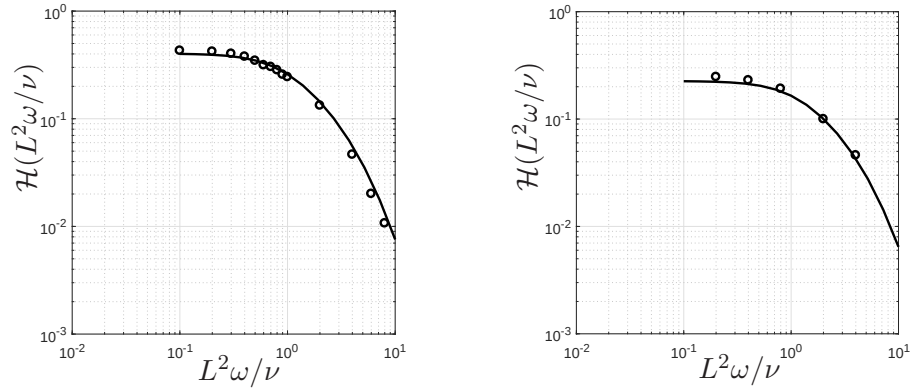

(a) Longitudinal flow (b) Transverse flow

Figure 6.3: Comparison of the transfer function results from VOF (symbols) with analytical solutions (solid line). $L = 1$, $\nu = 1$, $H = 2.5$, $a = 0.875$, $b = h = 1.75$, and $\mu_r = 0.02$.

6.3.1 Validation of the multiphase unsteady solution

The multiphase unsteady solution is validated by DNS with VOF. The results are expressed in the form of the transfer equation defined as:

$$\mathcal{H}\left(\frac{L^2\omega}{\nu}\right) = \sqrt{\frac{\Phi(\frac{iL^2\omega}{\nu})_{\text{output}}}{\Phi(\frac{iL^2\omega}{\nu})_{\text{input}}}} = \begin{cases} \sqrt{\hat{u}_{\text{I}}\hat{u}_{\text{I}}^*}, & \text{longitudinal,} \\ \sqrt{\hat{w}_{\text{I}}\hat{w}_{\text{I}}^*}, & \text{transverse,} \end{cases} \tag{6.63}$$

where the input is considered as the energy of the forcing, and the output is the energy at $y = 0$.

The transfer function shows good agreement between VOF simulation with flat interface ($\sigma \to \infty$) and the analytical solution in figure 6.3. Here, $L^2\omega/\nu$ varies from 0.1 to 1.0, $L = 1$, $\nu = 1$, $H = 2.5$, $h/b = 1.0$, and $\mu_r = 0.02$.

The derivation above considers a flat interface, whereas the curvature of the interface $\nabla \cdot \mathbf{n}$ is determined by the Young-Laplace equation:

$$\Delta p = \sigma \nabla \cdot \mathbf{n}, \tag{6.64}$$

where σ is the surface tension, Δp is the pressure difference sustained by the interface.

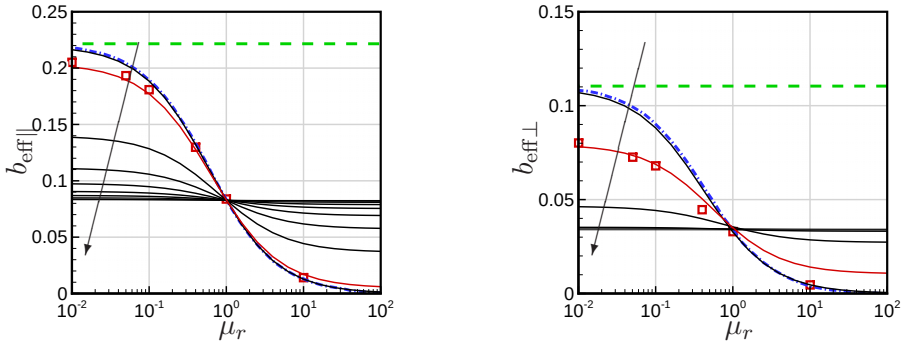

(a) Longitudinal flow

(b) Transverse flow

Figure 6.4: Effective slip length (a) $b_{\text{eff}\parallel}$ and (b) $b_{\text{eff}\perp}$ as a function of viscosity ratio μ_r and the location of the interface h. Green dashed line: [33], blue dashed-dotted line: [35], open square symbols: [61], black solid lines: steady solutions derived in this paper. Arrow indicates the decreasing of the interface height with respect to the groove depth h/b ranging from (a) 100% to 0% by a step of 10%; (b) 100% to 50% by a step of 10%. The red line in each plot is (a) $h/b = 99\%$; (b) $h/b = 97.5\%$. Data obtained from [61] is re-normalized in the same manner as this paper.

When the surface tension $\sigma \to \infty$, the interface is flat.

6.3.2 Validation of the multiphase steady solution

Schönecker et al. [35] considered the flow over an array of grooves being filled with a secondary immiscible fluid driven by a constant shear stress τ_∞ as $y \to \infty$ and derived analytical expressions for effective slip length, with respect to the viscosity ratio of the two fluids. Here, $b_{\text{eff}} \equiv \overline{u}_{\text{II}}/\overline{\partial u_{\text{II}}/\partial y}$, where the overline '$\overline{()}$' represents the averaged quantity across time and span, with both values evaluated at $y = 0$. This solution can serve as a lower bound of the current unsteady solution when $\omega \to 0$ and $y \to \infty$. This asymptotic trend is confirmed by comparing two sets of analytical solutions with $L^2\omega/\nu = 10^{-4}$, $H = 5$; and $\omega = 10^{-5}$, $H = 10$, with the same $a = 0.5$, $b = 1.0$, $h = b$, and $\mu_r = 0.02$. For the two sets of parameters $b_{\text{eff}\parallel} = 0.2101$ and 0.2101, respectively, agreeing upto the $10th$ digit. $b_{\text{eff}\perp} = 0.1032$ and 0.1032, respectively, agreeing upto the $10th$ digit as well. Therefore, $L^2\omega/\nu = 10^{-4}$, and $H = 5$ are used to validate the steady flow solutions.

Figure 6.4 shows a comparison amongst the steady analytical solutions of [33], [35], the simulation results of [61], and the asymptotic result of the analytical solution with $a = 0.5$, $b = 1$, $L^2\omega/\nu = 10^{-4}$, and $H = 5$. In figure 6.4, as μ_r decreases, both $b_{\text{eff}\parallel}$ and $b_{\text{eff}\perp}$ approach Philip's limit value assuming a shear-free boundary condition $\mu_r = 0$. The b_{eff} in both, [35] and [61], decrease as μ_r increases, indicating less drag reduction. The solution obtained in this chapter considers one additional parameter: the location of the interface h. Note that h does not change the trend of the slip length but its magnitude diminishes when the interface moves down and eventually approaches a fully-wetted solution $\mu_r = 1$. All solutions intersect at the fully-wetted solution, indicating that the effective slip length does not change both fluids have the same viscosity. When a small amount of penetration is considered, the data show good comparison to the simulation data of [61] at $\mu_r < 1$.

6.4 Results and discussion

6.4.1 Instantaneous flow field

When the grooves are parallel to the flow direction, the streamwise velocity changes monotonically along the wall normal direction. When the grooves are transverse to the flow direction, the flow field inside the grooves behaves similarly to a lid-driven cavity flow. Figure 6.5 shows the instantaneous streamlines inside the grooves of different depths b with different penetration rates $1 - h/b$. The external oscillatory boundary condition are all applied at the same $H = 5.40$. The penetration rate represents the area fraction of fluid A inside the groove to the area of the groove $(w(b - h)/wb)$. On one hand, as the groove becomes deeper, multiple vortices form inside, which is similar to the eddy structure in lid-driven cavities with increasing height [123]. On the other hand, fluid B in the blue shaded area generates vortices separately from fluid A (white area).

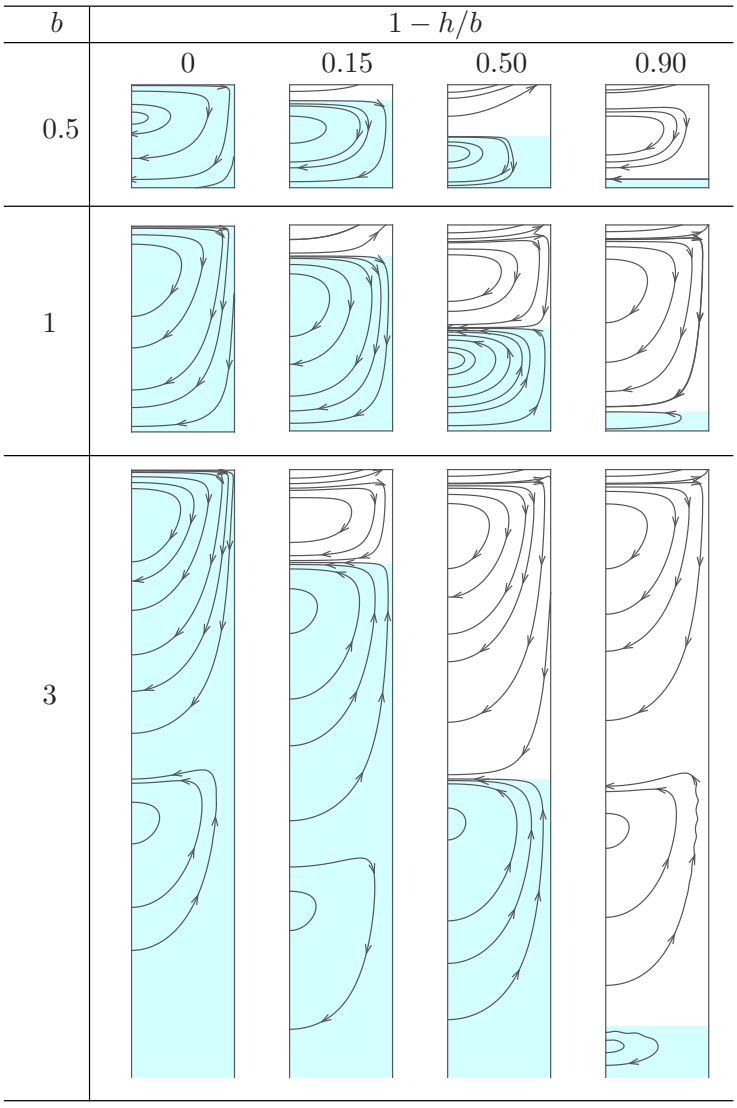

Figure 6.5: Instantaneous streamlines inside the grooves of different depths b with different penetration rates $1 - h/b$ at $t = \frac{2k\pi}{\omega}$, k is an integer. The blue area represents fluid B of $\mu_r = 0.02$. The coverage ratio of the groove is $\phi = 0.5$. $L^2\omega/\nu = 0.3428$.

H	Penetration rate	$\frac{L^2\omega}{\nu}$	μ_r	Re_τ
5.40	0, 0.15, 0.5, 0.9	$0.04 - 4.23$	0.02, 0.37, 30.00	180
2.43	0, 0.15, 0.5, 0.9	$0.04 - 4.23$	0.02, 0.37, 30.00	400
1.65	0, 0.15, 0.5, 0.9	$0.04 - 4.23$	0.02, 0.37, 30.00	590

Table 6.3: Location of the forcing H, the penetration rate $1 - h/b$, the relevant non-dimensional number $\frac{L^2\omega}{\nu}$, the viscosity ratio μ_r for all cases solved from analytical solution, and the applicable Re_τ. For all cases, $L = 18/3500$ is considered.

6.4.2 Parametric study

The effect of frequency, domain height, penetration rate, and viscosity ratio are studied using the analytic solution. All the following cases have a coverage ratio of $a = 0.875$ otherwise stated. The parameters for each case are listed in table 6.3. The frequency range is selected such that it is representative of a turbulent channel flow at a given Re_τ listed in the last column. The location of the forcing H is equivalent to $y^+ = 5$ for the Re_τ given. The viscosity ratios are chosen to be 0.02, 0.37, 30.00 to represent air, heptane, and Dupont Krytox with respect to water respectively [48].

The transfer function of the cases from table 6.3 are shown in figure 6.6(a-c). The transfer function $\mathcal{H}\left(\frac{iL^2\omega}{\nu}\right)$ is defined as the ratio between the energy at $y = 0$ and the energy of the forcing at $y = H$:

$$\mathcal{H}\left(\frac{L^2\omega}{\nu}\right) = \sqrt{\frac{\Phi(\frac{iL^2\omega}{\nu})|_{y=0}}{\Phi(\frac{iL^2\omega}{\nu})|_{y=H}}}. \tag{6.65}$$

Overall, as the oscillating frequency increases, it becomes harder for the forcing energy to penetrate into the grooved surface. As the representative Reynolds number increases, the transfer function increases. However, note that as Reynolds number increases, the forcing fluctuations would also be nearer to the surface. The shaded areas correspond to the condition $\mathcal{H}(L^2\omega/\nu, \mu_r \geq 1)$ to distinguish between high viscosity fluid and low viscosity fluid inside the groove. Note that the trend of $\mathcal{H}$ with penetration rate is different between shaded and non-shaded regions. When $\mu_r > 1$, as the penetration rate increases, $\mathcal{H}$ increases, and the penetration of the external fluid

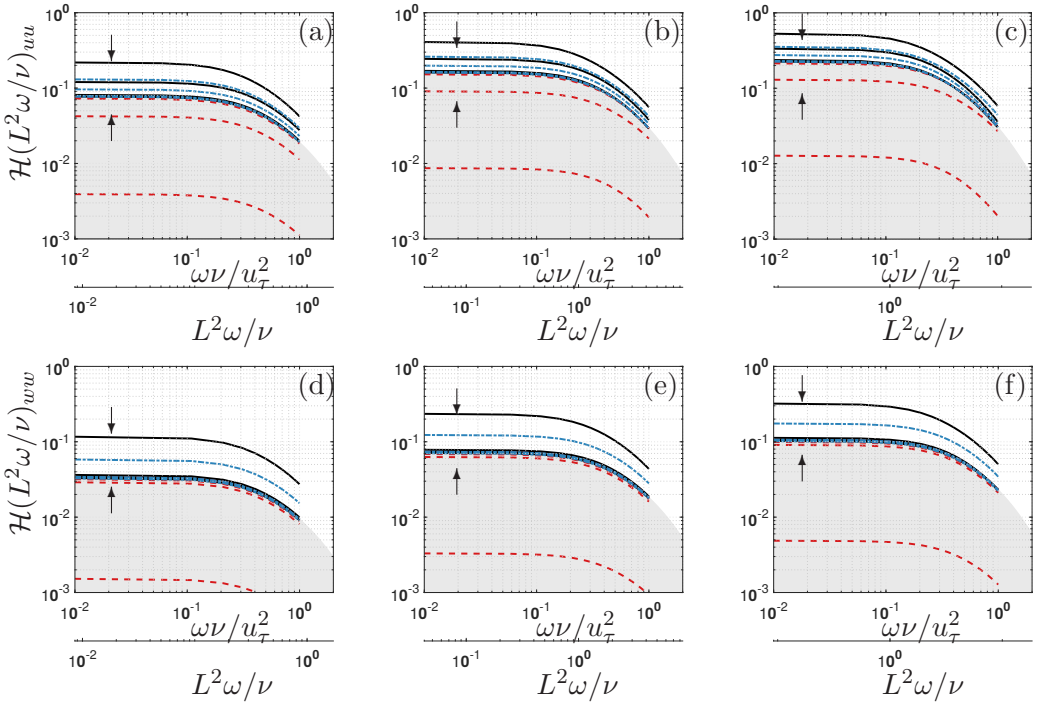

Figure 6.6: Transfer function $\mathcal{H}(L^2\omega/\nu)$ in longitudinal flow (top row) and transverse flow (bottom row) with increasing frequencies of the forcing normalized by viscous units u_τ^2/ν (top axis) or Womersley number $L^2\omega/\nu$ (bottom axis) with increasing representative (a) and (d) $Re_\tau = 180$, (b) and (e) $Re_\tau = 400$, (c) and (f) $Re_\tau = 590$. Here, $\mu_r = 0.02,\ 0.37,\ 30.00$ are denoted by black solid lines, blue dashed-dotted lines, and red dashed lines respectively. The shaded area represents $\mathcal{H}(L^2\omega/\nu, \mu_r \geq 1)$. The arrows indicate increasing penetration rate in the area of $\mu_r \geq 1$ or $\mu_r < 1$ respectively.

improves the transfer of forcing energy. Conversely, when $\mu_r < 1$, as the penetration rate increases, $\mathcal{H}$ decreases, and the penetration of the external fluid suppresses the transfer of the forcing energy. However, neither of these two conditions cross the border between the $\mu_r = 1$ curve. Also, air performs the best over the other two fluids, which is intuitively reasonable, considering that the interface does not break or drain based on the assumption made in this paper. Transverse flow (figure 6.6 d-f) behaves the same way as longitudinal flow.

The root-mean-square (rms) of the unsteady analytical effective slip length is determined by:

$$b_{\text{eff}\parallel} = \frac{\int_0^1 u(0,z)_{\text{rms}} dz}{\int_0^1 \frac{\partial u(\infty,z)}{\partial y}_{\text{rms}} dz} = \frac{\Re\left((B_0 + C_0)\exp(it)\right)_{\text{rms}}}{1/\sqrt{2}}, \tag{6.66}$$

for longitudinal flow; and

$$b_{\text{eff}\perp} = \frac{\int_0^1 w(0,z)_{\text{rms}} dz}{\int_0^1 \frac{\partial w(\infty,z)}{\partial y}_{\text{rms}} dz} = \frac{\Re\left(\sqrt{\frac{iL^2\omega}{\nu}}(E_0 - F_0)\exp(it)\right)_{\text{rms}}}{1/\sqrt{2}}. \tag{6.67}$$

for transverse flow [46, 124], where $\int_0^1 \frac{\partial u_{\text{II}}}{\partial y}(\infty, z)\mathrm{d}z = 1$. In viscous units, $b_0^+ = b_{\text{eff}} L u_\tau/\nu$, where u_τ is the friction velocity. The unsteady effective slip length is plotted in figure 6.7(a-c) for longitudinal flow and figure 6.7(d-f) for transverse flow. Zero penetration of the external fluid with air pockets provides the highest slip length. b_{eff} is relatively independent of the frequencies. Transverse effective slip length is more sensitive to the penetration of the external fluid: a 15% penetration would result in an effective slip length overlapping with the fully-wetted grooved cases.

Comparing the longitudinal effective slip length to the transverse values in figure 6.8 using the ratio $b_{\text{eff}\parallel}/b_{\text{eff}\perp}$, it is found that the effective slip length for longitudinal flows is more than 1.5 times of that of transverse flows with the same coverage ratio. The ratio drops at high frequencies. For the combination of zero penetration and air-water interface, $b_{\text{eff}\parallel}/b_{\text{eff}\perp} = 2$ at low frequencies. This agrees with the finding in [34] where no-shear strips in steady pipe flow were considered. Large penetration rate results in large ratio.

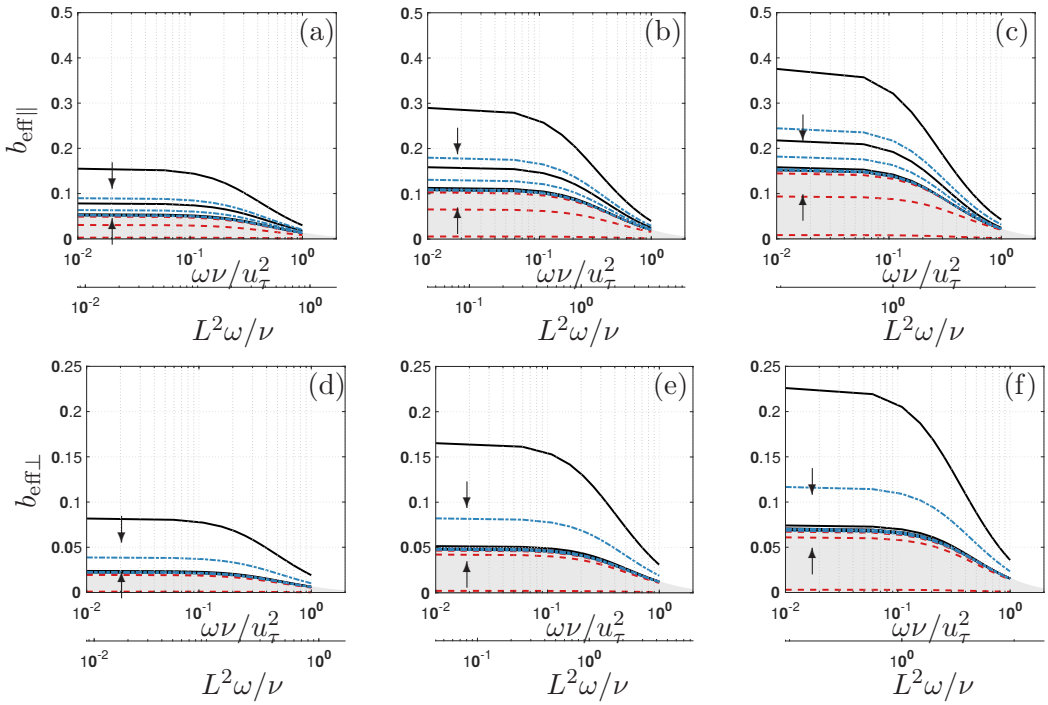

Figure 6.7: Effective slip length $b_{\mathrm{eff}\parallel}$ (top row) and $b_{\mathrm{eff}\perp}$ (bottom row) with increasing frequencies of the forcing normalized by viscous units u_τ^2/ν (top axis) or Womersley number $L^2\omega/\nu$ (bottom axis) with increasing representative (a) and (d) $Re_\tau = 180$, (b) and (e) $Re_\tau = 400$, (c) and (f) $Re_\tau = 590$. Here, $\mu_r = 0.02,\ 0.37,\ 30.00$ are denoted by black solid lines, blue dashed-dotted lines, and red dashed lines respectively. The shaded area represents $b_{\mathrm{eff}}(L^2\omega/\nu, \mu_r \geq 1)$. The arrows indicate increasing penetration rate in the area of $\mu_r \geq 1$ or $\mu_r < 1$ respectively.

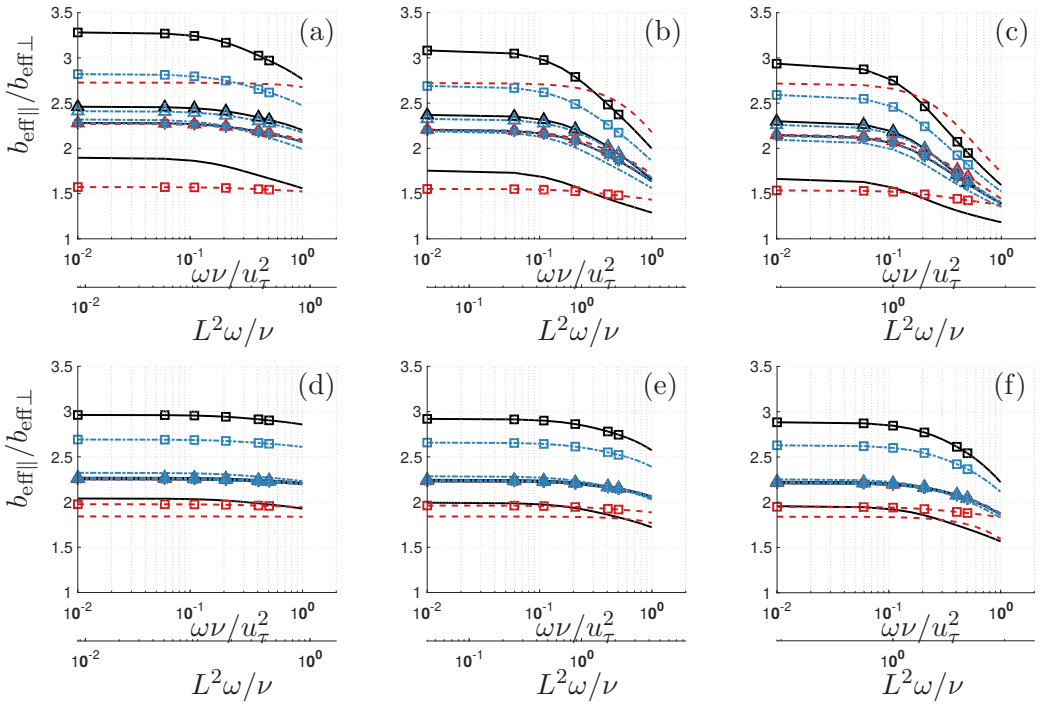

Figure 6.8: $b_{\text{eff}\parallel}/b_{\text{eff}\perp}$ with increasing frequencies of the forcing normalized by viscous units u_τ^2/ν (top axis) or Womersley number $L^2\omega/\nu$ (bottom axis) with increasing representative (a) and (d) $Re_\tau = 180$, (b) and (e) $Re_\tau = 400$, (c) and (f) $Re_\tau = 590$. Top row: $a = 0.875$; bottom row: $a = 0.5$. Here, $\mu_r = 0.02,\ 0.37,\ 30.00$ are denoted by black solid lines, blue dashed-dotted lines, and red dashed lines respectively. Penetration rate of 0, 0.15, 0.5, 0.9 is denoted by lines, $\square$, $\triangle$, $*$ respectively. The symbols differentiate lines and do not reflect actual data points.

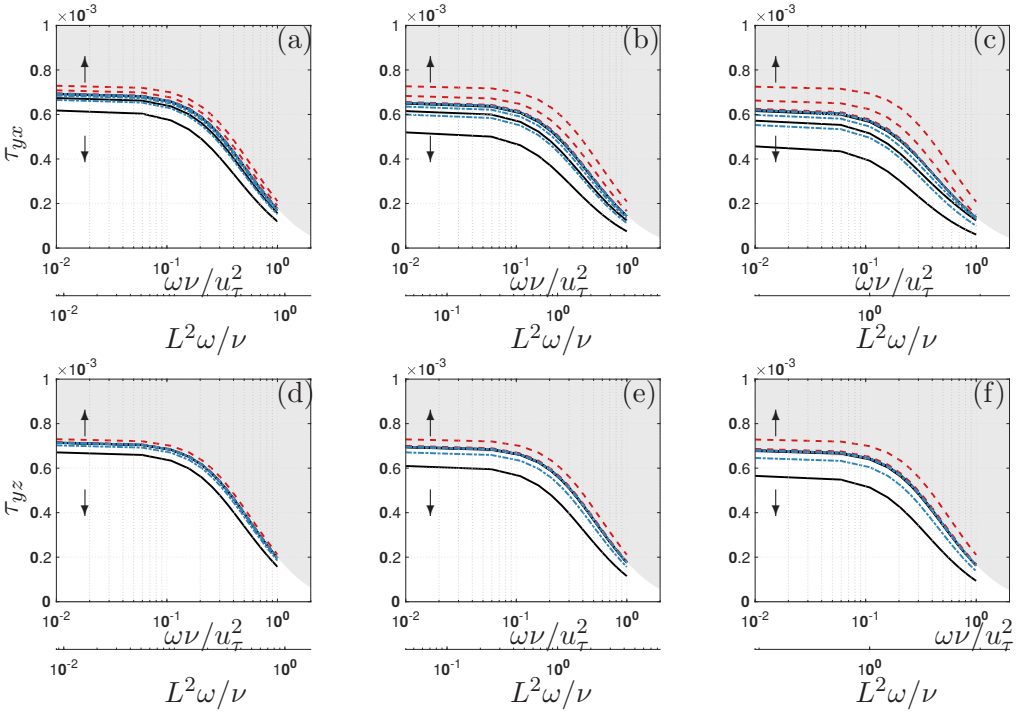

Figure 6.9: Shear stress τ_{yx} in longitudinal flow (top row) and τ_{yz} in transverse flow (bottom row) with increasing frequencies of the forcing normalized by viscous units u_τ^2/ν (top axis) or Womersley number $L^2\omega/\nu$ (bottom axis) with increasing representative (a) and (d) $Re_\tau = 180$, (b) and (e) $Re_\tau = 400$, (c) and (f) $Re_\tau = 590$. Here, $\mu_r = 0.02,\ 0.37,\ 30.00$ are denoted by black solid lines, blue dashed-dotted lines, and red dashed lines respectively. The shaded area represents $\tau(L^2\omega/\nu, \mu_r \geq 1)$. The arrows indicate increasing penetration rate in the area of $\mu_r \geq 1$ or $\mu_r < 1$ respectively.

The shear stress at the plane $y = 0$ is evaluated by

$$\tau_{yx} = \mu_1 \Re \left(\sqrt{\frac{iL^2\omega}{\nu}} (B_0 - C_0) \exp(it) \right)_{\text{rms}}, \tag{6.68}$$

for longitudinal flows, and

$$\tau_{yz} = \mu_1 \Re \left(\frac{iL^2\omega}{\nu} (E_0 + F_0) \exp(it) \right)_{\text{rms}}. \tag{6.69}$$

for transverse flows. Figure 6.9 shows the shear stress varying across the frequency range. Again, the combination of zero penetration and air pocket produces the least shear stress for both longitudinal and transverse flows. The effect of penetration of the external fluid has a larger impact on transverse flow than longitudinal flow. The trend observed in shear stress is consistent with those found in transfer function and effective slip length. As the frequency increases, the shear stress decreases, because the flow near the grooved surface is approaching a stationary state.

6.5 Summary

Analytical solutions of the multiphase Stokes flow generated by oscillatory velocity at a finite-height over a grooved surface have been derived. In the steady limit, the analytical results agree well with the steady solution of [35] and [61]. Numerical simulations using the VOF methodology were performed to validate the unsteady multiphase analytical solution. The analytical solution compares well with the DNS data. A transfer function based on the energy of the oscillatory velocity and the energy inside the grooved surface was obtained. The analytical solution was parameterized by $\omega L^2/\nu$, a representative Reynolds number Re_τ, and location of the multiphase interface h/b. We see that: (i) large values of $\omega L^2/\nu$ lower the transfer function, (ii) increasing Re_τ decreases the forcing height and therefore increases the transfer function, and (iii) When $\mu_r < 1$, penetration of the external fluid suppresses the transfer function; when $\mu_r > 1$, penetration of the external fluid increases it.

Bibliography

[1] A. B. D. Cassie and S. Baxter. Wettability of porous surfaces. *Transactions of the Faraday Society*, 40:546–551, 1944.

[2] R. S. Voronov, D. V. Papavassiliou, and L. L. Lee. Review of fluid slip over superhydrophobic surfaces and its dependence on the contact angle. *Industrial & Engineering Chemistry Research*, 47(8):2455–2477, 2008.

[3] D. Quéré. Wetting and roughness. *Annual Review of Materials Research*, 38: 71–99, 2008.

[4] J. P. Rothstein. Slip on superhydrophobic surfaces. *Annual Review of Fluid Mechanics*, 42(1):89–109, 2010.

[5] K. B. Golovin, J. W. Gose, M. Perlin, S. L. Ceccio, and A. Tuteja. Bioinspired surfaces for turbulent drag reduction. *Philosophical Transactions of the Royal Society A*, 374(2073), 2016.

[6] C. Henoch, T. Krupenkin, P. Kolodner, J. Taylor, M. Hodes, A. Lyons, C. Peguero, and K. Breuer. Turbulent drag reduction using superhydrophobic surfaces. In *3rd AIAA Flow Control Conference*, page 3192, 2006.

[7] B. Woolford, J. Prince, D. Maynes, and B. W. Webb. Particle image velocimetry characterization of turbulent channel flow with rib patterned superhydrophobic walls. *Physics of Fluids*, 21(8):085106, 2009.

[8] R. J. Daniello, N. E. Waterhouse, and J. P. Rothstein. Drag reduction in turbulent flows over superhydrophobic surfaces. *Physics of Fluids*, 21(8):085103, 2009.

[9] H. Park, G. Sun, and C. J. Kim. Superhydrophobic turbulent drag reduction as a function of surface grating parameters. *Journal of Fluid Mechanics*, 747:722–734, 2014.

[10] J. Zhang, Z. Yao, and P. Hao. Drag reductions and the air-water interface stability of superhydrophobic surfaces in rectangular channel flow. *Physical Review E*, 94 (5):053117, 2016.

[11] K. K. S. Lau, J. Bico, K. B. K. Teo, M. Chhowalla, G. A. J. Amaratunga, W. I. Milne, G. H. McKinley, and K. K. Gleason. Superhydrophobic carbon nanotube forests. *Nano Letters*, 3(12):1701–1705, 2003.

[12] L. Zhu, P. Shi, J. Xue, Y. Wang, Q. Chen, J. Ding, and Q. Wang. Superhydrophobic stability of nanotube array surfaces under impact and static forces. *ACS Applied Materials and Interfaces*, 6(11):8073–8079, 2014.

[13] H. Tian, J. Zhang, E. Wang, Z. Yao, and N. Jiang. Experimental investigation on drag reduction in turbulent boundary layer over superhydrophobic surface by TRPIV. *Theoretical and Applied Mechanics Letters*, 5(1):45–49, 2015.

[14] E. Aljallis, M. A. Sarshar, R. Datla, V. Sikka, A. Jones, and C.-H. Choi. Experimental study of skin friction drag reduction on superhydrophobic flat plates in high Reynolds number boundary layer flow. *Physics of Fluids*, 25(2):025103, 2013.

[15] R. A. Bidkar, L. Leblanc, A. J. Kulkarni, V. Bahadur, S. L. Ceccio, and M. Perlin. Skin-friction drag reduction in the turbulent regime using random-textured hydrophobic surfaces. *Physics of Fluids*, 26(8):085108, 2014.

[16] H. Haibao, D. Peng, Z. Feng, S. Dong, and W. Yang. Effect of hydrophobicity on turbulent boundary layer under water. *Experimental Thermal and Fluid Science*, 60:148–156, 2015.

[17] S. Srinivasan, J. A. Kleingartner, J. B. Gilbert, R. E. Cohen, A. J. B. Milne, and G. H. McKinley. Sustainable drag reduction in turbulent Taylor-Couette flows by depositing sprayable superhydrophobic surfaces. *Physical Review Letters*, 114(1): 2–6, 2015.

[18] H. Ling, S. Srinivasan, K. Golovin, G. H. Mckinley, A. Tuteja, and J. Katz. High-resolution velocity measurement in the inner part of turbulent boundary layers over super-hydrophobic surfaces. *Journal of Fluid Mechanics*, 801:670–703, 2016.

[19] T. Min and J. Kim. Effects of hydrophobic surface on skin-friction drag. *Physics of Fluids*, 16(7):L55–L58, 2004.

[20] K. Fukagata, N. Kasagi, and P. Koumoutsakos. A theoretical prediction of friction drag reduction in turbulent flow by superhydrophobic surfaces. *Physics of Fluids*, 18(5):051703, 2006.

[21] M. B. Martell, J. B. Perot, and J. P. Rothstein. Direct numerical simulations of turbulent flows over superhydrophobic surfaces. *Journal of Fluid Mechanics*, 620: 31–41, 2009.

[22] M. B. Martell, J. P. Rothstein, and J. B. Perot. An analysis of superhydrophobic turbulent drag reduction mechanisms using direct numerical simulation. *Physics of Fluids*, 22(6):065102, 2010.

[23] A. Busse and N. D. Sandham. Influence of an anisotropic slip-length boundary condition on turbulent channel flow. *Physics of Fluids*, 24(5):055111, 2012.

[24] H. Park, H. Park, and J. Kim. A numerical study of the effects of superhydrophobic surface on skin-friction drag in turbulent channel flow. *Physics of Fluids*, 25 (11):110815, 2013.

[25] T. O. Jelly, S. Y. Jung, and T. A. Zaki. Turbulence and skin friction modification in channel flow with streamwise-aligned superhydrophobic surface texture. *Physics of Fluids*, 26(9):095102, 2014.

[26] S. Türk, G. Daschiel, A. Stroh, Y. Hasegawa, and B. Frohnapfel. Turbulent flow over superhydrophobic surfaces with streamwise grooves. *Journal of Fluid Mechanics*, 747:186–217, 2014.

[27] J. Seo, R. García-Mayoral, and A. Mani. Pressure fluctuations and interfacial robustness in turbulent flows over superhydrophobic surfaces. *Journal of Fluid Mechanics*, 783:448–473, 2015.

[28] J. Seo and A. Mani. On the scaling of the slip velocity in turbulent flows over superhydrophobic surfaces. *Physics of Fluids*, 28(2):025110, 2016.

[29] T. Jung, H. Choi, and J. Kim. Effects of the air layer of an idealized superhydrophobic surface on the slip length and skin-friction drag. *Journal of Fluid Mechanics*, 790:R1, 2016.

[30] M. A. Samaha, H. V. Tafreshi, and M. Gad-el Hak. Modeling drag reduction and meniscus stability of superhydrophobic surfaces comprised of random roughness. *Physics of Fluids*, 23(1):012001, 2011.

[31] A. Rastegari and R. Akhavan. On the mechanism of turbulent drag reduction with super-hydrophobic surfaces. *Journal of Fluid Mechanics*, 773:R4, 2015.

[32] J. R. Philip. Flows satisfying mixed no-slip and no-shear conditions. *Zeitschrift fr angewandte Mathematik und Physik ZAMP*, 23(3):353–372, 1972.

[33] J. R. Philip. Integral properties of flows satisfying mixed no-slip and no-shear conditions. *Zeitschrift fr angewandte Mathematik und Physik ZAMP*, 23(6):960–968, 1972.

[34] E. Lauga and H. A. Stone. Effective slip in pressure-driven stokes flow. *Journal of Fluid Mechanics*, 489:55–77, 2003.

[35] C. Schönecker, T. Baier, and S. Hardt. Influence of the enclosed fluid on the flow over a microstructured surface in the cassie state. *Journal of Fluid Mechanics*, 740:168–195, 2014.

[36] A. V. Belyaev and O. I. Vinogradova. Effective slip in pressure-driven flow past super-hydrophobic stripes. *Journal of Fluid Mechanics*, 652:489–499, 2010.

[37] O. I. Vinogradova. Drainage of a thin liquid film confined between hydrophobic surfaces. *Langmuir*, 11(6):2213–2220, 1995.

[38] T. V. Nizkaya, E. S. Asmolov, and O. I. Vinogradova. Gas cushion model and hydrodynamic boundary conditions for superhydrophobic textures. *Physical Review E*, 90(4):043017, 2014.

[39] A. Busse, N. D. Sandham, G. McHale, and M. I. Newton. Change in drag, apparent slip and optimum air layer thickness for laminar flow over an idealised superhydrophobic surface. *Journal of Fluid Mechanics*, 727:488–508, 2013.

[40] D. Maynes, K. Jeffs, B. Woolford, and B. W. Webb. Laminar flow in a microchannel with hydrophobic surface patterned microribs oriented parallel to the flow direction. *Physics of Fluids*, 19(9):093603, 2007.

[41] C. Cottin-Bizonne, J. L. Barrat, L. Bocquet, and É. Charlaix. Low-friction flows of liquid at nanopatterned interfaces. *Nature Materials*, 2(4):237–240, 2003.

[42] M. Sbragaglia and A. Prosperetti. A note on the effective slip properties for microchannel flows with ultrahydrophobic surfaces. *Physics of Fluids*, 19(4):043603, 2007.

[43] L. P. Wang, C. J. Teo, and B. C. Khoo. Effects of interface deformation on flow through microtubes containing superhydrophobic surfaces with longitudinal ribs and grooves. *Microfluidics and nanofluidics*, 16(1-2):225–236, 2014.

[44] D. G. Crowdy. Analytical formulae for longitudinal slip lengths over unidirectional superhydrophobic surfaces with curved menisci. *Journal of Fluid Mechanics*, 791: R7, 2016.

[45] A. M. J. Davis and E. Lauga. Geometric transition in friction for flow over a bubble mattress. *Physics of Fluids*, 21(1):011701, 2009.

[46] C. Cottin-Bizonne, C. Barentin, É. Charlaix, L. Bocquet, and J. L. Barrat. Dynamics of simple liquids at heterogeneous surfaces: Molecular-dynamics simulations and hydrodynamic description. *The European Physical Journal E*, 15(4): 427–438, 2004.

[47] T. Biben and L. Joly. Wetting on nanorough surfaces. *Physical Review Letters*, 100(18):186103, 2008.

[48] B. J. Rosenberg, T. Van Buren, M. K. Fu, and A. J. Smits. Turbulent drag reduction over air- and liquid- impregnated surfaces. *Physics of Fluids*, 28(1): 015103, 2016.

[49] Y. Liu, J. S. Wexler, C. Schönecker, and H. A. Stone. Effect of viscosity ratio on the shear-driven failure of liquid-infused surfaces. *Physical Review Fluids*, 1(7): 074003, 2016.

[50] Y. Li, K. Alame, and K. Mahesh. Feature resolved simulations of turbulence over superhydrophobic surfaces. In *Proceedings of the 31st Symposium on Naval Hydrodynamics*, Monterey, USA, 2016.

[51] M. Reyssat, J. M. Yeomans, and D. Quéré. Impalement of fakir drops. *Europhysics Letters*, 81(2):26006, 2007.

[52] A. L. Dubov, K. Perez-Toralla, A. Letailleur, E. Barthel, and J. Teisseire. Superhydrophobic silica surfaces: fabrication and stability. *Journal of Micromechanics and Microengineering*, 23(12):125013, 2013.

[53] C. W. Extrand. Criteria for ultralyophobic surfaces. *Langmuir*, 20(12):5013–5018, 2004.

[54] Q.-S. Zheng, Y. Yu, and Z.-H. Zhao. Effects of hydraulic pressure on the stability and transition of wetting modes of superhydrophobic surfaces. *Langmuir*, 21(26): 12207–12212, 2005.

[55] C. Lee, C.-H. Choi, and C. J. Kim. Structured surfaces for a giant liquid slip. *Physical Review Letters*, 101(6):064501, 2008.

[56] K. Kamrin, M. Z. Bazant, and H. A. Stone. Effective slip boundary conditions for arbitrary periodic surfaces: the surface mobility tensor. *Journal of Fluid Mechanics*, 658:409–437, 2010.

[57] C. Y. Wang. Flow over a surface with parallel grooves. *Physics of Fluids*, 15(5): 1114–1121, 2003.

[58] C.-O. Ng and C. Y. Wang. Stokes shear flow over a grating: implications for superhydrophobic slip. *Physics of Fluids*, 21(1):013602, 2009.

[59] D. Crowdy. Slip length for longitudinal shear flow over a dilute periodic mattress of protruding bubbles. *Physics of Fluids*, 22(12):121703, 2010.

[60] O. Schnitzer. Slip length for longitudinal shear flow over an arbitrary-protrusion-angle bubble mattress: the small-solid-fraction singularity. *Journal of Fluid Mechanics*, 820:580–603, 2017.

[61] M. K. Fu, I. Arenas, S. Leonardi, and M. Hultmark. Liquid-infused surfaces as a passive method of turbulent drag reduction. *Journal of Fluid Mechanics*, 824: 688–700, 2017.

[62] T. Van Buren and A. J. Smits. Substantial drag reduction in turbulent flow using liquid-infused surfaces. *Journal of Fluid Mechanics*, 827:448–456, 2017.

[63] A. Keiser, L. Keiser, C. Clanet, and David Quéré. Drop friction on liquid-infused materials. *Soft Matter*, pages 6981–6987, 2017.

[64] C. Schönecker and S. Hardt. Longitudinal and transverse flow over a cavity containing a second immiscible fluid. *Journal of Fluid Mechanics*, 717:376–394, 2013.

[65] D. G. Crowdy. Perturbation analysis of subphase gas and meniscus curvature effects for longitudinal flows over superhydrophobic surfaces. *Journal of Fluid Mechanics*, 822:307–326, 2017.

[66] Y. Li, K. Alame, and K. Mahesh. Feature-resolved computational and analytical study of laminar drag reduction by superhydrophobic surfaces. *Physical Review Fluids*, 2:054002, 2017.

[67] C.-O. Ng, H. C. W. Chu, and C. Y. Wang. On the effects of liquid-gas interfacial shear on slip flow through a parallel-plate channel with superhydrophobic grooved walls. *Physics of Fluids*, 22(10):102002, 2010.

[68] C. J. Teo and B. C. Khoo. Analysis of stokes flow in microchannels with superhydrophobic surfaces containing a periodic array of micro-grooves. *Microfluidics Nanofluidics*, 7(3):353–382, 2009.

[69] M. J. Walsh. Riblets as a viscous drag reduction technique. *AIAA journal*, 21(4): 485–486, 1983.

[70] H. Choi, P. Moin, and J. Kim. Direct numerical simulation of turbulent flow over riblets. *Journal of Fluid Mechanics*, 255:503–539, 1993.

[71] D. C. Chu and G. E. Karniadakis. A direct numerical simulation of laminar and turbulent flow over riblet-mounted surfaces. *Journal of Fluid Mechanics*, 250: 1–42, 1993.

[72] D. Goldstein, R. Handler, and L. Sirovich. Direct numerical simulation of turbulent flow over a modeled riblet covered surface. *Journal of Fluid Mechanics*, 302: 333–376, 1995.

[73] R. García-Mayoral and J. Jiménez. Drag reduction by riblets. *Philosophical Transactions of the Royal Society of London A: Mathematical, Physical and Engineering Sciences*, 369(1940):1412–1427, 2011.

[74] J. Jiménez. Turbulent flows over rough walls. *Annual Review of Fluid Mechanics*, 36(1):173–196, 2004.

[75] M. Gad-el Hak. Comment on "Experimental study of skin friction drag reduction

on superhydrophobic flat plates in high Reynolds number boundary layer flow". *Physics of Fluids*, 25(7):079101, 2013.

[76] B. Vajdi Hokmabad and S. Ghaemi. Turbulent flow over wetted and non-wetted superhydrophobic counterparts with random structure. *Physics of Fluids*, 28(1): 015112, 2016.

[77] P. Luchini, F. Manzo, and A. Pozzi. Resistance of a grooved surface to parallel flow and cross-flow. *Journal of Fluid Mechanics*, 228:87–109, 1991.

[78] C.-O. Ng. Effective slip for stokes flow between two grooved walls with an arbitrary phase shift. *Fluid Dynamics Research*, 49:025516, 2017.

[79] E. Larrieu, E. J. Hinch, and F. Charru. Lagrangian drift near a wavy boundary in a viscous oscillating flow. *Journal of Fluid Mechanics*, 630:391–411, 2009.

[80] H. Schlichting and K. Gersten. *Boundary-layer theory*. Springer, 9th edition, 2017.

[81] W. J. Jung, N. Mangiavacchi, and R. Akhavan. Suppression of turbulence in wall-bounded flows by high-frequency spanwise oscillations. *Physics of Fluids A-Fluid*, 4(8):1605–1607, 1992.

[82] C. Viotti, M. Quadrio, and P. Luchini. Streamwise oscillation of spanwise velocity at the wall of a channel for turbulent drag reduction. *Physics of Fluids*, 21(11): 115109, 2009.

[83] K. Mahesh, G. Constantinescu, and P. Moin. A numerical method for large-eddy simulation in complex geometries. *Journal of Computational Physics*, 197(1):215–240, 2004.

[84] S. Muppidi and K. Mahesh. Study of trajectories of jets in crossflow using direct numerical simulations. *Journal of Fluid Mechanics*, 530:81–100, 2005.

[85] S. Muppidi and K. Mahesh. Direct numerical simulation of round turbulent jets in crossflow. *Journal of Fluid Mechanics*, 574:59–84, 2007.

[86] S. Muppidi and K. Mahesh. Direct numerical simulation of passive scalar transport in transverse jets. *Journal of Fluid Mechanics*, 598:335–360, 2008.

[87] R. Sau and K. Mahesh. Passive scalar mixing in vortex rings. *Journal of Fluid Mechanics*, 582:449–461, 2007.

[88] R. Sau and K. Mahesh. Dynamics and mixing of vortex rings in crossflow. *Journal of Fluid Mechanics*, 604:389–409, 2008.

[89] R. Sau and K. Mahesh. Optimization of pulsed jets in crossflow. *Journal of Fluid Mechanics*, 653:365–390, 2010.

[90] X. Chai and K. Mahesh. Dynamic–equation model for large-eddy simulation of compressible flows. *Journal of Fluid Mechanics*, 699:385–413, 2012.

[91] X. Chai, P. S. Iyer, and K. Mahesh. Numerical study of high speed jets in crossflow. *Journal of Fluid Mechanics*, 785:152–188, 2015.

[92] P. S. Iyer and K. Mahesh. A numerical study of shear layer characteristics of low-speed transverse jets. *Journal of Fluid Mechanics*, 790:275–307, 2016.

[93] M. A. Regan and K. Mahesh. Global linear stability analysis of jets in cross-flow. *Journal of Fluid Mechanics*, 828:812–836, 2017.

[94] P. A. Chang, A. Vargas, D. Lummer, M. Jiang, and K. Mahesh. Fully-resolved LES of weakly separated flows. In *20th AIAA Computational Fluid Dynamics Conference*. AIAA, 2011.

[95] K. Mahesh, P. Kumar, A. Gnanaskandan, and Z. Nitzkorski. LES applied to ship research. *Journal of Ship Research*, 59(4):238–245, 2015.

[96] P. Kumar and K. Mahesh. Large-eddy simulation of flow over an axisymmetric body of revolution. *Journal of Fluid Mechanics*, 853:537–563, 2018.

[97] P. Chang, M. Ebert, Y. L. Young, Z. Liu, K. Mahesh, H. Jang, and M. Shearer. Propeller forces and structural responses to crashback. In *Proceedings of the 27$^{\text{th}}$ Symposium on Naval Hydrodynamics, Seoul, Korea*, 2008.

[98] H. Jang and K. Mahesh. Large eddy simulation of ducted propulsors in crashback. In *Proceedings of the 27th Symposium on Naval Hydrodynamics, Seoul Korea*, 2008.

[99] H. Jang and K. Mahesh. Large eddy simulation of crashback in ducted propulsors with stator blades. In *Proceedings of the 29th Symposium on Naval Hydrodynamics, Gothenburg, Sweden*, 2012.

[100] H. Jang and K. Mahesh. Large eddy simulation of flow around a reverse rotating propeller. *Journal of Fluid Mechanics*, 729:151–179, 2013.

[101] A. Verma, H. Jang, and K. Mahesh. The effect of an upstream hull on a propeller in reverse rotation. *Journal of Fluid Mechanics*, 704:61–88, 2012.

[102] H. Jang, A. Verma, and K. Mahesh. Predicting unsteady loads in marine propulsor crashback using large eddy simulation. *International Journal of Rotating Machinery*, 2012.

[103] H. Jang. *Large eddy simulation of Crashback in marine propulsors*. PhD thesis, University of Minnesota, 2011.

[104] P. Kumar and K. Mahesh. Analysis of marine propulsor in crashback using large eddy simulation. In *Fourth International Symposium on Marine Propulsors, Austin, USA*, 2015.

[105] K. Alame and K. Mahesh. Wall-bounded flow over a realistically rough superhydrophobic surface. *arXiv preprint arXiv:1802.06845*, 2018.

[106] F. H. Harlow and J. E. Welch. Numerical calculation of time-dependent viscous incompressible flow of fluid with free-stream. *Physics of Fluids*, 8:2182–2189, 1965.

[107] URL https://computation.llnl.gov/casc/hypre/software.html.

[108] K. Alame and K. Mahesh. private communication, 2016.

[109] C. H. Choi and C. J. Kim. Large slip of aqueous liquid flow over a nanoengineered superhydrophobic surface. *Physical Review Letters*, 96:066001, 2006.

[110] S. Richardson. A model for the boundary condition of a porous material. part 2. *Journal of Fluid Mechanics*, 49:327–336, 1971.

[111] C. Ybert, C. Barentin, C. Cottin-Bizonne, P. Joseph, and L. Bocquet. Achieving large slip with superhydrophobic surfaces: Scaling laws for generic geometries. *Physics of Fluids*, 19(12):123601, 2007.

[112] B. Emami, H. V. Tafreshi, M. Gad-el Hak, and G. C. Tepper. Predicting shape and stability of air-water interface on superhydrophobic surfaces with randomly distributed, dissimilar posts. *Applied Physics Letters*, 98(20):203106–203106, 2011.

[113] R. D. Moser, J. Kim, and N. N. Mansour. Direct numerical simulation of turbulent channel flow up to $Re_\tau = 590$. *Physics of Fluids*, 11(4):943–945, 1999.

[114] A. S. Thom. Momentum absorption by vegetation. *Quarterly Journal of the Royal Meteorological Society*, 97(414):414–428, 1971.

[115] L. Chan, M. Macdonald, D. Chung, N. Hutchins, and A. Ooi. A systematic investigation of roughness height and wavelength in turbulent pipe flow in the transitionally rough regime. *Journal of Fluid Mechanics*, 771(1):743–777, 2015.

[116] W. P. Breugem, B. J. Boersma, and R. E. Uittenbogaard. The influence of wall permeability on turbulent channel flow. *Journal of Fluid Mechanics*, 562:35–72, 2006.

[117] R. García-Mayoral and J. Jiménez. Hydrodynamic stability and breakdown of the viscous regime over riblets. *Journal of Fluid Mechanics*, 678:317–347, 2011.

[118] K. A. Flack, M. P. Schultz, and T. A. Shapiro. Experimental support for Townsends Reynolds number similarity hypothesis on rough walls. *Physics of Fluids*, 17(3):035102, 2005.

[119] A. A. Townsend. *The structure of turbulent shear flow*. Cambridge University Press, 1980.

[120] S. Hahn, J. Je, and H. Choi. Direct numerical simulation of turbulent channel flow with permeable walls. *Journal of Fluid Mechanics*, 450:259–285, 2002.

[121] P. Orlandi, S. Leonardi, and R. A. Antonia. Turbulent channel flow with either transverse or longitudinal roughness elements on one wall. *Journal of Fluid Mechanics*, 561:279–305, 2006.

[122] T. P. Chiang, W. H. Sheu, and Robert R. Hwang. Effect of Reynolds number on the eddy structure in a lid-driven cavity. *International Journal for Numerical Methods in Fluids*, 26(5):557–579, 1998.

[123] P. N. Shankar. *Slow viscous flows: qualitative features and quantitative analysis using complex eigenfunction expansions*. Imperial College Press, 2007.

[124] A. Maali and B. Bhushan. Measurement of slip length on superhydrophobic surfaces. *Philosophical Transactions of the Royal Society A*, 370(1967):2304–2320, 2012.